Satellite-Assisted WOFOST Yield Prediction for Green Maize and Winter Barley in the Netherlands

Shijie Hu

Satellite-Assisted WOFOST Yield Prediction for Green Maize and Winter Barley in the Netherlands

by

Shijie Hu

to obtain the degree of Master of Science

at the Delft University of Technology,

to be defended publicly on 30 September, 2025.

Student number: 6024416
Project duration: February 1, 2025 – August 31, 2025
Thesis committee: Dr. ir. J. Timmermans, TU Delft, main supervisor
Dr. ir. P. M. van Bodegom, Leiden University
Dr. S. Pande, TU Delft

TU Delft

Preface

Looking back on this journey of study and research, I am grateful that I chose the path of remote sensing. When I first encountered the field, I knew almost nothing about what “remote sensing” truly was or what it could do. It lived mostly in textbooks and algorithms, interesting, but distant. That changed during an internship at an agricultural remote sensing company, when everything became concrete and vivid. The first time I used satellite imagery to monitor tomato growth, and could tell my family, “I’m using satellites to see how the crops are doing”. I felt a real connection between technology, the land, and everyday life.

That renewed connection to the land gradually led me into agricultural remote sensing and crop modeling. I am very happy that I chose this topic. At the beginning, the maze of model parameters, unfamiliar algorithms, and unexpected issues often left me puzzled and frustrated. Yet these challenges taught me how to read the literature more critically, to debug patiently, and to search for answers step by step. Completing this thesis has been more than a research task—it has been a personal journey of learning through uncertainty and growing through repeated attempts.

First and foremost, I would like to express my heartfelt gratitude to my supervisors, Joris, Peter, and Saket, for their invaluable guidance and steady support throughout this work. I am especially thankful to Joris, who consistently gave me positive energy and encouragement, both academically and in life. I am also deeply grateful to Dr. Allard de Wit for generously sharing the latest winter barley phenological parameters, which substantially advanced this research.

These two years of study in the Netherlands have brought profound growth. I have met many wonderful people, gained new perspectives, and also experienced the loss of someone important to me. Two years ago, I was the kind of girl who might feel upset if no one came to pick me up on a rainy day; now I can cycle in the rain and even find it amusing, the rhythm of raindrops on my coat somehow makes me feel free. Thank you, Dutch rain, for teaching me resilience in such an unexpected way. The rain that falls in a person’s life is not always visible to others; each of us goes through our own rainy seasons. And of course, there is sunlight too.

Shijie Hu
Delft, July 2025

Contents

Abstract

Accurate field-scale crop yield prediction is critical for supporting sustainable agricultural management under increasing climate variability. Process-based crop growth models, such as WOFOST, provide a physically consistent framework for simulating crop development and biomass accumulation, but their predictive performance is often limited by uncertainties in parameterization, inputs, and structural assumptions. To address these limitations, this study explores the integration of satellite-derived biophysical parameters into WOFOST using an Ensemble Kalman Filter (EnKF) for dynamic data assimilation, aiming to improve the accuracy of canopy development and yield estimation for green maize and winter barley in the Netherlands.

Three biophysical variables, i.e., Leaf Area Index (LAI), Canopy Chlorophyll Content (CCC), and Canopy Water Content (CWC), were retrieved from Sentinel-2 imagery and assimilated individually into WOFOST at the parcel scale for the 2022 growing season. Model performance was evaluated against independent CBS provincial-scale statistics. The results demonstrate that assimilating LAI significantly improved WOFOST's simulations of canopy dynamics and yield formation. For green maize, the mean yield bias was reduced from -3.78 t ha^{-1} (-27.6%) to -0.11 t ha^{-1} (-0.81%), and the RMSE decreased from 3.89 t ha^{-1} to 0.99 t ha^{-1}, indicating a substantial enhancement in predictive accuracy. In contrast, CCC and CWC provided limited additional benefit under the current implementation, largely because they were derived from fixed biochemical coefficients and thus contributed less independent information. Sensitivity experiments further revealed that the number, timing, and uncertainty of assimilated observations strongly affect assimilation performance, with the greatest improvements achieved during canopy expansion and peak-growth stages.

Overall, this study demonstrates the potential of integrating satellite-derived biophysical parameters into process-based crop models via EnKF to enhance field-scale yield predictions. Beyond the widely studied maize applications, our results confirm that the proposed system also performs well for winter barley, highlighting its broader applicability. While LAI assimilation proved most effective, our experiments with CCC and CWC illustrate both the opportunities and current limitations of incorporating additional physiological indicators. Future work should therefore focus on advancing the effective assimilation of CCC and CWC and on developing strategies for multi-variable assimilation, ultimately enabling more comprehensive and robust crop monitoring under diverse environmental conditions.

Keywords: WOFOST, Sentinel-2, Ensemble Kalman Filter, crop yield prediction, data assimilation

1

Introduction

1.1. Relevance

Ensuring global food security has become an urgent challenge under the dual pressure of climate change and population growth. According to the global risks report, global food shortage, together with global water scarcity, is ranked as the fourth-highest threat to human society over the next decade (World Economic Forum, 2025). Climate change, extreme weather events, and resource limitations increasingly undermine the stability of the agricultural system (Masson-Delmotte et al., 2018). Progress indicators suggest that the world remains on the wrong track in achieving Sustainable Development Goal 2.2, which aims to eliminate all forms of malnutrition by 2030 (FAO, IFAD, UNICEF, WFP and WHO, 2024). To meet the demands of a population exceeding 90 billion by 2050, global food production must increase by approximately 70% (Wirsenius et al., 2010).

Achieving this goal requires addressing several interacting challenges, including pest and disease management, agricultural water management, soil health management, and the adoption of sustainable precision farming practices (Lakhiar et al., 2024; Tilman et al., 2011; UNICEF et al., 2023). Effective pest and disease management minimizes avoidable yield losses by combining multi-scale surveillance (field scouting, spore or insect traps, and remote sensing) with economic-threshold decision rules, so actions are triggered by risk rather than by the calendar; host resistance, crop rotation, and habitat management lower baseline pressure, while targeted controls applied with precise timing and placement contain outbreaks and slow resistance evolution. Agricultural water management stabilizes production by aligning irrigation timing and amounts with crop phenology and evaporative demand, using scheduling based on crop evapotranspiration, soil-moisture sensing, and canopy or thermal indicators, and by delivering water through drip systems, pulsed application, or variable-rate irrigation; where appropriate, regulated deficit irrigation conserves water at non-critical stages, and coupling irrigation with fertigation improves nutrient delivery while managing salinity risks. Soil health management, implemented through diversified rotations, cover crops, reduced tillage, and organic amendments, builds soil organic matter and aggregation, enhances infiltration and available water capacity, strengthens microbially mediated nutrient cycling and disease suppression, and thereby improves yield stability across both wet and dry

years while reducing erosion and off-site losses.

Precision agriculture (PA) is a data-driven, technology-enabled farm management strategy that monitors, quantifies, and evaluates the needs of specific crops and fields (Gebbers and Adamchuk, 2010). Building on this foundation, PA integrates multi-source observations from satellites and unmanned aerial vehicles (UAVs), in-field and proximal sensors, and machinery telemetry with geospatial analytics, crop growth models, and (where appropriate) machine-learning methods to translate measurements into site-specific actions such as variable-rate irrigation, fertilization, seeding, and crop protection. A key capability is accurate, in-season crop-yield prediction, which is used to diagnose the combined effects of pest pressure, nutrient deficiencies, water stress, and soil constraints during the growing season and to trigger proactive interventions at the right time and place while quantifying decision uncertainty.

1.2. Current State of Art

Nowadays, process-based crop models offer a promising approach to simulating and forecasting crop yields under varying environmental and management conditions. They are capable of representing underlying physiological processes such as photosynthesis, respiration, and biomass allocation. These models respond dynamically to environmental inputs such as temperature, solar radiation, precipitation, and soil conditions. Widely used models such as WOFOST, APSIM, and DSSAT have been extensively applied across scales and regions (Jones et al., 2003; Keating et al., 2003; Van Diepen et al., 1989). For example, DSSAT has also been evaluated for simulating maize and soybean growth and yield under rainfed conditions in Maryland, USA, where model predictions showed good agreement with field observations across multiple growing seasons (Akumaga et al., 2023). Furthermore, Chisanga et al., 2021 evaluated both APSIM and DSSAT-CERES-Maize models in rainfed maize systems in Zambia, demonstrating their capacity to simulate local yield dynamics under varying seasonal conditions. In addition to these major crops, crop models have also been successfully applied to less common species, demonstrating their adaptability across diverse cropping systems. For instance, Shi et al., 2022 used the WOFOST model to simulate yield of Lycium barbarum L. (goji berry), a perennial fruit crop in northwestern China. After calibration, the model accurately predicted both summer and autumn harvests, with yield errors below 6%. The wide application highlights the robustness and flexibility of process-based models in capturing yield responses across diverse crops, climates, and management conditions, making them suitable tools for both idealized projections and real-world agronomic decision-making.

However, despite their strengths, the practical application of process-based crop models remains limited by three major challenges. First, mechanistic crop models require numerous input parameters, such as crop variety traits, soil properties, and management practices. However, many of these parameters are difficult to obtain or vary significantly across regions, leading to high uncertainty in model parameterization and reduced reliability of the simulation results (Pathak et al., 2012). Secondly, these models are highly sensitive to meteorological inputs such as solar radiation, temperature, and precipitation. However, these weather data often contain measurement errors, spatial interpolation uncertainties, or may be unavailable at the required temporal and spatial resolution. Such uncertainties in the driving inputs can propagate through the model, leading to significant deviations in simulated crop growth and yield outcomes. Thirdly, although mechanistic models aim to simulate the entire crop life-

cycle by incorporating key processes such as photosynthesis, canopy-atmosphere gas exchange, and soil water and temperature dynamics, many of these physiological and environmental processes are simplified for computational feasibility. Such simplifications may limit the model's ability to accurately capture crop responses under complex or stress-prone environmental conditions (Marin et al., 2017).

In contrast, satellite remote sensing provides an alternative approach towards precision agriculture. Since the 1970s, satellite remote sensing has been widely applied for non-destructive estimation of crop yields, offering spatially explicit, frequent, and non-destructive observations that are highly valuable for crop monitoring and modeling (Liang and Qin, 2008). Various types of remote sensing technologies have been employed. Thermal infrared remote sensing enables the estimation of land surface temperature and evapotranspiration, which are closely related to plant water stress (Zhou et al., 2021). Active microwave remote sensing, including Synthetic Aperture Radar (SAR), is capable of acquiring data regardless of cloud cover or lighting conditions and is particularly useful for assessing soil moisture, crop structure, and even biomass under certain conditions (Alebele et al., 2021). Optical remote sensing, which captures reflectance in visible and near-infrared wavelengths, is widely used for retrieving vegetation indices such as NDVI and EVI, which are proxies for canopy greenness and biomass (Panda et al., 2010). In particular, Sentinel-2 offers multi-spectral imagery with high spatial resolution (10-20 meters) and a revisit frequency of five days, making it suitable for near real-time agricultural applications (Franch et al., 2021). For example, Castro, 2024 used time-series Sentinel-2 imagery to calculate NDVI for cucumber, bean, and corn fields in Comayagua, Honduras, and developed multiple linear regression models to successfully predict both crop yield and disease occurrence with high accuracy. With the rapid development of deep learning techniques, more recent studies have leveraged advanced neural networks to improve yield estimation accuracy. For instance, Xiao et al., 2024 applied an attention-based convolutional neural network to Sentinel-2 time-series data for field-scale winter wheat yield prediction, achieving better performance than traditional machine learning models. These models have successfully used satellite imagery to estimate crop yields at the regional scale and are widely used due to their simplicity, ease of calculation, and high accuracy.

However, the relationships established through these models are only applicable to local regions and specific times, and rarely involve the growth mechanisms of crops. This is because most data-driven models are trained on local datasets and rely heavily on region-specific conditions such as soil properties, climate, and management practices. Since these models primarily capture statistical correlations rather than the underlying physiological processes, their performance tends to degrade when applied to different regions or time periods. Besides, optical Earth observation data are often affected by substantial temporal gaps, primarily due to cloud cover (Whitcraft et al., 2015). Moreover, the parameters retrieved from satellite data carry substantial uncertainty and often exhibit systematic bias arising from sensor calibration and atmospheric correction, view–illumination geometry/BRDF effects, mixed pixels and scale mismatch, cloud-shadow contamination, and the choice/parameterization of the inversion model (e.g., NDVI regressions vs. PROSAIL/ML). Because ground truth for calibration/validation is sparse and not fully representative, these errors can translate into location- and season-dependent biases that limit transferability. These limitations highlight the need to integrate remote sensing data with process-based crop models, which simulate crop growth and development based on environmental conditions and physiological mechanisms. By assimilating remote sensing observations into crop models, it becomes possible to constrain model uncertainties with real-time data, while benefiting from the model's ability to predict future crop states under changing conditions. A growing body of research has shown that incorporating remote sensing-derived variables into crop growth models enhances their

performance in simulating crop development and yield. For instance, Ji et al., 2021 coupled time□series Sentinel-2 imagery with a CASA-WOFOST model to simulate field-scale wheat yield in China, achieving an R^2 of 0.84, which significantly reduced runtime and offering robustness under complex terrain conditions compared to WOFOST alone. Additionally, Bouras et al., 2023 assimilated Sentinel-2-derived LAI into a semi-empirical crop growth model (SAFY) using an Ensemble Kalman Filter (EnKF) to estimate winter wheat yield at $20\ m$ resolution, achieving a 70% increase in capturing spatial variability and a 53% reduction in RMSE compared to model-only simulations. These studies demonstrate the potential of integrating remote sensing data into crop models to enhance yield estimation accuracy, spatial representativeness, and computational efficiency, particularly when adapted to diverse field conditions.

While many existing data assimilation studies rely predominantly on single-source remote sensing variables such as LAI or vegetation indices, these indicators reflect only limited aspects of crop growth and often fail to capture critical physiological responses such as chlorophyll dynamics and water status. Moreover, most of these studies focus on commonly modelled crops like wheat, maize, or rice, with limited attention to other cereals. In particular, the application of the WOFOST crop model to winter barley remains underexplored in the literature, and no known studies have integrated multi-source biophysical variables into WOFOST for this crop.

1.3. Research Objectives

Building on the FPCUP framework “Consistent retrieval of crop yields using a data assimilation platform,” which simulated yields with the WOFOST model across the Netherlands, this study proposes a multi-variable assimilation framework that integrates LAI, Canopy Chlorophyll Content (CCC), and Canopy Water Content (CWC) retrieved from Sentinel-2 imagery into the WOFOST model using the EnKF. Simulations are conducted at the parcel scale for both green maize and winter barley in the Netherlands during the 2022 growing season. In addition, the study evaluates the impact of different observation uncertainty quantification strategies on assimilation performance. By extending the WOFOST model to a less-studied crop and enhancing its predictive capability through multi-source assimilation, this research provides a more physiologically comprehensive and scalable approach for regional crop monitoring and yield forecasting.

The aim of this study is to enhance the physiological completeness and predictive capability of WOFOST for crop monitoring and yield forecasting. Specifically, we seek to: (i) improve crop-state estimation by assimilating multiple biophysical variables through a data assimilation approach, (ii) assess the model’s performance under different assimilation scenarios, and (iii) demonstrate the applicability of the approach to multiple crop types at the parcel scale.

The remainder of this thesis is structured as follows. Chapter 2 introduces the key concepts relevant to this study, including the WOFOST crop model, remote sensing techniques, data assimilation methods, research questions, and study area. Chapter 3 presents the materials and methods, detailing the model configuration, data sources, assimilation framework, and uncertainty analysis. Chapter 4 reports the experimental results and sensitivity analyses. Chapter 5 discusses the key findings, limitations, and implications of the study. Finally, Chapter 6 concludes the thesis with broader implications and suggestions for future research and applications.

2

Literature Review

This chapter introduces the key concepts and models underpinning this study. Section 2.1 provides an overview of the WOFOST crop growth model, outlining its structure, principles, and capabilities. Section 2.2 presents the role of satellite remote sensing in agricultural monitoring, with a focus on the biophysical variables retrievable from Sentinel-2 imagery. Section 2.3 discusses data assimilation techniques, particularly the EnKF, and reviews relevant studies in crop yield estimation. Section 2.4 outlines the research questions guiding this work, and Section 2.5 describes the study area and selected crops, including green maize and winter barley, within the context of parcel-level modeling in the Netherlands.

2.1. Crop Growth Models

A wide range of crop growth models has been developed to simulate canopy development, biomass production, and yield formation under varying environmental and management conditions. Among the most commonly used are DSSAT, APSIM, CropSyst, AquaCrop, and WOFOST, which differ in their modeling approaches, input requirements, and suitability for integration with remote sensing and data assimilation frameworks (Di Paola et al., 2016). DSSAT employs a suite of crop-specific modules and combines mechanistic and empirical components to simulate crop phenology, biomass, and soil–water–nutrient dynamics, but often requires extensive cultivar-specific calibration to achieve accurate predictions. APSIM offers a highly modular and flexible structure that allows detailed representation of crop, soil, and management interactions, making it suitable for climate adaptation studies but increasing model complexity and data demands. CropSyst emphasizes multi-season and multi-crop simulations with a focus on water, carbon, and nitrogen balances, while AquaCrop simplifies model structure and parameterization, specializing in yield response to water availability and water-use efficiency, making it particularly useful in water-limited environments.

In contrast, WOFOST adopts a fully mechanistic and physiologically explicit approach, simulating daily photosynthesis, respiration, assimilate partitioning, and phenological development. Compared with

DSSAT and APSIM, WOFOST requires fewer cultivar-specific parameters while maintaining a transparent model structure, which makes it easier to calibrate for less-studied crops and to couple with satellite-derived observations (Camargo and Kemanian, 2016). Moreover, WOFOST has been extensively validated and operationally implemented in large-scale systems such as the European Commission's MARS Crop Yield Forecasting System and the Global Yield Gap Atlas, demonstrating its robustness and scalability (Boogaard et al., 2013). Recent studies have also demonstrated that WOFOST outperforms DSSAT-based models in simulating crop phenology and biomass accumulation, while showing greater stability across different sowing dates and agroclimatic conditions, making it more suitable for regional-scale crop monitoring and integration with satellite-derived observations (Singh et al., 2025). Therefore, these characteristics make WOFOST an appropriate modeling platform for this study.

2.1.1. The WOFOST Model

WOFOST (World Food Studies) is a process-based, dynamic crop growth simulation model developed to represent the physiological mechanisms of crop development under both potential and water-limited conditions (Boogaard et al., 1998; Supit and van Diepen, 1994). Unlike empirical models that rely on statistical correlations, WOFOST simulates crop growth by explicitly modeling key physiological processes, including radiation interception, photosynthesis, phenological development, dry matter accumulation, transpiration, and biomass partitioning. The model operates on a daily time step and supports detailed simulation from sowing to harvest.

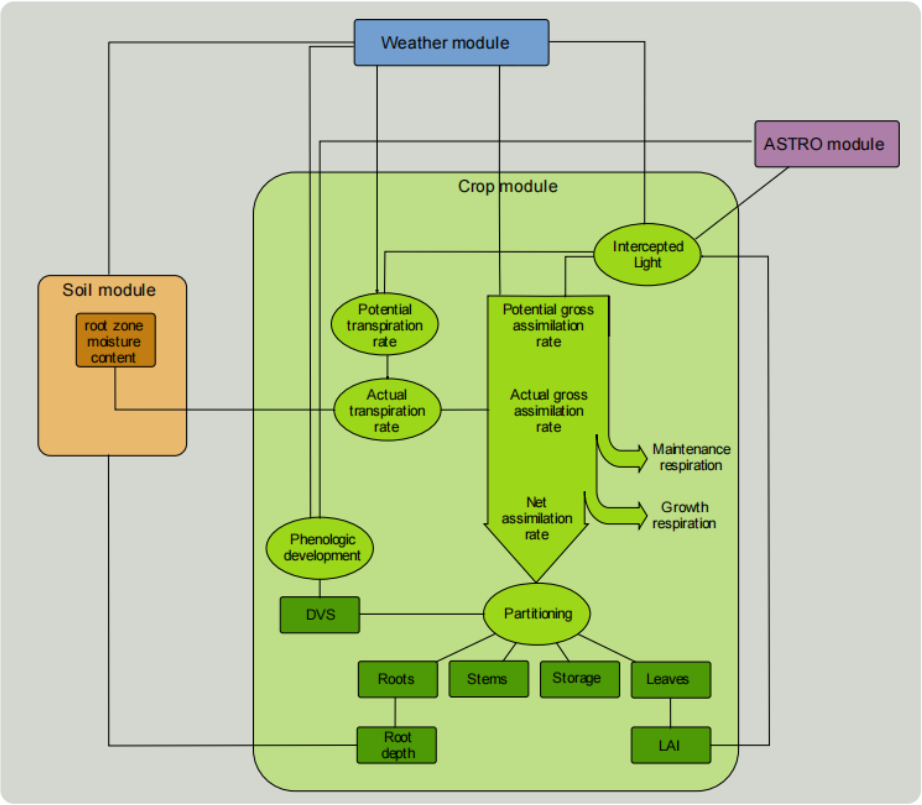

Figure 2.1: Simplified structure of the dynamic explanatory crop growth model WOFOST A. De Wit et al., 2019.

As illustrated in Figure 2.1, the model consists of several interlinked modules that describe interactions

between the crop, soil, atmosphere, and management inputs. The crop module represents the core physiological processes, starting from the interception of solar radiation, which drives biomass production through gross assimilation. The ASTRO module provides daily solar radiation and day length data, which, combined with weather variables from the weather module, determine potential assimilation and transpiration rates. The soil module governs water availability in the root zone, affecting actual transpiration and thus influencing growth under water-limited conditions. Phenological development is modeled based on accumulated thermal time and is expressed using a Development Stage Index (DVS). The assimilated biomass is partitioned among plant organs, including roots, stems, leaves, and storage organs, according to phenological stage, and the resulting LAI dynamically feeds back into light interception.

This modular structure allows WOFOST to simulate crop growth responses to varying environmental conditions and management practices with physiological realism. It provides the foundation for integrating remote sensing data and data assimilation techniques in subsequent chapters.

2.1.2. Simulation Structure and Key Processes

WOFOST simulates crop growth by integrating a series of biophysical processes, including light interception, photosynthesis, phenological development, biomass accumulation and partitioning, and soil water dynamics. These components are organized into interdependent modules, as illustrated in Figure 2.1. Below, the key simulation processes are introduced.

1) Light Interception and Photosynthesis. WOFOST estimates daily dry matter production based on intercepted photosynthetically active radiation (PAR) and crop-specific light use efficiency (LUE). The intercepted PAR is calculated using the Beer-Lambert law:

$$\mathrm{PAR}_{\mathrm{int}} = \mathrm{PAR}_{\mathrm{inc}} \cdot (1 - e^{-k \cdot LAI}) \tag{2.1}$$

where $\mathrm{PAR}_{\mathrm{inc}}$ is the incident PAR, k is the light extinction coefficient, and LAI is the leaf area index Supit and van Diepen, 1994.

The gross assimilation rate (A_g) is then calculated by:

$$A_g = \varepsilon \cdot \mathrm{PAR}_{\mathrm{int}} \tag{2.2}$$

where ε is the light use efficiency (g MJ^{-1}) Boogaard et al., 1998.

2) Respiration and Net Assimilation. Maintenance and growth respiration are subtracted from gross assimilation to derive the net daily biomass increment:

$$A_n = A_g - R_m - R_g \tag{2.3}$$

where R_m and R_g represent maintenance and growth respiration, respectively Boogaard et al., 1998.

3) Phenological Development. Crop development is simulated as a function of temperature using a Development Stage (DVS) index ranging from 0 (sowing) to 2 (maturity). DVS increases with daily accumulated temperature above a crop-specific base temperature:

$$\Delta\text{DVS} = \frac{T_{avg} - T_{base}}{T_{sum}} \tag{2.4}$$

where T_{avg} is daily average temperature, T_{base} is the base temperature for development, and T_{sum} is the required thermal time for the current stage Supit and van Diepen, 1994.

4) Biomass Partitioning. The assimilated biomass is partitioned into four organs—leaves, stems, storage organs (e.g., grains), and roots—based on DVS-specific partitioning coefficients. The resulting dynamics of LAI and root depth feed back into radiation interception and soil water extraction, respectively Boogaard et al., 1998.

5) Water-Limited Production. In water-limited mode, crop transpiration and photosynthesis are constrained by soil water availability. Potential transpiration is computed based on atmospheric demand, while actual transpiration depends on the soil water content in the root zone:

$$T_a = T_p \cdot f_w \tag{2.5}$$

where T_p is the potential transpiration, and f_w is a reduction factor (0–1) based on soil moisture stress Boogaard et al., 1998. Water stress also affects leaf expansion, photosynthesis, and biomass partitioning.

2.1.3. Model Inputs and Outputs

1) Meteorological Inputs. WOFOST requires the following daily atmospheric variables to simulate crop growth processes (Wageningen Environmental Research, 2024a), :

Table 2.1: Daily atmospheric variables required by WOFOST (Wageningen Environmental Research, 2024a)

Variable	Unit	Description
TMAX	°C	Daily maximum temperature
TMIN	°C	Daily minimum temperature
VAP	hPa	Mean daily vapor pressure
WIND	m s^{-1}	Mean daily wind speed at 2 meters above ground level
RAIN	cm day^{-1}	Daily precipitation, including rainfall and snow water equivalent
IRRAD	J m^{-2} day^{-1}	Daily global radiation
SNOWDEPTH	cm	Depth of snow cover (optional)

These meteorological drivers regulate key physiological processes such as photosynthesis, evapotranspiration, and phenological development, thereby strongly influencing crop growth and yield forma-

tion. Solar radiation (IRRAD) provides the primary energy source for photosynthesis and dry matter accumulation, while temperature (TMAX, TMIN) controls enzyme activity and regulates phenological development, including germination, leaf expansion, flowering, and grain filling. Vapor pressure (VAP) and wind speed (WIND) jointly determine atmospheric demand for water, which strongly affects transpiration and canopy cooling. Precipitation (RAIN) and snow cover (SNOWDEPTH) directly govern soil moisture availability, influencing root water uptake and the onset of water stress. Inaccurate representation of these drivers can propagate errors through the water, carbon, and energy balance calculations, leading to unrealistic estimates of biomass accumulation, crop water use, and final yield. Therefore, accurate and high-resolution weather data are critical to ensure reliable crop growth simulations in WOFOST.

2) Soil Inputs. To simulate the soil water balance, WOFOST requires a set of parameters that characterize the soil profile. Key variables include the soil moisture retention properties, such as field capacity and wilting point, which determine the amount of water available for crop uptake under different soil moisture conditions. Soil texture and hydraulic conductivity are also essential, as they govern infiltration rates, drainage, and the overall dynamics of water movement through the soil. In addition, the specification of initial soil moisture content provides the starting condition for the simulation and strongly affects early crop development and subsequent stress responses. Finally, maximum rooting depth and total soil depth define the volume of soil that can potentially be explored by the root system, thereby constraining both water availability and nutrient uptake. Together, these parameters regulate root growth, plant water status, and the onset of water stress, and are thus critical for reliable crop growth and yield simulations.

3) Crop Parameters. Each crop type in WOFOST is defined by a set of physiological and morphological parameters that describe its growth and development processes. Among these, thermal time requirements specify the heat accumulation needed to progress through different phenological stages, thereby determining the crop's growth duration and maturity. Leaf characteristics, such as specific leaf area and leaf lifespan, control canopy expansion and turnover, influencing the interception of radiation and photosynthetic efficiency. Assimilate partitioning factors govern how carbohydrates are distributed among leaves, stems, roots, and storage organs, directly affecting biomass allocation and yield formation. In addition, parameters related to light-use efficiency and the maximum attainable leaf area index define the potential photosynthetic capacity and canopy development under optimal conditions. Finally, maximum rooting depth and critical stress thresholds describe the crop's ability to access soil resources and tolerate water or nutrient stress. These parameters are typically derived from field experiments, literature sources, or calibration procedures. In this study, parameterization for maize and winter barley follows the standard WOFOST crop files, with selected values further adjusted to reflect regional agronomic knowledge. The detailed parameter values used in the simulations are provided in the following chapter.

4) Model Outputs. WOFOST provides daily outputs that reflect crop status and environmental interactions. Table 2.2 explains the output from the WOFOST model. This set of results is typical for the PCSE/WOFOST implementation (Wageningen Environmental Research, 2024b).

Table 2.2: Summary of key simulation outputs and phenological indicators from PCSE/WOFOST 7.2.

Variable	Description
DVS	The development stage of the crop, ranging from 0 (sowing/emergence) to 2 (maturity).
LAIMAX	The maximum Leaf Area Index (LAI) reached during the crop's growth cycle.
TAGP	Total Above-Ground Production: the accumulated dry biomass (kg/ha) of all above-ground plant organs.
TWSO	Total dry weight of storage organs (e.g., grains, tubers) at the end of the simulation.
TWLV	Total dry weight of leaves at the end of the growth cycle.
TWST	Total dry weight of stems.
TWRT	Total dry weight of roots (below-ground biomass).
CTRAT	Cumulative crop transpiration throughout the growth cycle (cm).
RD	Final rooting depth (cm), indicating the depth reached by crop roots during the simulation.
CEVST	Cumulative soil evaporation during the growth cycle (cm).
DOS	Date of sowing. May be defined as "None" if simulation starts from emergence.
DOE	Day of emergence (DVS = 0).
DOA	Day of anthesis (flowering; DVS = 1).
DOM	Day of maturity (DVS = 2).
DOH	Day of harvest. May be omitted if harvest coincides with maturity.
DOV	Day of vernalization completion. Only applicable to crops requiring cold exposure to induce flowering.

2.1.4. Applications and Limitations

WOFOST has been widely applied in a variety of agricultural studies due to its ability to mechanistically simulate crop growth and yield under different environmental and management conditions. It has served as a key component in national-scale crop forecasting systems such as the MARS Crop Yield Forecasting System in Europe, and has been adopted in both academic and operational settings for simulating crop performance, evaluating climate impacts, and supporting decision-making in precision agriculture (A. De Wit et al., 2019). Numerous studies have demonstrated the model's utility in estimating potential yield, monitoring water stress, and analyzing the effects of management scenarios across diverse regions and crop types. For example, Tao et al., 2020 modified the WOFOST model by introducing tree age as a dynamic parameter to simulate the growth and yield of perennial jujube trees, enabling accurate yield estimation across different orchard ages ($R^2 \geq 0.856$, RMSE $\leq$ 0.68 t/ha). Xu et al., 2024 further extended the model's capacity to simulate nutrient-limited systems by incorporating a nitrogen dynamics module, successfully capturing the responses of Korla Fragrant pear trees to varying fertilization regimes, with strong performance across LAI, soil nitrogen, and yield simulations. In addition, Li et al., 2024 demonstrated the model's suitability for future climate impact assessments by coupling WOFOST with CMIP6 projections, predicting spatially varying spring wheat yield responses

under different emission scenarios, with increases up to 20.2% in the short term. These studies illustrate the versatility of WOFOST in simulating both annual and perennial crops, under varying environmental conditions, nutrient regimes, and future climate scenarios.

However, while previous research has explored different model enhancement, there remains a lack of studies focusing on the joint assimilation of multiple biophysical variables (e.g., LAI, CCC, and CWC) into the WOFOST model. Additionally, its application to certain crops such as winter barley, especially at the parcel level under real field conditions in Northwest Europe, has been limited. To address these gaps, this study aims to enhance yield estimation accuracy by integrating multi-source remote sensing variables into the WOFOST framework, focusing on maize and winter barley in Drenthe, the Netherlands. The following section details the methodology developed to achieve this goal.

2.2. Remote Sensing

Remote sensing plays a critical role in monitoring crop growth and forecasting yields, providing spatially continuous and temporally frequent data over large areas. A variety of techniques have been developed to extract biophysical parameters, such as LAI, CCC, and vegetation indices (e.g., NDVI, VHI), which serve as proxies for crop health and productivity. These variables are often assimilated into crop growth models or directly used in machine learning frameworks for yield estimation. Among the most widely used approaches are optical, thermal, and Synthetic Aperture Radar (SAR) observations, which differ in their sensing principles and the type of biophysical information they capture. Optical remote sensing relies on measuring surface reflectance in the visible, near-infrared, and shortwave-infrared regions of the electromagnetic spectrum, enabling the retrieval of key vegetation traits such as leaf chlorophyll content, leaf water content and biomass. Through vegetation indices and radiative transfer modeling, optical techniques provide direct insights into plant photosynthetic activity, pigment dynamics, and stress responses (Tagliabue et al., 2022). Thermal infrared (TIR) remote sensing complements optical data by providing information on canopy temperature, which can be used to estimate evapotranspiration, detect heat stress, and quantify water-use efficiency (Anderegg et al., 2024). While thermal measurements are powerful for understanding crop water relations, their application is often constrained by coarse spatial resolution, lower revisit frequency, and high sensitivity to atmospheric conditions, especially when using satellite-based observations. SAR techniques, in contrast, are active microwave systems that operate independently of sunlight and penetrate clouds, making them valuable in regions with frequent cloud cover or low-light conditions. SAR backscatter is sensitive to canopy structure, biomass, and surface moisture, enabling monitoring of crop height and phenological development even under cloudy conditions (Wang et al., 2023). However, SAR signals are indirect and require complex calibration and inversion models to retrieve biophysical parameters accurately, which complicates operational implementation compared with optical approaches. Therefore, in this thesis, I focus on optical measures derived from Sentinel-2 imagery, as they provide high spatial resolution and are well-suited for parcel-scale crop monitoring

2.2.1. Optical remote sensing in Crop Monitoring

Despite the complementary capabilities mentioned above, optical remote sensing remains the preferred approach for most agricultural monitoring applications. This preference is driven by several advantages: (1) High physiological sensitivity: optical reflectance directly captures vegetation pigment

dynamics, canopy structure, and photosynthetic activity; (2) Rich spectral diversity: multispectral and hyperspectral sensors provide multiple vegetation indices, enabling accurate retrieval of LAI, CCC, and CWC; (3) High spatial and temporal resolution: missions such as Sentinel-2 (10–20 m, 5-day revisit) and Landsat allow fine-scale monitoring of crop development across growing seasons; (4) Operational maturity and accessibility: optical data are widely available, computationally efficient to process, and supported by standardized workflows for vegetation trait retrieval (Omia et al., 2023). Therefore, in this study, we exploit Sentinel-2 multispectral imagery to derive biophysical variables through physically based inversion and vegetation index approaches. Specifically, we focus on leaf area index (LAI), canopy chlorophyll content (CCC), and canopy water content (CWC) because they jointly capture canopy structure, photosynthetic capacity, and water status—three pillars that govern growth and yield formation. Figure 2.2 illustrates the spectral basis for these variables and guides our Sentinel-2 band selection and retrieval strategy.

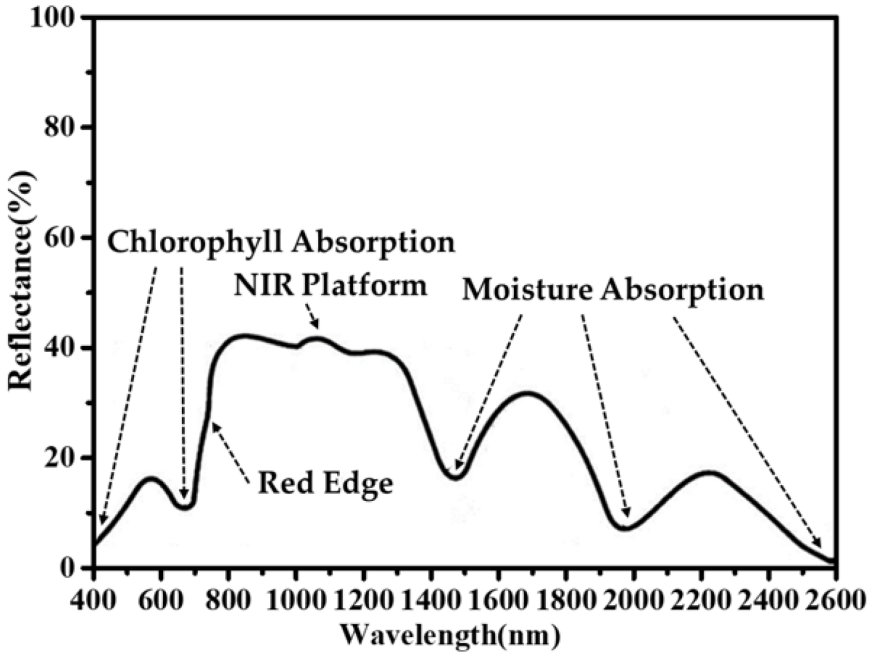

Figure 2.2: Typical spectral reflectance curve of green vegetation, highlighting chlorophyll absorption ($430 - 480\ nm$ and $660\ nm$), red-edge sensitivity ($700–740\ nm$), NIR plateau ($800–1000\ nm$), and strong water absorption features ($970, 1200, 1450, 1940\ nm$). These spectral regions correspond to Sentinel-2 bands used for estimating LAI, CCC, and CWC. Ai et al., 2020.

LAI quantifies the one-sided green leaf area per unit ground area and is a fundamental control on light interception, transpiration, and biomass accumulation. Its optical estimation typically exploits the contrast between visible and near-infrared reflectance and the high sensitivity of the red-edge region ($700–740\ nm$) to canopy density, using Sentinel-2 bands B4, B5–B7, B8, and B8A. Recent reviews highlight that hybrid retrieval methods, which integrate vegetation indices with physically based radiative transfer model (RTM) inversion, outperform single-index approaches in both accuracy and temporal stability (Croci et al., 2022).

CCC represents the total canopy chlorophyll per unit ground area and serves as a direct proxy for photosynthetic capacity and nitrogen status. Chlorophyll strongly absorbs radiation in the blue ($430–480\ nm$) and red ($660\ nm$) regions, while the steep slope of the red-edge provides additional sensitivity to chloro-

phyll variation. Sentinel-2 bands B2, B4, and B5–B7 are widely used for CCC retrieval through indices such as the Chlorophyll Index (CIred-edge) and RTM-based inversion. Recent studies confirm that CCC retrievals derived from Sentinel-2 red-edge bands are robust across different crops and phenological stages, offering valuable constraints for crop productivity assessments (Delloye et al., 2018).

CWC measures the water stored in foliage per unit ground area and is closely linked to crop water stress, stomatal regulation, and yield stability. CWC estimation relies on strong water absorption features in the short-wave infrared (SWIR) region, particularly near 970, 1200, 1450, and $1940\ nm$, which correspond to Sentinel-2 bands B11 and B12. Water-sensitive indices such as the Normalized Difference Water Index (NDWI) and the Moisture Stress Index (MSI), combined with RTM-based equivalent water thickness (EWT) inversion, have proven effective for quantifying canopy water dynamics (Konings et al., 2021).

Together, LAI, CCC, and CWC provide complementary and minimally redundant information: LAI constrains canopy structural development, CCC reflects photosynthetic potential, and CWC captures crop water status. The spectral features highlighted in Figure X therefore justify our optical strategy for retrieving these variables from Sentinel-2 imagery, which are subsequently assimilated into the WOFOST crop growth model to improve state estimation and field-scale yield forecasting.

2.2.2. Available Tools and Processing Platforms

To facilitate the estimation of such parameters, dedicated software tools and processing chains have been developed. One widely used platform is the Sentinel Application Platform (SNAP), developed by the European Space Agency. SNAP provides a modular environment for processing and analyzing data from Sentinel-1, Sentinel-2, and Sentinel-3 missions. Through SNAP's biophysical processor, users can retrieve key vegetation parameters such as LAI, Fraction of Absorbed Photosynthetically Active Radiation (FAPAR), and CCC from Sentinel-2 reflectance data using semi-empirical inversion techniques. These derived products are particularly valuable for crop growth monitoring and assimilation into models such as WOFOST or DSSAT. Beyond SNAP, other platforms and methods have been developed. The Google Earth Engine (GEE) environment allows for scalable, cloud-based processing of large volumes of satellite data and includes tools for vegetation index computation, crop classification, and time series analysis. For instance, machine learning models trained on GEE have been used to estimate crop phenology and yield by learning temporal patterns in spectral reflectance curves. Additionally, radiative transfer model (RTM) inversion methods, such as those based on PROSAIL, have been applied to retrieve chlorophyll and structural parameters at fine spatial resolution, albeit with higher computational cost and complexity. While these tools significantly lower the barrier for crop-related remote sensing applications, challenges remain. Many parameter retrieval algorithms are sensitive to atmospheric correction quality and sensor calibration, and often require site-specific tuning. Furthermore, coarse temporal or spatial resolution may limit their effectiveness for smallholder fields or intra-seasonal stress detection. Continued integration of multi-source data—optical, thermal, and SAR—and advances in fusion techniques and uncertainty quantification will be essential for improving the robustness and generalizability of crop parameter estimation.

2.2.3. Integrating Models with Satellite Remote Sensing

Several recent studies demonstrate contrasting methodological approaches. For instance, applied the WOFOST crop growth model in combination with remotely-sensed LAI and used the SUBPLEX optimization algorithm to minimize simulation errors by adjusting sensitive parameters. This physically-based data assimilation approach maintains mechanistic interpretability but requires careful calibration and often underperforms in highly heterogeneous fields due to parameter uncertainty and model rigidity. In contrast, Sagan et al., 2021 explored purely data-driven methods by training convolutional neural networks (CNNs) on multi-temporal high-resolution imagery from WorldView-3 and PlanetScope. Their method avoids mechanistic modeling and instead learns spatiotemporal patterns directly from image sequences. While achieving high accuracy at the field scale ($R^2 > 0.8$), this approach is highly dependent on the availability of labeled yield data and lacks transparency, limiting its transferability across regions and years. Another hybrid approach was proposed by Wu et al., 2021, who combined Sentinel-2 NDVI time series with high-resolution cropland masks to enhance regional winter wheat yield estimation using regression models. This approach effectively leverages spatial detail but still relies on hand-crafted features (like peak NDVI), which may not generalize well under abnormal climate or management conditions.

Despite their contributions, all three approaches face limitations. Physically-based models often struggle with parameter estimation under limited ground truth; deep learning models are prone to overfitting and lack physical consistency; statistical approaches may fail under extreme conditions due to their empirical nature. Moreover, most studies remain region-specific, and few have addressed uncertainty quantification comprehensively. Therefore, integrating physical understanding with data-driven flexibility is best operationalized via data assimilation, which combines satellite observations with process-based models to update crop states/parameters and to explicitly propagate observation and model errors. Doing so improves transferability beyond region-specific calibrations and yields reliable estimates for decision making.

2.3. Data Assimilation

2.3.1. Overview of Data Assimilation in Crop Modeling

Data assimilation (DA) is a powerful framework that integrates remote sensing (RS) observations with crop growth models to improve simulation accuracy and real-time forecasting. It aims to bridge the gap between observation-based monitoring and process-based simulation, leveraging the strengths of both. In the context of crop modeling, DA techniques are typically classified into three main categories: parameter assimilation, state variable assimilation, and forcing data assimilation (Jin et al., 2018).

1) Parameter Assimilation. This approach involves adjusting model parameters (e.g., maximum leaf area index, light-use efficiency, partitioning coefficients) to minimize the discrepancy between simulated and RS-derived observations. Optimization algorithms such as the Shuffled Complex Evolution (SCE-UA), Genetic Algorithms (GA), or Bayesian inference (e.g., MCMC) are commonly employed. Parameter assimilation is often used for retrospective calibration or regionalization, enhancing model adaptability to specific crops or management practices.

2) State Variable Assimilation. State variable assimilation updates dynamic variables—such as LAI, biomass, or canopy water content—during the simulation process, based on real-time observations. Sequential filtering techniques, especially the Ensemble Kalman Filter (EnKF), have become popular due to their ability to handle non-linear processes and estimate uncertainty. Particle Filters (PF) and 4D-Variational (4D-Var) methods have also been applied, depending on the model complexity and data availability. This class of methods is particularly suitable for in-season crop monitoring and forecasting.

3) Forcing Data Assimilation. Rather than modifying model states or parameters, this method incorporates RS-derived datasets as direct replacements or corrections for external forcing inputs (e.g., solar radiation, precipitation, soil moisture). For instance, assimilating microwave-derived soil moisture or radiation fluxes can improve water balance estimation in crop models. This approach is effective when meteorological data is sparse or of low quality.

4) Data-Driven and Hybrid Approaches. In recent years, data-driven models—particularly those based on deep learning—have emerged as alternatives or complements to traditional process-based assimilation frameworks. Deep learning methods, such as Convolutional Neural Networks (CNNs) and Recurrent Neural Networks (RNNs), have been used to learn mappings between multi-temporal remote sensing data and crop yield or biophysical indicators. Some hybrid approaches incorporate deep learning into assimilation pipelines, either by estimating model parameters or states, or by serving as surrogates for specific processes. While these methods offer high flexibility and accuracy in specific scenarios, they often lack mechanistic interpretability and require large labeled datasets, limiting their generalizability across time and space.

Each of these DA pathways has distinct advantages and limitations. Parameter assimilation offers interpretability but is sensitive to overfitting; state variable assimilation captures real-time dynamics but requires careful treatment of observation errors; and forcing assimilation is flexible but relies heavily on the accuracy of external RS products. A detailed comparison is provided in Table 2.3. In this study, we adopt a state variable assimilation strategy based on the Ensemble Kalman Filter, which integrates multi-source Sentinel-2 derived variables into the WOFOST model to improve crop yield estimation.

Table 2.3: Comparison of data assimilation approaches in crop modeling

Method	**Description**	**Advantages**	**Limitations**
Parameter Assimilation	Adjusts model parameters (e.g., LUE, LAI_{max}) using optimization algorithms or Bayesian methods	Improves model adaptability to different crops/sites; retains physical meaning	Computationally intensive; risk of overfitting; limited for real-time use
State Variable Assimilation	Updates dynamic variables (e.g., LAI, biomass) based on observations during simulation using filters (e.g., EnKF, PF, 4D-Var)	Real-time correction; handles temporal variability well; supports uncertainty quantification	Requires frequent observations; sensitive to observation errors and filter settings
Forcing Data Assimilation	Replaces or corrects driving inputs (e.g., weather, soil moisture) using RS products	Improves input quality; low computational cost; easy to implement	Dependent on the availability and accuracy of external RS products

2.3.2. Ensemble Kalman Filter

The Ensemble Kalman Filter (EnKF) is a widely used sequential data assimilation method for combining model simulations with observations in a statistically consistent way. Unlike the classical Kalman filter, which is limited to linear systems, the EnKF approximates forecast error statistics using a Monte Carlo approach, making it suitable for nonlinear environmental models such as crop growth simulations. The filter operates by propagating an ensemble of model realizations, each representing a plausible state of the system given input uncertainties. When new observations become available, the ensemble is updated using the Kalman gain, which weighs the relative uncertainty in the model forecasts and the observations (A. d. De Wit and Van Diepen, 2007).

The analysis step updates each ensemble member as follows:

$$\mathbf{x}_a^{(i)} = \mathbf{x}_f^{(i)} + \mathbf{K}\left(\mathbf{y}^{(i)} - \mathbf{H}\mathbf{x}_f^{(i)}\right), \quad i = 1, \ldots, N \tag{2.6}$$

where $\mathbf{x}_f^{(i)}$ and $\mathbf{x}_a^{(i)}$ are the forecast and analysis states for ensemble member i, $\mathbf{y}^{(i)}$ is the perturbed observation, $\mathbf{H}$ is the observation operator, and N is the ensemble size. The Kalman gain $\mathbf{K}$ is computed as:

$$\mathbf{K} = \mathbf{P}_f\mathbf{H}^T\left(\mathbf{H}\mathbf{P}_f\mathbf{H}^T + \mathbf{R}\right)^{-1} \tag{2.7}$$

Here, $\mathbf{P}_f$ denotes the forecast error covariance matrix estimated from the ensemble, and $\mathbf{R}$ is the observation error covariance.

By assimilating observations into the model, the EnKF corrects biases and reduces uncertainty in state predictions, while preserving the dynamic consistency of the underlying simulation model. In this study, the EnKF was implemented to integrate satellite-derived observations into a process-based crop model, as detailed in the following sections.

2.4. Research Questions

While satellite remote sensing has become an essential tool for crop monitoring, and process-based models such as WOFOST offer detailed mechanistic representations of crop growth, there remains a clear gap in the integrated use of both approaches. Many previous studies have relied on vegetation indices or LAI time series alone for yield estimation, often neglecting underlying physiological processes. Conversely, purely mechanistic models require accurate, site-specific inputs that are difficult to obtain at scale. Moreover, most data assimilation frameworks applied in agricultural contexts focus on assimilating a single variable (typically LAI), with limited consideration of uncertainty propagation and multi-variable fusion. These limitations hinder the robustness and transferability of current yield forecasting systems, particularly under variable environmental and management conditions.

This study addresses these gaps by exploring how remote sensing–derived vegetation parameters can be effectively integrated into a process-based crop model using a data assimilation framework. The objective is to improve parcel-level yield prediction while accounting for uncertainty and leveraging multi-source observations. To guide this investigation, the following research questions are proposed:

- **Main Research Question:**
  - How can vegetation parameters derived from remote sensing be effectively integrated into crop growth models to improve yield prediction accuracy at the field scale?
- **Sub-questions:**
  - To what extent do satellite-driven yield predictions agree with ground-based reference data?
  - Which biophysical variables (e.g., LAI, CCC, CWC) most significantly influence yield simulation outcomes?
  - How can high-resolution Sentinel-2 observations be dynamically assimilated into models such as WOFOST using methods like the Ensemble Kalman Filter?
  - What are the dominant sources of uncertainty in the prediction system—stemming from model structure, parameterization, or observational data—and how can these uncertainties be characterized and minimized?

2.5. Study Area and Crop Description

The area of interest is Drenthe, a province located in the north-east part of the Netherlands ($52.9°\mathrm{N},\ 6.6°\mathrm{E}$). Drenthe is characterized by (1) relatively flat terrain and intensive crop cultivation, with most of the province consisting of farmland, which makes it well suited for remote sensing–based agricultural monitoring (Figure 2.3), (2) a temperate maritime climate, with moderate temperatures and relatively even precipitation throughout the year. Average daily temperatures range from around $5\,°\mathrm{C}$ in January to $18\,°\mathrm{C}$ in July, while annual precipitation typically ranges between 800 and 900 millimetres, providing favourable conditions for crop growth (Time and Date, 2022).

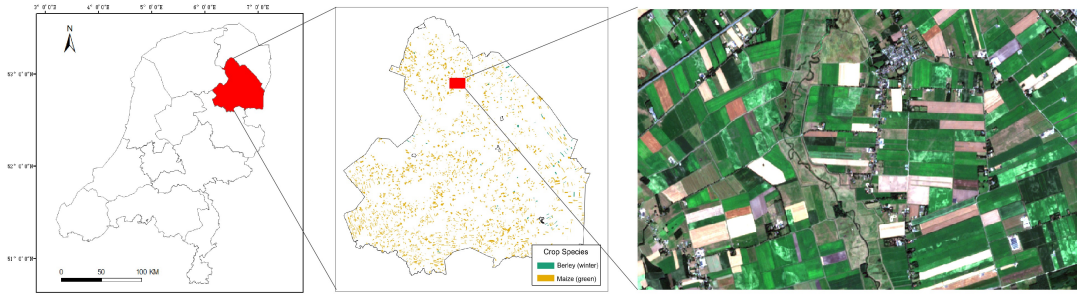

Figure 2.3: Location of the study area in the northeastern Netherlands. The left panel shows the national and provincial context, highlighting the selected agricultural region in red. The middle panel indicates the distribution of maize (green) and winter barley fields. The right panel displays a Sentinel-2 true-colour image acquired on August 13, 2022.

This study focuses on two crop types present in the BRP (Basisregistratie Gewaspercelen) parcel register: maize (green) and barley (winter). Table 2.4 summarizes the number of BRP parcels assigned to each type of crop in the Drenthe province.

Table 2.4: Number of crop parcels by type in Drenthe (BRP register)

Crop Type	Number of Parcels
Maize (green)	4,692
Barley (winter)	94

Maize (green), also known as silage maize, is primarily grown as a forage crop for livestock. Unlike grain maize, it is harvested earlier in the season, usually between mid-September and early October, while still green, in order to preserve its nutritional value as silage. This crop is characterized by its rapid biomass accumulation and tall canopy structure, which typically results in high LAI values during peak growth. In WOFOST simulations, maize (green) exhibits a strong sensitivity to temperature and radiation, with a relatively short growth cycle compared to grain varieties. However, a key limitation is that WOFOST simulates the full crop cycle until physiological maturity, and does not account for early harvest practices typical of silage maize in the Netherlands. As a result, the model may overestimate the actual growing duration and final biomass. In contrast, remote sensing can capture the actual phenological status of the crop, including abrupt changes in canopy cover caused by early harvest, making it a valuable complementary tool for monitoring maize (green) development and refining model outputs.

Winter barley, on the other hand, in contrast, is a cool-season cereal sown in autumn and harvested the following summer. It is well-adapted to temperate climates and contributes to both grain production and livestock feed. Due to its early sowing (around September to October), it experiences a dormant phase during winter and resumes growth in spring. The crop typically reaches its maximum LAI in late spring to early summer. Its long growing period makes it an important crop for soil cover and erosion control during the non-growing season of many summer crops.

Together, these two crops represent distinct phenological patterns and land surface dynamics, providing a valuable contrast for crop growth simulation, yield estimation, and remote sensing-based data assimilation in this study.

3

Materials and Methods

To address the research questions, we designed a research methodology focuses on three main components (Figure 3.1): (1) **Workflow design** focuses on data preparation and integration, including compiling climate, soil, crop type, and human-activity datasets, deriving crop-relevant functional traits from satellite observations, and integrating them into a process-based crop growth model; (2) **Workflow testing** for sensitivity analysis, including defining and testing scenarios by varying observation uncertainties, the number/timing of observations, and the set of assimilated variables; (3) **Workflow validation** for comparing simulated yields with reported yield statistics to estimate uncertainties, identifying optimal assimilation strategies, and testing model transferability to other sites. Each of these components will be described in detail in the following sections.

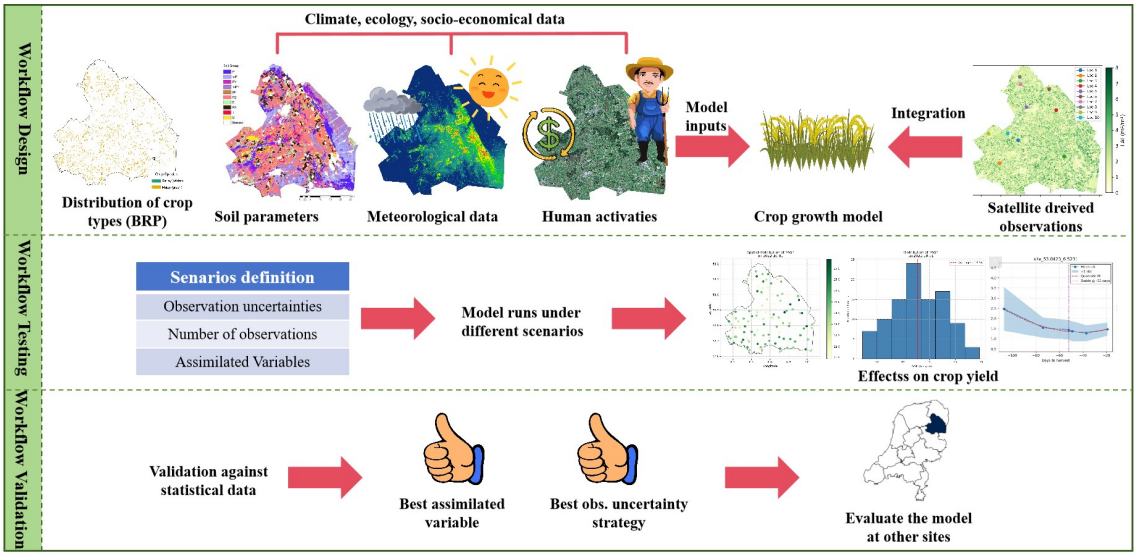

Figure 3.1: Proposed framework for integrating remote sensing data into a crop growth model for yield evaluation.

3.1. Workflow Design

This section outlines the experimental framework used to estimate crop yields by integrating remote sensing and crop growth modeling. The overall workflow comprises five main steps: data pre-processing, open-loop crop growth modeling, satellite parameter retrieval, model monitoring integration through data assimilation (Figure 3.2).

In the first step, meteorological and remote sensing data were collected and preprocessed, including cloud filtering and variable extraction from GRIB-format weather files. The second step involved simulating green maize and winter barley growth using the WOFOST model, parameterized with field-specific inputs and evaluated for sensitivity. Biophysical parameters, i.e., LAI, CCC, and CWC were retrieved from Sentinel-2 imagery in the third step using the SNAP toolbox. The fourth step applied the EnKF to assimilate biophysical observations into WOFOST simulations, using perturbed parameter ensembles and time-varying observation uncertainties. Finally, model outputs were validated against independent observations to assess predictive performance. The goal was to ensure that the simulation error (RMSE) remained within an acceptable threshold (≤20% MAE) before final interpretation of results.

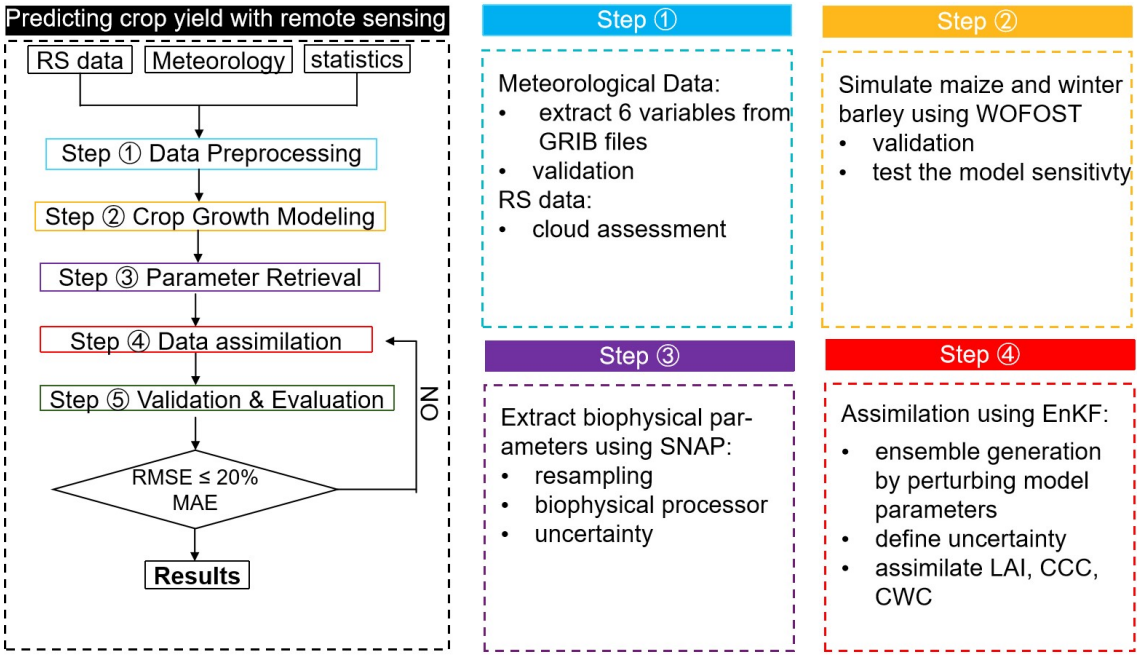

Figure 3.2: Overview of the experimental workflow for crop yield estimation using remote sensing and crop growth modeling.

3.1.1. Meteorological Data

The meteorological data used in this study were obtained from the HARMONIE-AROME Cy43 reforecast dataset, provided by the Royal Netherlands Meteorological Institute (KNMI). This dataset provides high-resolution weather model outputs at a spatial resolution of 2×2 km covering the Netherlands, and is made available through the KNMI Data Platform ((KNMI), 2024a, 2024b). It provides a consistent and spatially detailed representation of meteorological variables essential for crop growth modelling.

The dataset consists of four files per day, each corresponding to a different initialization time: 00:00,

06:00, 12:00, and 18:00. Each file contains forecasts extending up to 60 hours at hourly intervals (e.g., T+1h, T+2h, ..., T+60h). For the purposes of this study, only the 0-hour forecast step was retained to represent the daily observed meteorological conditions. The files are in GRIB format, which is commonly used for weather model outputs and supports efficient storage and access to multi-dimensional meteorological data.

To ensure compatibility with the WOFOST crop growth model, the raw meteorological variables obtained from the KNMI reforecast dataset were transformed into daily values following specific procedures (Table 3.1). Hourly temperature data were used to extract the daily minimum and maximum temperatures, which are required as separate inputs in WOFOST. Wind speed was calculated from the U and V vector components using the Euclidean norm. Precipitation and global radiation values were derived from GRIB files ending with `00500_GB`, which represent 6-hour accumulated values. Actual vapor pressure is obtained from relative humidity and saturated vapor pressure calculated through the Goudriaan equation A. De Wit et al., 2020. The formulas are as follows:

$$H_R = \frac{e_a}{e_s} \times 100\% \tag{3.1}$$

$$e_s = 0.610588 \times \frac{17.32491 \times T}{T + 238.102} \tag{3.2}$$

where H_R is the relative humidity (%), e_a and e_s represent the actual vapor pressure (kPa) and the saturated vapor pressure (kPa), respectively. T is the air temperature (°C).

These were summed to obtain daily totals. This harmonized processing ensures that all input variables conform to the daily resolution and physical format expected by the WOFOST simulation framework.

Table 3.1: Mapping of meteorological variables from KNMI to WOFOST inputs

KNMI Variable	**WOFOST Input**	**Conversion Method**
Temperature [°C]	Daily max/min temperature [°C]	Extract daily minimum and maximum from hourly temperature bands
Temperature [°C] and RH [%]	Mean daily vapor pressure [hPa]	Equation 3.1 and 3.2
U-/V-wind components [m/s]	Mean daily wind speed [m/s]	$\sqrt{U^2 + V^2}$
Precipitation [mm/6h]	Daily precipitation [mm/day]	Daily accumulated mean from GRIB files ending with `00500_GB`
Global radiation [J/m²/6h]	Daily global radiation [J/m²/day]	Daily accumulated mean from GRIB files ending with `00500_GB`

3.1.2. Crop Growth Model Configuration

The WOFOST crop model was implemented using the PCSE (Python Crop Simulation Environment) framework (“PCSE Documentation”, n.d.). Daily weather inputs, including global radiation, maximum and minimum temperature, vapor pressure, wind speed, and precipitation, were derived from the KNMI

reanalysis dataset and converted to WOFOST-required variables as described in Section 3.1.1.

Soil properties were defined using default profile files provided by the PCSE library, specifically the `ec1.soil` configuration, which describes a coarse-textured soil type ("PCSE Documentation", n.d.). These standard soil files include parameters such as field capacity, wilting point, and rooting depth and are suitable for water-limited simulations. No site-specific calibration of soil properties was conducted.

Crop-specific parameter files were sourced directly from the official WOFOST crop library, that is, `maize_green_201` for maize (green) and `winter_barley_301` for winter barley. These files contain detailed phenological, morphological, and physiological characteristics of the crops. No modifications were made to the crop parameters, except for the definition of sowing and harvest dates, which were specified at the parcel level based on typical cropping calendars in Drenthe. The growth and development of crops in WOFOST are primarily governed by a set of physiological parameters that control the rate and extent of biomass accumulation, phenological progress, and canopy development. In this study, key parameters from the official WOFOST crop library were used without modification, including:

- **TSUM1** and **TSUM2**: the thermal time requirements (in °C·day) from emergence to anthesis, and from anthesis to physiological maturity, respectively. These parameters determine the length of the vegetative and reproductive stages.
- **SPAN**: the average lifespan of leaves in days, influencing the rate of senescence and the duration of active photosynthesis.
- **TDWI**: the initial dry weight of the plant at emergence (kg/ha), serving as the starting biomass for the simulation.

These parameters were selected as representative indicators of crop development and canopy dynamics, and they play a key role in determining the simulated time series of LAI and yield. They are summarized in Table 3.2. One thing notable here is that although the parameters VERNBASE (minimum vernalization days) and VERNSAT (saturated vernalization days) are listed as phenological parameters for green maize, they do not affect the simulation because maize is a summer crop that does not require vernalization.

Table 3.2: Key crop parameters used in WOFOST simulations

Parameter	Description	Maize (green)	Barley (winter)
TSUM1 (°C· day)	Thermal time from emergence to anthesis.	695	685
TSUM2 (°C· day)	Thermal time from anthesis to physiological maturity.	800	812
VERNBASE (day)	Base vernalization requirement.	14	9.3
VERNSAT (day)	Saturating vernalization requirement.	70	46

Note. Vernalization parameters mainly affect winter cereals; values for non-vernalizing crops are typically ignored by the model logic.

Due to the large number of maize (green) parcels in the study area, a k-means clustering algorithm was applied to select a representative subset. Based on the spatial and agronomic attributes, 100 representative maize parcels were selected from the full set. In total, simulations were conducted at the parcel level for 100 maize and 94 winter barley fields during their respective 2022 growing seasons.

3.1.3. Satellite Parameter Retrieval

In this study, Sentinel-2 Level-2A surface reflectance data were used to retrieve canopy biophysical variables over maize and barley parcels in Drenthe, were acquired from the Copernicus Open Access Hub (“Copernicus Browser”, n.d.). Images were filtered to retain only those with less than 20% cloud cover over the study area. After quality control, a total of 26 cloud-free or low-cloud-cover images were available during the study period. Specifically, 10 images were acquired within the green maize growing season (25 April - 30 October 2022) and 17 images within the winter barley growing season (14 September 2021 - 30 July 2022). A complete list of selected Sentinel-2 images is provided in Appendix A. These images formed the basis for retrieving crop biophysical parameters for subsequent assimilation.

Three biophysical parameters retrieved from Sentinel-2 imagery were utilized: LAI, CCC, and CWC. All three variables were included as assimilation targets. However, the assimilation framework used LAI as the sole state variable in the EnKF, while CCC and CWC were indirectly constrained via their dependence on LAI.

Leaf Area Index (LAI): LAI, defined as the one-sided green leaf area per unit ground surface area (m^2/m^2), is a key driver of both radiation interception and transpiration in WOFOST. It directly influences the potential gross assimilation rate by controlling intercepted photosynthetically active radiation (PAR). As such, LAI plays a central role in determining crop biomass accumulation and water loss through transpiration.

Canopy Chlorophyll Content (CCC): CCC is calculated as:

$$CCC = LAI \times C_{ab} \tag{3.3}$$

where C_{ab} denotes the average leaf chlorophyll concentration ($\mu g/cm^2$). CCC reflects canopy-level photosynthetic capacity and nitrogen status. Although WOFOST does not explicitly simulate CCC, it is biophysically linked to light use efficiency. In this study, CCC was included as an observational constraint to ensure the physiological realism of the LAI state update.

Canopy Water Content (CWC): CWC is defined as:

$$CCC = LAI \times C_w \tag{3.4}$$

where C_w represents the leaf water content (g/cm^2). CWC is sensitive to canopy moisture status and serves as an early indicator of drought stress or senescence. Similar to CCC, CWC was not directly updated in the model but used as an additional criterion for validating the LAI updates during assimilation.

Sentinel-2 biophysical variables were retrieved using the Biophysical Processor on SNAP. The retrieval process consists of several steps:

1. **Preprocessing and Resampling:** Sentinel-2 Level-2A products were first resampled to a uni-

form 20 m spatial resolution using the SNAP Resampling tool to harmonize spatial grids across bands.

2. **Biophysical Parameter Retrieval:** The resampled data were processed with the SNAP Biophysical Processor (S2 Toolbox), which uses a set of neural networks trained on PROSAIL radiative transfer model simulations to estimate biophysical parameters. These outputs correspond to top-of-canopy variables, representing the green vegetative portion of the canopy.

The retrieval approach and neural network implementation follow the principles outlined in the Algorithm Theoretical Baseline Document (ATBD) for the Sentinel-2 ToolBox Biophysical Processor. The networks estimate variables by minimizing the cost between simulated PROSAIL reflectance spectra and observed reflectance, conditioned on predefined look-up tables and vegetation priors.

To assess the theoretical accuracy of Sentinel-2 derived vegetation biophysical parameters, we refer to Table 3.3, which summarizes the performance metrics of the neural networks used in the SNAP biophysical processor. The table reports the coefficient of determination (R^2) and root mean square error (RMSE) for various products retrieved at 20m resolutions from S2A and S2B imagery.

Table 3.3: Retrieval accuracy of Sentinel-2 biophysical parameters at 20m resolution (adapted from SNAP ATBD).

Variable	**Metric**	**S2A-20m**	**S2B-20m**
LAI	R^2	0.82	0.82
	RMSE	0.90	0.90
CCC (μg/cm^2)	R^2	0.84	0.84
	RMSE	57.99	57.22
CWC (g/cm^2)	R^2	0.84	0.85
	RMSE	0.031	0.023

Among the three variables assimilated in our model, LAI, CCC, and CWC, LAI exhibited a reasonable retrieval accuracy with R^2 ranging from 0.71 to 0.82, and RMSE values between 0.90 and 1.15. For CCC, the R^2 values were 0.84, and the RMSE ranged from 57.22 to 57.99 μg/cm^2. Similarly, CWC achieved R^2 values around 0.84–0.85 and RMSEs as low as 0.023 g/cm^2. These retrieval uncertainties directly impact the confidence in model calibration and assimilation performance. Although these metrics were derived under idealized, simulated conditions, they provide a useful benchmark for understanding potential errors in field-scale retrieval. Moreover, by aggregating pixel-level estimates to parcel-level means, we reduce the influence of outliers and spatial noise, thereby improving the robustness of subsequent data assimilation steps.

3.1.4. Data Assimilation Framework

The data assimilation (DA) framework is designed to optimally combine remote sensing observations with process-based crop growth model simulations to improve the accuracy of state and output variables. By integrating observations into the model during the growing season, the framework continuously corrects the model states, thereby reducing errors caused by uncertainties in model parameters, meteorological forcing, and initial conditions. The assimilation process starts with an ensemble of model simulations generated by perturbing model parameters and/or initial states based on prior uncertainty distributions. At each observation date, the EnKF compares simulated variables (e.g., LAI) with satellite-derived observations, and updates the ensemble states according to the Kalman gain.

The updated states are then used as initial conditions for the next simulation step, ensuring that the model trajectory remains close to the observations while respecting the process-based constraints.

The assimilation strategy varies for the three parameters. While LAI is a direct output of the WOFOST model and can be assimilated straightforwardly, CCC and CWC are not explicitly simulated as model state variables. To enable their assimilation, CCC and CWC were expressed as functions of LAI and constant biochemical coefficients (see Eq. 3.3, 3.4), where Cab and Cw are fixed constants for each ensemble member throughout the simulation.

The values of Cab and Cw for each ensemble member were derived from the distribution obtained by dividing remotely sensed CCC and CWC by LAI at corresponding observation dates. From these empirical distributions, a value is randomly drawn and assigned to each ensemble member at initialization, and remains fixed during assimilation. This design ensures that updates to CCC and CWC are implemented indirectly by updating LAI through the assimilation algorithm, while maintaining physical consistency with the model structure. The statistical characteristics of the Cab and Cw distributions are summarised in Table 3.4.

Table 3.4: Statistical characteristics of the Cab and Cw distributions derived from remotely sensed CCC and CWC divided by LAI.

Parameter	**Mean**	**Standard deviation**
Cab (μg cm^{-2})	112	106
Cw (g cm^{-2})	0.036	0.031

The observation error covariance matrix $\mathbf{R}$ plays a crucial role in the Ensemble Kalman Filter by determining the relative weight assigned to the observations during the assimilation step. An accurate specification of $\mathbf{R}$ is essential to balance observational reliability against model uncertainty. In this study, $\mathbf{R}$ was implemented as a diagonal matrix, assuming that observation errors at each assimilation timestep are uncorrelated in time. In addition, we examined the sensitivity of the assimilation results to different specifications of $\mathbf{R}$, as discussed in Section 3.2.1. The baseline configuration of $\mathbf{R}$ was defined using the observation error variances of the assimilated variables, computed from their total uncertainties. For each variable, the standard deviation of the observation error, σ_o was calculated as:

$$\sigma_o = \sqrt{0.7\,\sigma^2_{\text{spatial}} + 0.3\,\sigma^2_{\text{algo}}} \tag{3.5}$$

where σ_{spatial} represents the spatial variability of the retrievals within the observation footprint, and σ_{algo} is the algorithmic retrieval error. The weights (0.7 for spatial variability and 0.3 for algorithmic error) were selected to balance the contribution of the two components, given that the algorithmic error values are generally larger than the spatial variability estimates (see Table 3.3). This weighting ensures that neither source of uncertainty dominates the total observation error. The corresponding observation error variances (σ_o^2) form the diagonal elements of $\mathbf{R}$ in the baseline configuration.

To account for uncertainty in model parameters and initial conditions, an ensemble of WOFOST simulations was generated by perturbing a set of physiologically meaningful variables related to crop growth and soil properties. For each ensemble member, these variables were sampled from normal distributions centered on reference values with specified standard deviations. The perturbation strategy aimed to reflect plausible variability in crop traits and soil conditions across fields.

Table 3.5 lists the perturbed parameters used for silage maize, along with their assumed mean and standard deviation. All parameters were sampled independently. Where applicable, physical bounds were imposed using truncation to ensure biologically reasonable values (e.g., TDWI constrained between 30 and 150 g m^{-2}).

Table 3.5: Perturbed parameters and distributions for silage maize ensemble simulations.

Parameter	Description	Distribution (mean $\pm$ std)
TDWI	Initial dry weight of the crop (g m^{-2})	$\mathcal{N}(60,\ 30)$, clipped [30, 150]
WAV	Weight of storage organs per seed (g)	$\mathcal{N}(10,\ 5)$
SPAN	Lifespan of leaves (days)	$\mathcal{N}(33,\ 5)$
TSUM1	Thermal time until anthesis (°C·d)	$\mathcal{N}(695,\ 50)$
TSUM2	Thermal time from anthesis to maturity (°C·d)	$\mathcal{N}(800,\ 50)$
CVL	Carbohydrate conversion efficiency: leaves	$\mathcal{N}(0.68,\ 0.2)$
CVO	Carbohydrate conversion efficiency: storage organs	$\mathcal{N}(0.67,\ 0.1)$
CVR	Carbohydrate conversion efficiency: roots	$\mathcal{N}(0.69,\ 0.1)$
SMW	Soil moisture content at wilting point (m^3 m^{-3})	$\mathcal{N}(0.30,\ 0.03)$
SMFCF	Soil moisture content at field capacity	$\mathcal{N}(0.46,\ 0.04)$
SM0	Initial soil moisture content	$\mathcal{N}(0.57,\ 0.057)$

The ensemble size N was set to 40 in this study, balancing computational efficiency with the need for robust statistical representation of forecast uncertainty. While larger ensembles generally improve the accuracy of the forecast error covariance matrix $\mathbf{P}_f$, they also impose higher computational costs, especially when simulations are run at the parcel level across multiple time steps. Previous studies in environmental modeling have shown that ensemble sizes between 20 and 50 are often sufficient to capture the major sources of variability without excessive sampling noise. Preliminary sensitivity tests conducted in this study indicated that increasing N beyond 40 yielded only marginal improvements in assimilation performance, justifying the chosen ensemble size for practical use.

3.2. Workflow Testing

To evaluate the robustness of the crop yield prediction workflow, three sensitivity analyses were conducted. All experiments were carried out on green maize fields, since it is a major crop in the study area. A key consideration is the definition of the harvest date. For green maize, the actual harvest typically occurs before the DOM estimated by the crop model, as the crop is harvested at an earlier stage of development. To ensure consistency with field management practices and to provide realistic yield estimates, the harvest date was therefore explicitly defined, and yield was assessed at this point rather than at DOM. The sensitivity analysis was organized along three dimensions: (1) sensitivity to observation uncertainty, (2) sensitivity to the number of assimilated observations, and (3) sensitivity to the choice of assimilated variables. This design allows for a systematic evaluation of how uncertainties in observational data, data availability, and variable selection influence assimilation outcomes and yield predictions.

3.2.1. Sensitivity to Observation Uncertainty

We assessed how the assumed LAI observation uncertainty influences the EnKF analysis. Each experiment used an ensemble of 30 members and a common assimilation window from 2022-04-25 to 2022-10-30 for green maize; meteorology, soil, and management were identical across runs.

For every satellite overpass, the LAI observation at the field coordinate was computed as the mean of valid pixels inside an $N \times N$ window ($N \in \{1, 5, 7\}$). The associated observation standard deviation σ_o combined a spatial representativeness term, σ_{spatial} (the standard deviation of valid pixels within the window), and an algorithmic retrieval term, as defined in Eq. 3.5. We tested five scenarios:

- **S1**: window 5×5 (baseline).
- **S2**: window 5×5 with uncertainty inflation ($\sigma_o \times 2$).
- **S3**: window 10×10 (no spatial variability, retrieval error only).
- **S4**: window 3×3 (smaller representativeness error).
- **S5**: window 1×1 (no spatial variability, retrieval error only).

These scenarios were designed to systematically evaluate the sensitivity of the EnKF analysis to assumptions about observation uncertainty and spatial representativeness. The baseline configuration (S1) uses a 5×5 window, representing a balance between capturing local heterogeneity and maintaining a sufficient number of valid pixels for robust LAI estimation. Scenario S2 applies an artificial inflation of σ_o to test how the assimilation performance responds when the observations are assumed to be less reliable, thereby assessing the impact of overestimated observation errors. In contrast, S3 adopts a larger 10×10 window, reducing the spatial representativeness error but potentially increasing the mismatch between satellite-derived LAI and field-scale conditions due to greater spatial averaging. S4 uses a smaller 3×3 window to explore the effect of reduced sub-pixel heterogeneity on assimilation accuracy. Finally, S5 isolates the impact of retrieval uncertainty alone by using a single-pixel estimate (1×1) and neglecting spatial variability entirely. Together, these scenarios provide a controlled framework to understand how different uncertainty assumptions influence the assimilation outcome.

3.2.2. Sensitivity to Number of Observations

Accurate crop-state estimation through data assimilation depends not only on the quality of individual observations but also on their number and timing. In practice, optical satellite data are often irregular in time due to cloud contamination and acquisition gaps, making it essential to understand how many observations are needed to meaningfully constrain crop growth dynamics. This experiment was therefore designed to quantify how the number and temporal distribution of assimilated LAI observations influence the effectiveness of the EnKF analysis and its predictive performance. In particular, we evaluate both the marginal benefit of each additional assimilation date and the point of diminishing returns, which provides practical insights for optimizing satellite acquisition strategies and operational crop monitoring.

We quantify how the number and timing of assimilated LAI observations affect the EnKF analysis and key outputs (LAI trajectory and harvest TAGP) for green maize.

Across all experiments, we assimilate only LAI with an Ensemble Kalman Filter (30 members) over the period 2022-04-25 to 2022-10-30. Meteorology, soil, management and crop parameters are identical across experiments. Observation uncertainty follows our baseline error model (Sec. 3.2.1): the per-datum standard deviation σ_o is the quadratic sum of a spatial representativeness term and a retrieval term, and the observation-error covariance R is diagonal.

For this site–year we retained 6 Sentinel-2 LAI observations for assimilation. We excluded the earliest overpass because it occurred at a very early phenological stage (LAI near zero, low information content), and we discarded the last three overpasses because they fell after the harvest date and thus lay outside the crop cycle. Formally, we assimilated only dates within the in-season window,

$$S(\mathcal{O}) = \{\, t_i \in \mathcal{O} \mid t_{\mathrm{em}} < t_i \le t_{\mathrm{harv}} \,\}, \qquad |S(\mathcal{O})| = 6, \tag{3.6}$$

where t_{em} and t_{harv} denote (simulated or observed) emergence and harvest dates, respectively.

To assess the effect of observation count, we progressively increased the number of assimilated dates. Starting from the first available in-season observation, we ran the full simulation using only that single assimilation date and recorded the resulting LAI and TAGP at harvest. We then repeated the simulation while adding the next chronological observation, continuing until all six observations were assimilated. For each scenario, we also computed the ensemble standard deviation of LAI and TAGP at the harvest date to evaluate whether additional observations reduce output uncertainty. This approach allows us to quantify both the marginal benefit of each additional assimilation date and the point of diminishing returns.

3.2.3. Sensitivity to Assimilated Variables

Data assimilation performance depends strongly on which biophysical variables are assimilated, since different remotely sensed variables provide complementary information about crop canopy status. For example, LAI primarily constrains canopy structure, CCC reflects photosynthetic capacity and nitrogen status, and CWC captures plant water content and stress. Understanding how assimilating each variable individually, or in combination, influences the model's predictive skill is therefore essential for designing efficient assimilation strategies and optimizing the use of available satellite products. This experiment was thus designed to evaluate the relative contributions of LAI, CCC, and CWC observations to improving state estimation and yield forecasting.

Different remotely sensed variables carry different types of information on crop canopy condition and may influence the assimilation outcome in distinct ways. As described in Section **??**, we expressed CCC and CWC as the product of LAI and a constant biochemical coefficient, i.e., Cab or Cw, which is fixed for each ensemble member throughout the simulation. These coefficients were sampled at initialization from empirical distributions derived by dividing the remotely sensed CCC or CWC by LAI, and their statistics are given in Table 3.4. This approach allows CCC and CWC to be indirectly updated via LAI adjustments during assimilation. We tested several assimilation configurations: LAI only, CCC only and CWC only. In all experiments, the meteorology, soil, management, and crop parameters were identical, and observation uncertainty followed the baseline error model (Sec. 3.2.1). For each configuration, we evaluated the effect on LAI and TAGP trajectories and harvest TAGP, and the ensemble standard deviation of these variables at harvest, to quantify the relative benefits of assimilating different

variables or combinations thereof.

3.3. Workflow Validation

3.3.1. Validation Data

For validation, we rely on official agricultural statistics from Statistics Netherlands (CBS). In the Dutch system, crop areas and yields are self-reported by farmers (via annual agricultural returns) and consolidated by CBS together with administrative registers and expert checks before publication. We made extensive efforts to obtain parcel-level observations for independent validation. However, because the underlying parcel-level microdata are access-restricted, we could not obtain field-by-field observations for our study area. We therefore validated our results against province-level CBS statistics available through the StatLine portal (e.g., Arable crops; production, region, code 85636ENG), which provide long time series of harvested area, yield, and production for major arable crops. To ensure a like-for-like comparison, model outputs were aggregated from parcels to the corresponding province–year units. While this approach offers an authoritative benchmark, it also implies that any field-scale errors may be partially masked by spatial aggregation, a limitation we acknowledge in the discussion.

3.3.2. Evaluation Methodology

Model performance was evaluated using official provincial statistics from CBS as an independent benchmark. Since only a single province-level observation was available for the 2022 growing season, metrics based on temporal or spatial correlation (e.g., R^2) are not applicable.

Instead, as only the aggregated average yield across all fields was available from official statistics, the validation focused on metrics that measure the agreement between the model estimates and the observed mean at the aggregated level. Four complementary indicators were employed: aggregated bias, relative bias, standardized bias (z-score), and root mean square error (RMSE).

Aggregated bias quantifies the difference between the mean simulated yield and the observed average yield, providing a direct measure of the overall deviation. It is defined as:

$$\text{Bias} = \bar{y}_{\text{model}} - \bar{y}_{\text{obs}} \tag{3.7}$$

where $\bar{y}_{\text{model}}$ is the mean yield simulated across all fields and $\bar{y}_{\text{obs}}$ is the observed mean yield. A smaller absolute value of bias indicates that the model estimates are closer to the reference value.

To allow for a scale-independent comparison, the relative bias (%Bias) was also calculated by normalizing the aggregated bias with respect to the observed mean:

$$\%\text{Bias} = \frac{\bar{y}_{\text{model}} - \bar{y}_{\text{obs}}}{\bar{y}_{\text{obs}}} \times 100\% \tag{3.8}$$

This metric expresses the deviation as a percentage, enabling direct interpretation of overestimation or underestimation relative to the observed average.

Furthermore, a standardized bias (z-score) was used to statistically evaluate whether the simulated

mean differs significantly from the observed mean. It is calculated as:

$$z = \frac{\bar{y}_{\text{model}} - \bar{y}_{\text{obs}}}{SE} \tag{3.9}$$

where $SE = \frac{s}{\sqrt{n}}$ is the standard error of the simulated mean, s is the standard deviation among field-level simulations, and n is the number of fields. A $|z|$ value smaller than 1.96 indicates that the simulated mean is not statistically different from the observed mean at the 95% confidence level.

Finally, the root mean square error (RMSE) was calculated to quantify the overall deviation of field-level simulations from the observed mean yield:

$$\text{RMSE} = \sqrt{\frac{1}{n}\sum_{i=1}^{n}(y_i - \bar{y}_{\text{obs}})^2} \tag{3.10}$$

where y_i is the simulated yield for field i.Although individual field observations were unavailable, this metric provides an aggregated measure of how closely the simulated yields cluster around the validation reference. Collectively, these metrics offer a comprehensive evaluation of the assimilation performance in terms of accuracy, relative deviation, statistical consistency, and overall agreement with the observed yield.

This approach provides a consistent evaluation of model skill at the provincial scale, despite the lack of parcel-level validation data.

4

Results

4.1. Results of Workflow Design

4.1.1. Spatial and Temporal Patterns of Climate Variables

To analyze the spatiotemporal variability of meteorological conditions, the mean daily values of six climate variables were calculated for each quarter in 2021–2022: global radiation, maximum and minimum temperatures, vapor pressure, wind speed, and precipitation.

Figures above illustrate the spatial distribution of six climate variables in each quarter. Overall, the maps reveal distinct spatial gradients and seasonal variations:

Temperature: Both maximum and minimum temperatures tend to be higher in the southern part of Drenthe. Several localized hotspots are also observed around built-up areas such as Assen and Emmen. These elevated temperature zones may be attributed to urban heat island effects and reduced vegetation cover in these urbanized regions.

Global Radiation: A consistent south–north gradient is observed, with higher radiation in the southern part of the province and lower values in the northern side.

Vapor Pressure: The spatial distribution of vapor pressure does not exhibit a strong or consistent spatial pattern across the province. However, a general trend of slightly lower vapor pressure in the interior compared to the peripheral regions can be observed, which may relate to localized land cover and topographic influences. Seasonally, vapor pressure is highest in Q3, reflecting increased atmospheric moisture during the warmest period of the year, and is lowest in Q1 and Q4, consistent with colder and drier winter and autumn conditions.

Wind Speed: Wind speed displays clear spatial heterogeneity across Drenthe. Lower wind speeds are observed in several interior zones of the province, which spatially correspond to forested areas such as Dwingelderveld and Drentsche Aa National Parks. These vegetated regions likely reduce surface wind through increased surface roughness and canopy friction. In contrast, higher wind speeds are

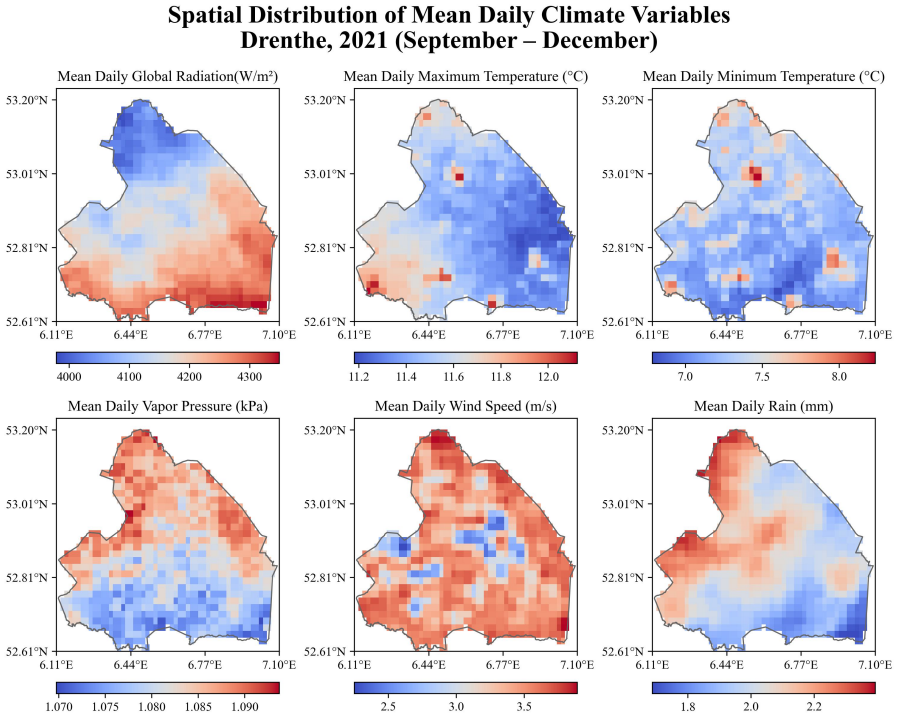

Figure 4.1: Spatial distribution of mean daily climate variables in Drenthe, 2021 (September–December).

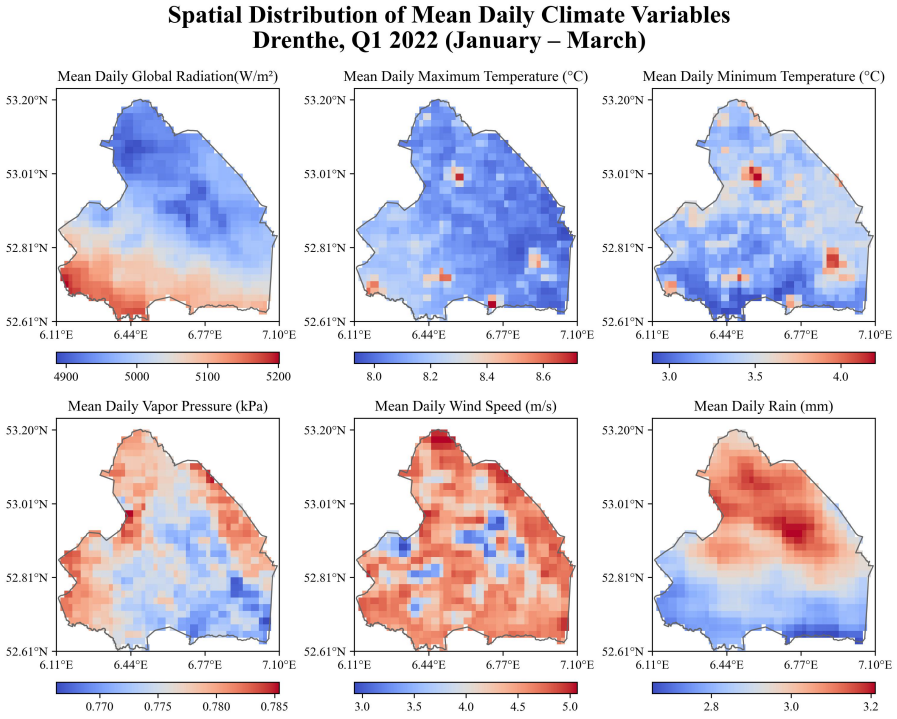

Figure 4.2: Spatial distribution of mean daily climate variables in Drenthe, Q1 2022 (January–March).

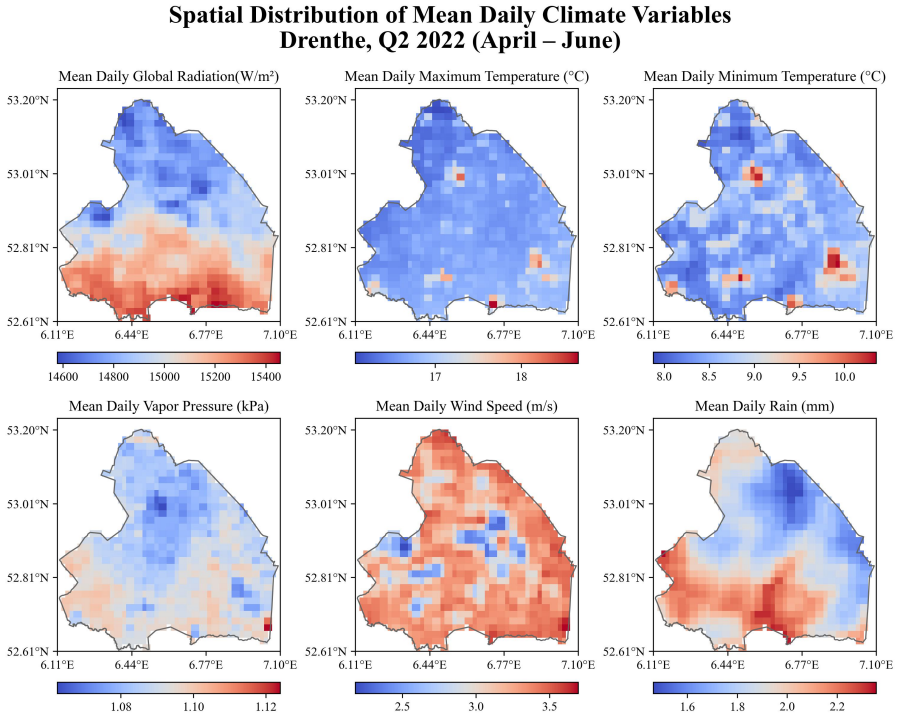

Figure 4.3: Spatial distribution of mean daily climate variables in Drenthe, Q2 2022 (April–June).

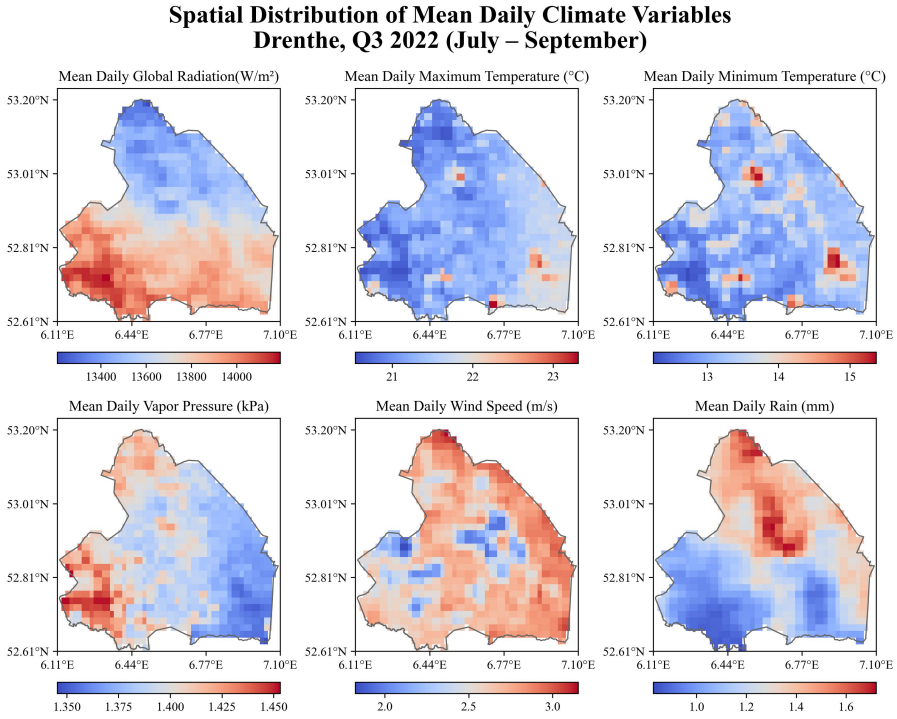

Figure 4.4: Spatial distribution of mean daily climate variables in Drenthe, Q3 2022 (July–September).

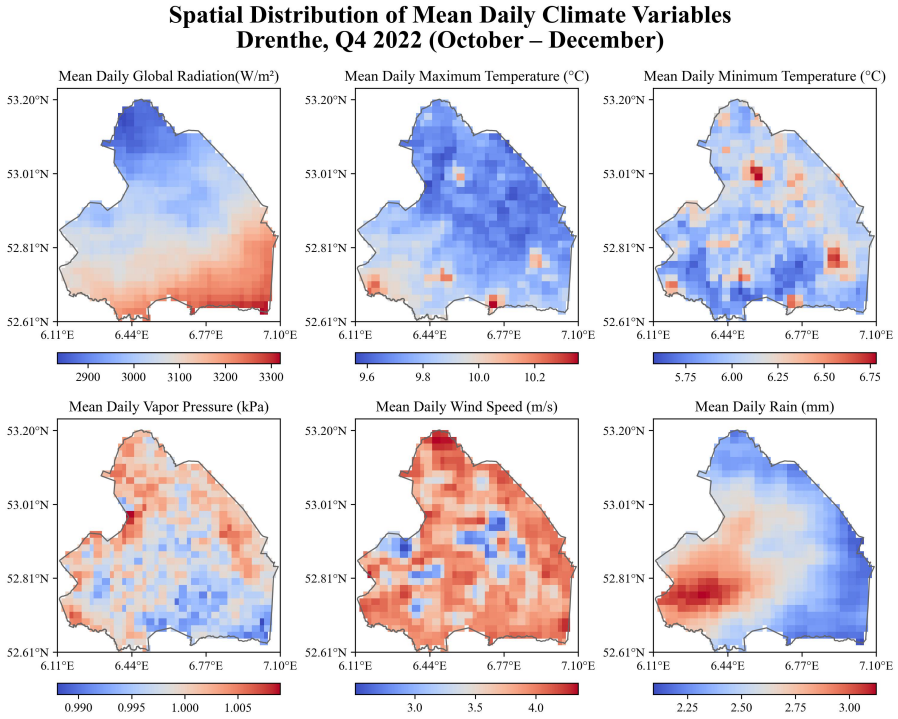

Figure 4.5: Spatial distribution of mean daily climate variables in Drenthe, Q4 2022 (October–December).

seen along the open-field peripheries in the north and southeast. Seasonally, wind speeds peak during winter (Q1) and drop significantly in summer (Q3), reflecting the overall weakening of synoptic-scale winds during the warmer months.

Precipitation: Rainfall patterns vary considerably by quarter. The highest rainfall zones are mostly located in the northern and central parts of Drenthe (e.g., during Q1 and Q3), while the southern zones experience relatively lower rainfall. These spatial disparities can influence local soil moisture availability for crops.

These spatial patterns underscore the heterogeneity of environmental conditions within the study area. Recognizing these differences is critical when simulating crop growth at the parcel level, as microclimatic variation may impact growth rate, water stress, and yield distribution.

We further explored the temporal dynamics of meteorological conditions during the growing seasons. Time series were extracted from two representative adjacent parcels, one cultivated with green maize and the other with winter barley. As shown in Figure 4.6, the plots depict the daily mean values of six climate variables. The shaded bands represent ± 3 standard deviations, calculated from the distribution of all parcels within the study area, to capture overall variability.

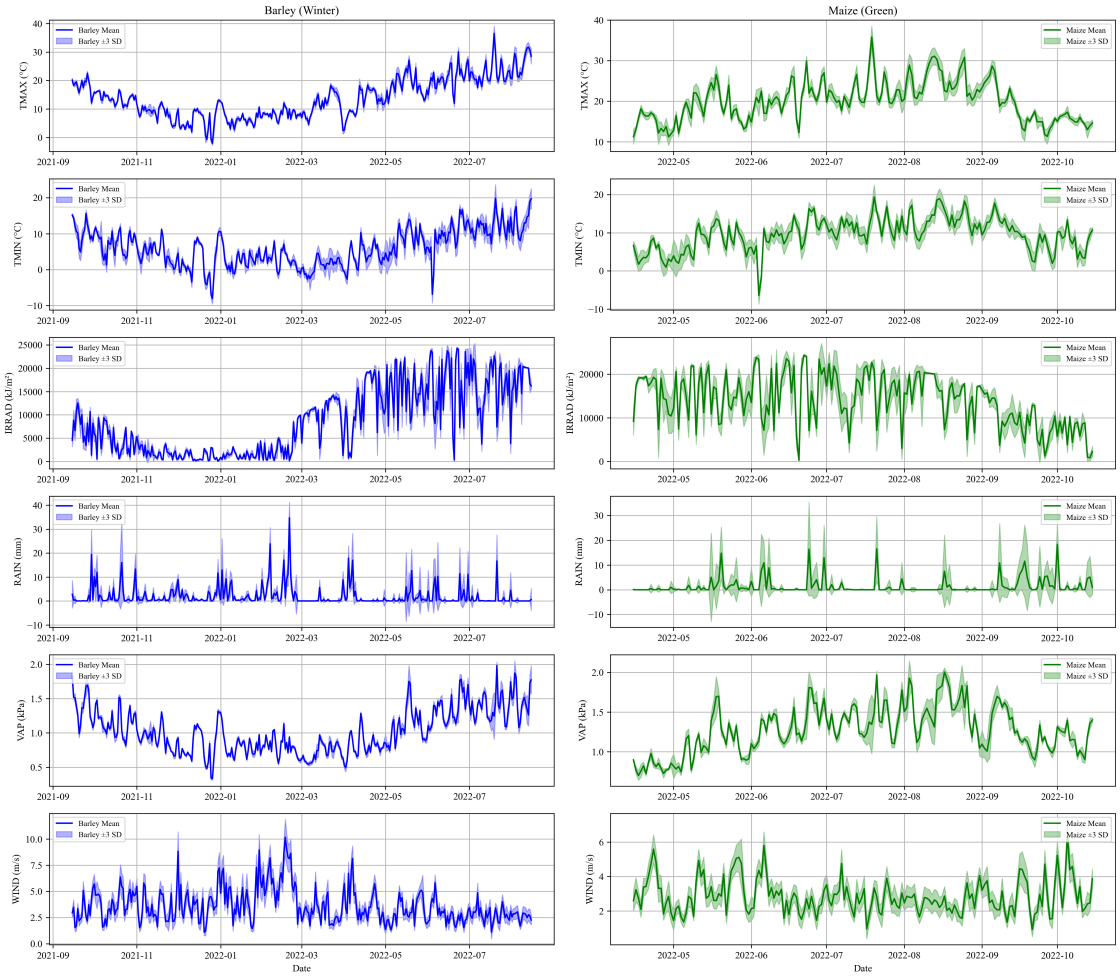

Figure 4.6: Daily meteorological variables averaged over parcels for winter barley (left) and green maize (right) during their respective growing seasons. Shaded areas indicate ± 3 standard deviation.

The patterns reflect seasonal shifts in temperature and radiation, with higher variability in precipitation and wind. Winter barley was sown in autumn and exhibited a long growing cycle into early summer, while green maize was cultivated in a shorter, warmer summer window. These dynamics help contextualize the input conditions for the WOFOST simulations.

4.1.2. Sentinel-2 Derived Biophysical Parameters

The left panel of Figure 4.7 shows a spatial snapshot of Sentinel-2 LAI on 13 August 2022. On that date, LAI ranged from 0.00 to 12.14 across the study area (mean: 2.16; median: 1.91; P5: 0.29; P95: 4.93; $n = 6{,}698{,}479$ valid pixels), revealing pronounced field-scale heterogeneity: high values clustered over intensively cultivated maize fields, while built-up and bare/harvested surfaces exhibited low LAI. LAI in urbanized areas was generally close to zero but not exactly zero, partly due to vegetation in parks, roadside trees, and small garden plots, and partly because of mixed pixel effects where coarse spatial resolution blends non-vegetated surfaces with nearby vegetated areas. These statistics describe the full AOI. In the right panel, we extracted LAI time series for ten selected green maize field locations to capture temporal dynamics at representative crop sites. All sites follow a single-peaked

seasonal trajectory characteristic of maize: low LAI in early season (April–May), rapid canopy development during June–July, a peak around late July to mid–August, and decline with senescence and harvest in September–October. Variations in peak magnitude and timing among locations likely reflect differences in planting dates, cultivar/field management, and local water availability. Notably, while the WOFOST open-loop simulation suggests that the DOM occurs around mid–October, the Sentinel-2 observations indicate that maize harvesting had already commenced by mid–September in many fields, leading to a more rapid decline in LAI than the model predicts.

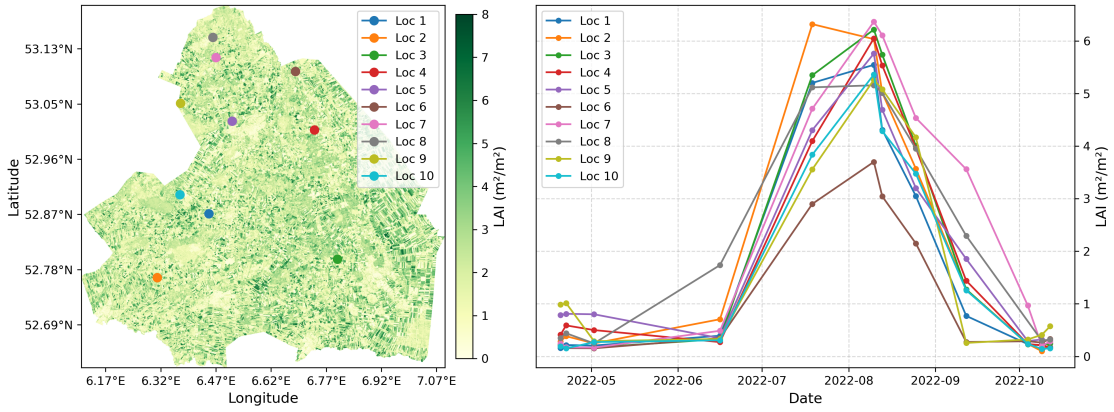

Figure 4.7: **Spatial and temporal patterns of LAI.** *Left:* Sentinel-2 derived LAI spatial distribution on 13 August 2022. *Right:* Seasonal LAI trajectories (April–October 2022) for ten green maize field locations. Locations are colour-coded and labelled consistently between panels.

Similarly, Figure 4.8 and Figure 4.9 illustrates the spatial distribution and temporal dynamics of CCC and CWC for green maize in the study area. The spatial snapshots on 13 August 2022 show that both CCC and CWC exhibit pronounced field-scale heterogeneity: intensively cultivated maize fields present high values, whereas built-up areas, bare soil, and harvested fields display low values. CCC, ranging from 0 to 450 μg cm^{-2}, primarily reflects canopy photosynthetic capacity and nitrogen status. CWC, ranging from 0 to 0.14 g cm^{-2}, is linked to canopy water status and structure.

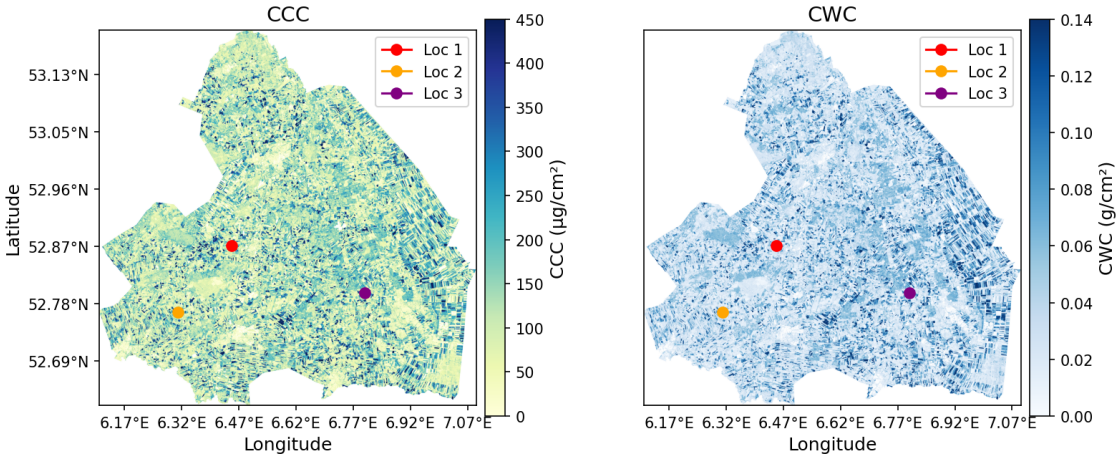

Figure 4.8: *S*entinel-2 derived CCC (left) and CWC (right) spatial distribution on 13 August 2022.

As shown in Figure 4.9, the corresponding time series (April–October) reveal a single-peaked seasonal trajectory for both parameters, characteristic of maize phenology. Values remain low in April–May, increase rapidly during canopy expansion in June–July, and reach a maximum in early-to-mid

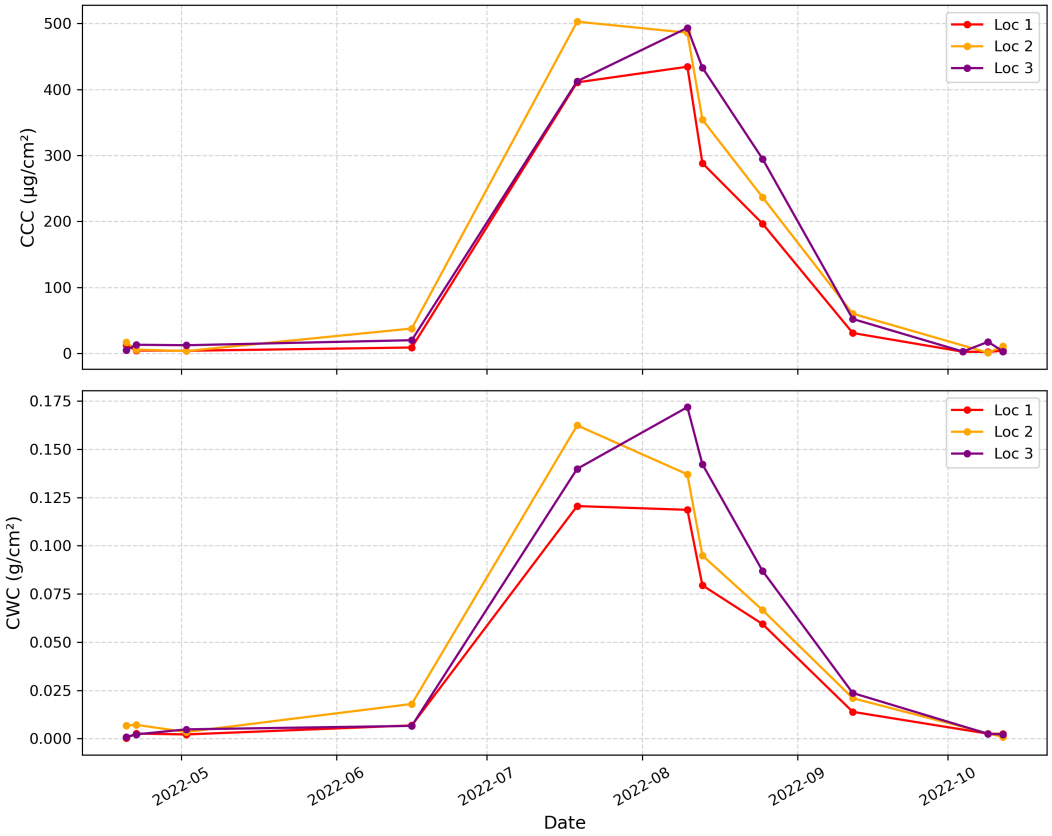

Figure 4.9: Time series of CCC (up) and CWC (low) for ten green maize field locations.

August. CCC peaks occur nearly synchronously with LAI maxima, indicating that leaf area expansion and chlorophyll accumulation progress concurrently. CWC peaks generally coincide with LAI but decline more steeply during September, reflecting rapid water loss during senescence and harvest. The concurrent rise and fall of CCC, CWC, and LAI highlight their coupled biophysical nature, while the faster decline of CWC underlines its sensitivity to physiological and environmental stress.

4.1.3. Open-loop WOFOST Simulations

This section presents the simulation outputs of the WOFOST crop growth model, prior to any data assimilation. Simulations were conducted at the parcel level for 100 green maize fields and 94 winter barley fields in Drenthe during the 2022 growing season. The following subsections describe the spatial and temporal characteristics of simulated LAI, and compare model outputs against Sentinel-2 observations.

To examine the variability in crop development across the study area, we analyzed the maximum simulated LAI (LAI_{max}) and its spatiotemporal distribution. The histogram in Figure 4.10 (top left) illustrates the distribution of LAI_{max} across 100 green maize fields, which ranges from approximately 3.0 to 4.0, with most parcels clustering between 3.4 and 3.8. The spatial distribution map (top right) reveals a clear gradient in LAI_{max}, generally decreasing from the southwestern to the northeastern parts of Drenthe. This pattern closely resembles the spatial distribution of global radiation discussed earlier, suggesting that incoming solar radiation may be a key driver of biomass accumulation. Other contributing fac-

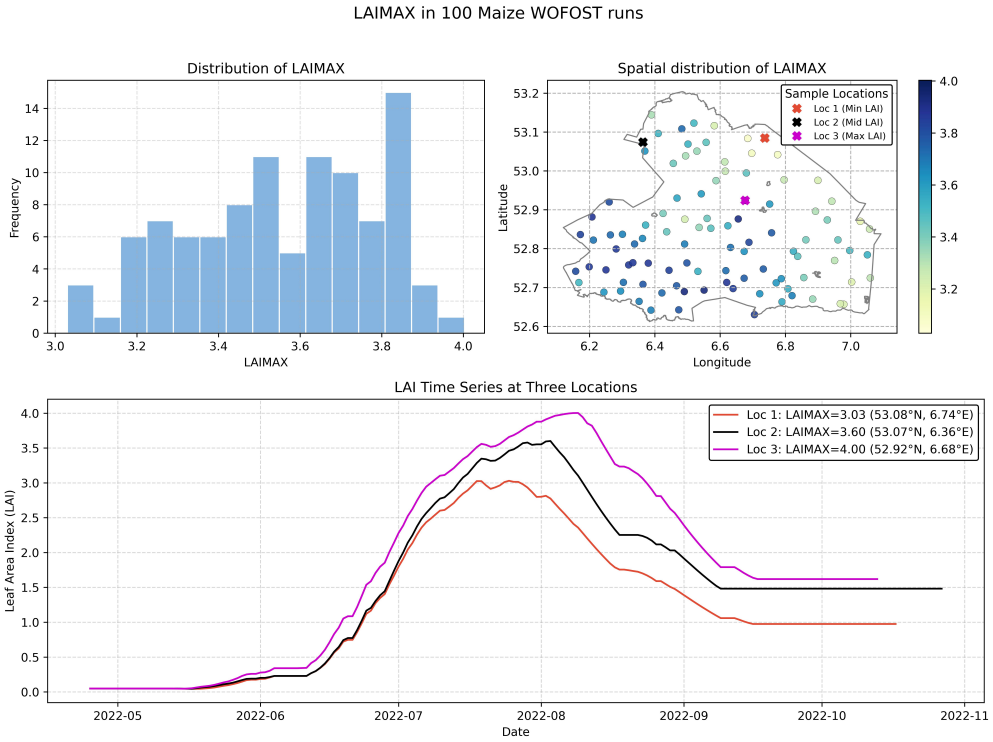

Figure 4.10: Distribution (top left), spatial pattern (top right), and time series (bottom) of LAI_{max} from WOFOST simulations in 100 maize parcels.

tors may include variations in soil water availability. The bottom panel of Figure 4.10 shows LAI time series at three sample locations representing low, medium, and high LAI_{max}. While the timing of LAI peaks is broadly similar across sites, there are notable differences in peak magnitude and curve shape, reflecting spatial heterogeneity.

As shown in Figure 4.11, to evaluate the plausibility of WOFOST-simulated LAI prior to assimilation, model outputs were compared with Sentinel-2 LAI retrievals at three representative locations selected in Figure 4.10. The model reproduces the general seasonal trajectory of LAI, including onset, rapid growth, and decline phases. However, the overall magnitude of simulated LAI is lower than that from Sentinel-2, which may be attributed to model parameter settings that do not fully represent the actual crop growth conditions in the study area, although uncertainties in the remote sensing retrievals cannot be ruled out. Additionally, at the end of the growing season, WOFOST shows a slower decline in LAI, whereas Sentinel-2 captures an abrupt drop. As mentioned before, this mismatch primarily reflects the fact that the model assumes senescence to follow a natural physiological process, while in practice, silage maize is often harvested earlier, leading to a sudden reduction in canopy cover.

These discrepancies emphasize the need for dynamic model updating using satellite observations, which is addressed through the data assimilation framework in the following section.

4.1.4. Data Assimilation Results

Figure 4.12 show the data assimilation results for one site $(52.6501°\mathrm{N}, 6.4941°\mathrm{E})$. The EnKF mean (red) follows the same overall trend as the satellite LAI, with visible but moderate analysis increments at

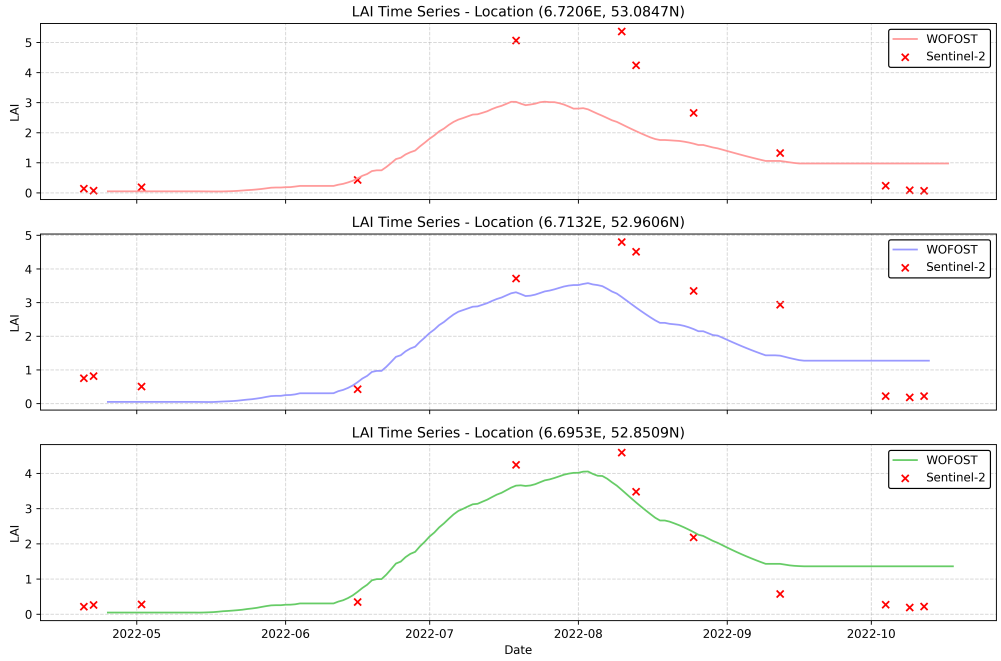

Figure 4.11: LAI time series comparison between WOFOST simulations and Sentinel-2 observations at three selected maize parcels. Red crosses indicate Sentinel-2 derived LAI.

the observation dates (top–right). The ensemble spread contracts immediately after each update and gradually regrows between updates, which represents textbook filter behaviour and indicates that the prescribed observation error and background spread are in reasonable balance.The seasonal pattern is agronomically consistent: a slow increase during early vegetative growth, a rapid ramp-up to a mid-season peak, and a decline during senescence. Because canopy radiation absorption in WOFOST scales with $fAPAR = 1 - \exp(-k\,\mathrm{LAI})$, LAI corrections applied before and around the peak (when LAI is in the 2–4 range) have the largest leverage on downstream fluxes, whereas late-season corrections yield diminishing returns as both $fAPAR$ saturates and leaves senesce.

Total above-ground biomass (TAGP, middle–left) responds smoothly to the LAI updates. Small kinks in TAGP coincide with LAI analysis times, reflecting changes in absorbed PAR and thus daily gross assimilation. The largest TAGP adjustments occur following early and mid-season LAI increments, when additional canopy area substantially increases light interception; after the LAI peak, analysis increments produce smaller TAGP changes because (i) $fAPAR$ is closer to saturation and (ii) senescence shortens the remaining integration window. Importantly, the filter does not induce spurious oscillations or drift: TAGP remains monotonic and within the ensemble envelope, showing that LAI information propagates physically through canopy photosynthesis and allocation rather than forcing the biomass state directly.

For green maize, where harvest output is TAGP, concentrating high-quality LAI observations during the canopy expansion phase and near the seasonal peak maximizes the benefit to biomass prediction, while late-season acquisitions mainly reduce LAI uncertainty with limited effect on TAGP. The stable spread-reduction without collapse suggests no overconfidence; if further TAGP skill is desired, improvements will likely come from (i) tighter LAI errors around peak growth and (ii) refining canopy parameters that control light-use efficiency (e.g., k, $AMAXTB$, $EFFTB$), rather than from increasing the number of late-season updates.

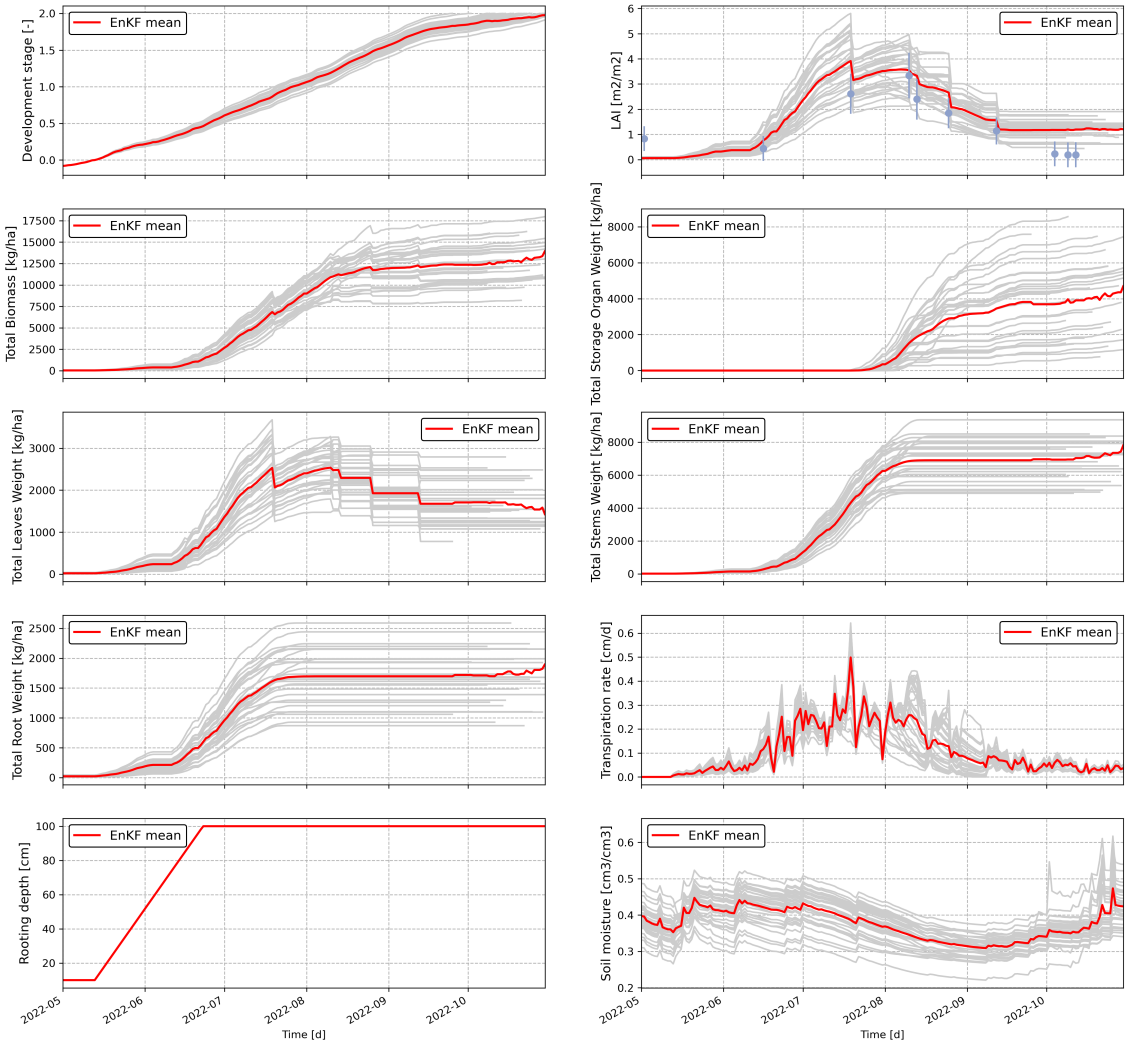

Figure 4.12: Temporal dynamics of crop growth variables under data assimilation

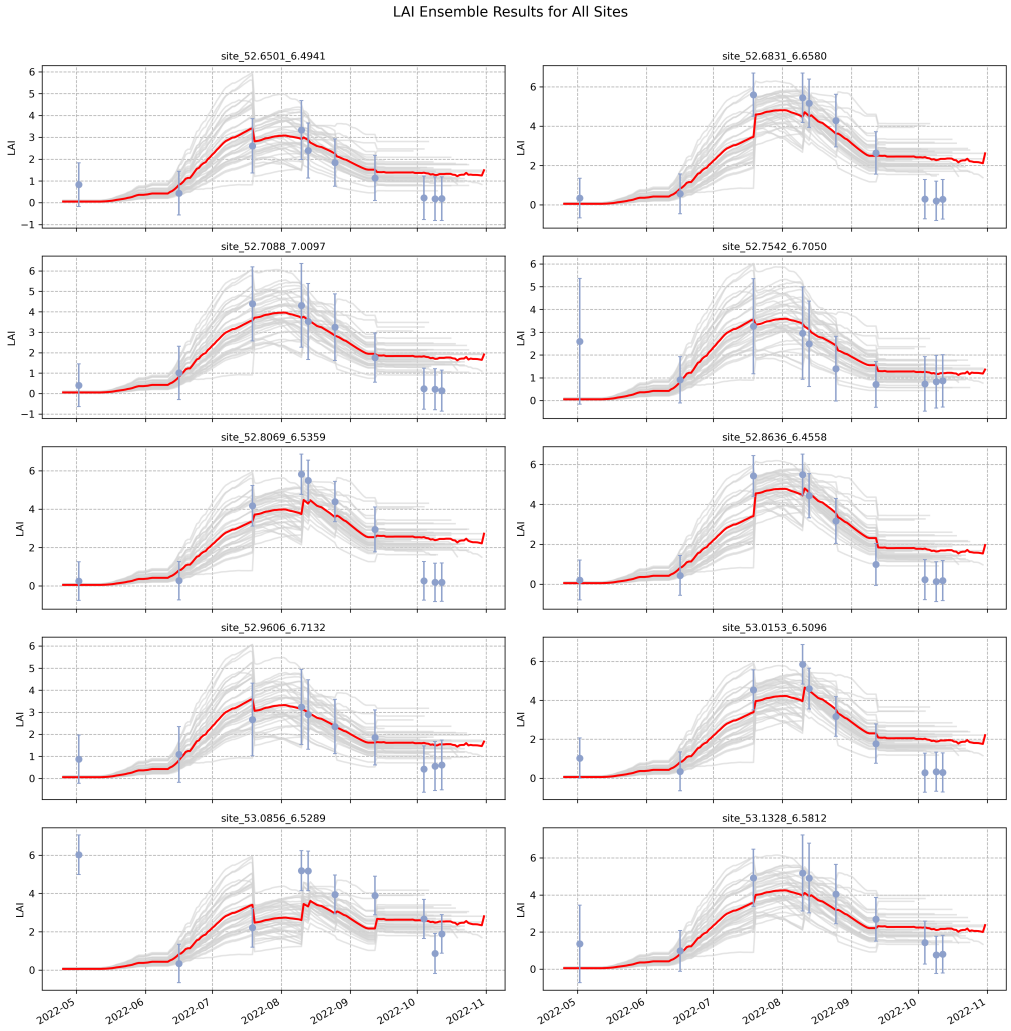

Figure 4.13: Time series of simulated LAI for 10 sites during EnKF.

We further investigate the behavior of LAI during the assimilation process. Figure 4.13 summarises LAI-only EnKF results for ten representative green maize sites. Each panel shows the ensemble trajectories (grey), the EnKF mean (red), and the Sentinel-2 LAI observations with $\pm 1\sigma$ (blue). Across sites, the analysed LAI exhibits a consistent seasonal cycle: a slow increase in early season (May), a rapid rise during canopy expansion, a mid-season peak, and a gradual decline afterwards. Peak LAI typically lies between 3 and 5, with inter-site differences in peak timing of about 2-3 weeks and peak magnitude of roughly ± 1 LAI. Late-season LAI converges to 1-2, consistent with senescence and partial ground exposure. This spatial variability is plausibly driven by soil/management contrasts and mesoscale weather differences rather than filter behaviour.

At most update dates the observations fall within the ensemble envelope, and the ensemble spread contracts immediately after assimilation then re-grows between updates. The analysis increments are moderate, avoiding oscillations; the red curves track the blue points without overfitting. This indicates a reasonable balance between background spread and observation error, and a stable EnKF across all sites. The largest and most systematic adjustments occur around the rising limb and near peak LAI, when corrections most strongly affect absorbed PAR and hence downstream biomass. Post-peak

updates have smaller impact on the trajectory (saturation of $fAPAR$ and ongoing senescence), mainly tightening uncertainty rather than shifting the mean. However, we also observe that the first observation on 2 May 2022 has negligible impact on the analysis. This is because the crop is still in its early growth stage and the associated observation carries large uncertainty. Similarly, the last three observations after 1 October provide little to no effect. At that time, the maize had already been harvested, resulting in very low LAI values, while the process-based model ensemble still maintained nonzero canopy states. Therefore, we consider these three observations ineffective and exclude them from the subsequent sensitivity tests.

We further illustrate the trajectory of TAGP at the same ten sites during the LAI assimilation process, as shown in the Figure 4.14.

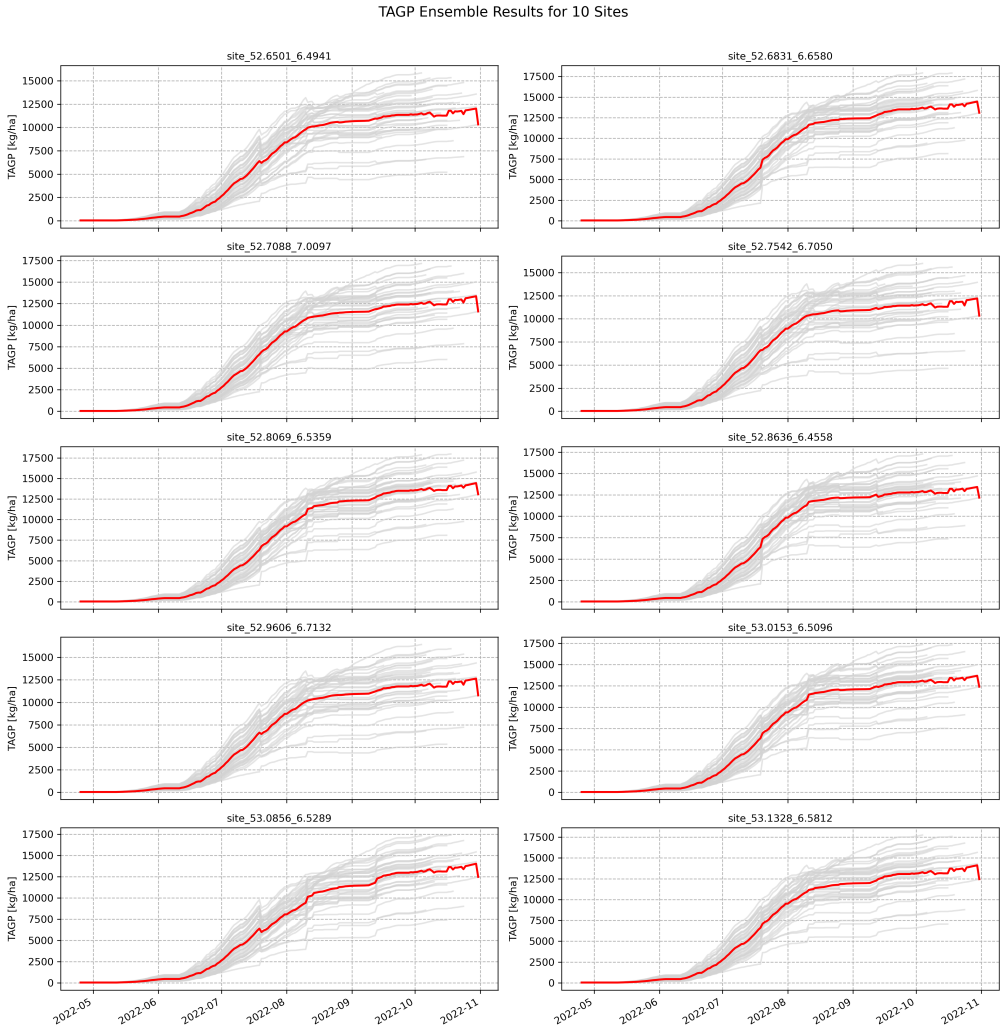

Figure 4.14: Time series of simulated TAGP for 10 sites during EnKF.

Overall, TAGP increases monotonically throughout the growing season, following an agronomically consistent pattern: slow accumulation in the early stage, rapid growth during mid-season, and a plateau after September. The EnKF mean (red) remains within the ensemble envelope and closely follows the ensemble trajectories (grey), indicating a stable assimilation process without spurious oscillations or

drift. During the rapid growth phase (June–August), LAI updates lead to visible adjustments in TAGP, accompanied by a marked reduction in ensemble spread, demonstrating the constraining effect of observations on model uncertainty. In contrast, during the late season (after October), observations have little impact on TAGP, mainly serving to maintain ensemble stability. Noticeable differences are observed across sites, with final TAGP levels ranging from about 12 to 17 $tons/ha$, likely reflecting variations in local meteorological conditions, soil environments, or observational uncertainty. These results highlight that LAI assimilation is most influential for biomass prediction during the vigorous growth stage and also reveal spatial heterogeneity among sites.

TAGP trajectories not only capture the crop growth dynamics but also provide a basis for determining the harvest date. A programmatic analysis across multiple sites showed that around 1 October 2022, the daily increments of TAGP had approached zero and consecutive declines were observed, indicating that above-ground biomass accumulation had essentially ceased and begun to decrease. Since green maize is typically harvested when total biomass is near its maximum rather than at the physiological maturity date (DOM) defined by the crop model, we defined 1 October as the harvest date in this study for subsequent yield evaluation and sensitivity analysis.

With the harvest date, we calculate the TAGP for all the green maize parcels on that day, and plot the spatial distribution and frequency distribution (see Figure 4.26). We find that the harvest TAGP range from 11.5 to 15.5 $tons/ha$, with an average value of 13.56 $tons/ha$. Most parcels cluster within 13–14.5 $tons/ha$, while a few parcels deviate toward lower or higher values. It indicates that the yield estimates after assimilation are overall reasonable and spatially coherent. On the whole, the southern areas exhibit slightly higher TAGP compared to the northern areas. Such spatial variability indicates that even on the same harvest day, the final yield of different fields is still influenced by soil conditions, local climate, and management differences.

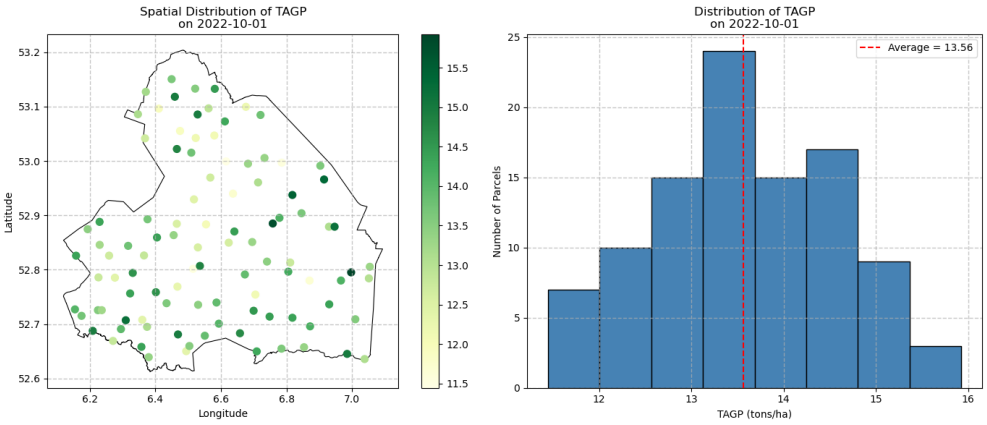

Figure 4.15: Spatial distribution (left) and frequency distribution (right) of TAGP on harvest date.

Furthermore, we explore the relationship between maximum LAI and TAGP. Figure 4.26 shows the spatial distribution of LAIMAX and harvest TAGP. The spatial maps reveal pronounced heterogeneity across parcels, with higher LAI Max generally corresponding to higher TAGP.

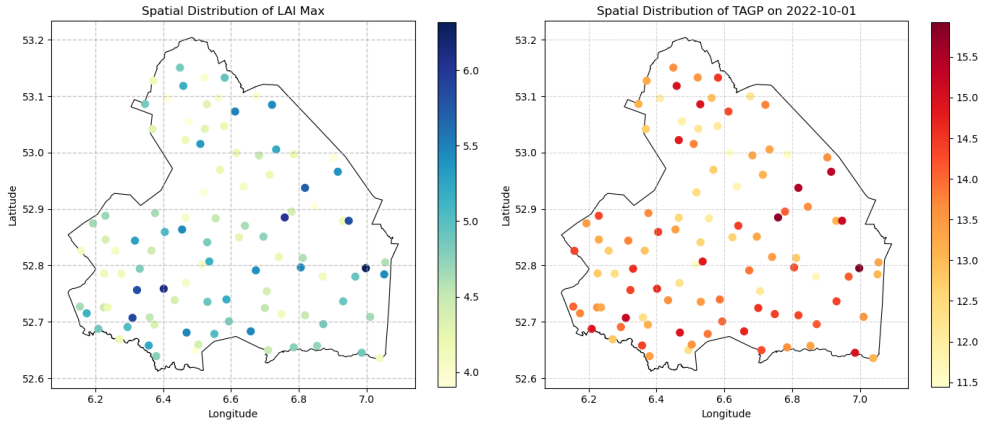

Figure 4.16: Spatial distribution of maximum LAI (left) and TAGP (right) on the harvest date.

The scatter plot further quantifies this relationship, as shown in Figure 4.17 , a significant positive correlation Pearson $r = 0.68$) is observed. This suggests a linkage between maximum canopy size and final biomass. However, the observed spread in the data indicates that TAGP is also influenced by other factors, such as meteorological conditions, soil properties, and canopy light-use efficiency.

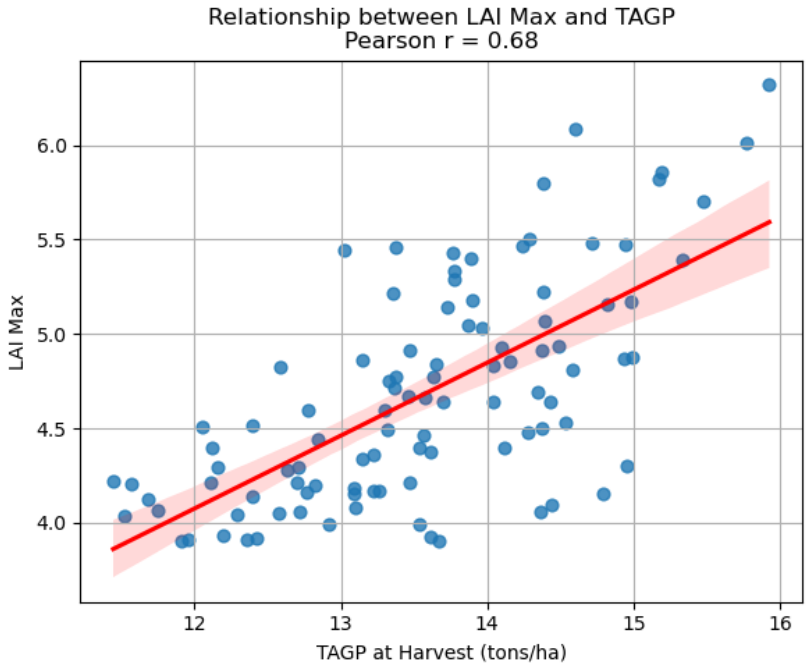

Figure 4.17: Correlation between LAIMAX and TAGP for green maize.

Subsequently, we applied the entire workflow to winter barley, using the same data processing, model setup, and assimilation procedures to evaluate whether the approach is equally effective for a different crop species. This is particularly relevant as, to date, very few studies have applied WOFOST to winter barley, leaving its performance for this crop largely unexplored.

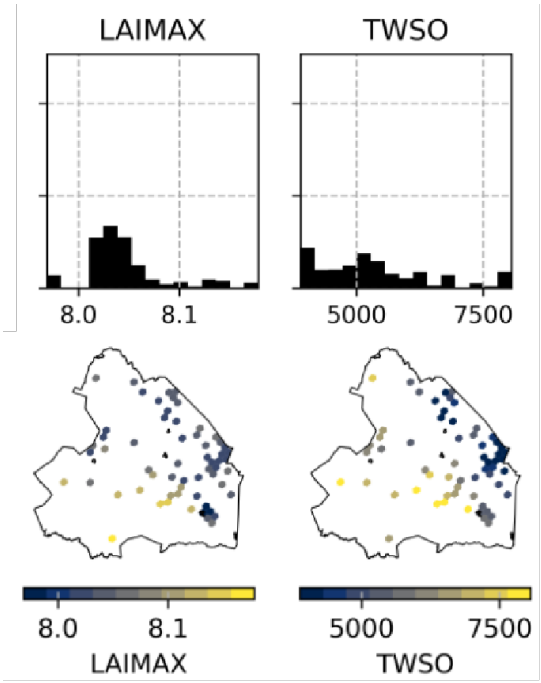

Figure 4.18: Open-loop simulation results of WOFOST for winter barley in 2022.Top panels show the distributions of simulated maximum leaf area index (LAIMAX, left) and total storage organ biomass at DOM (TWSO, right). Bottom panels display the corresponding spatial distributions across all parcels within the study area. LAIMAX is dimensionless, while TWSO is expressed in kg/ha.

Figure 4.18 shows the open-loop simulation results (i.e., without data assimilation). Under the current crop parameter settings, the simulated maximum leaf area index (LAIMAX) is consistently very high across most parcels (8.0 or above), which shows a clear mismatch compared with the Sentinel-2 LAI observations (see Figure 4.19). Meanwhile, the simulated total above-ground storage organ biomass at harvest (TWSO) is considerably underestimated, averaging around $5,000\ kg/ha$. For winter barley, the final grain yield is represented by TWSO, as WOFOST classifies grains as storage organs.

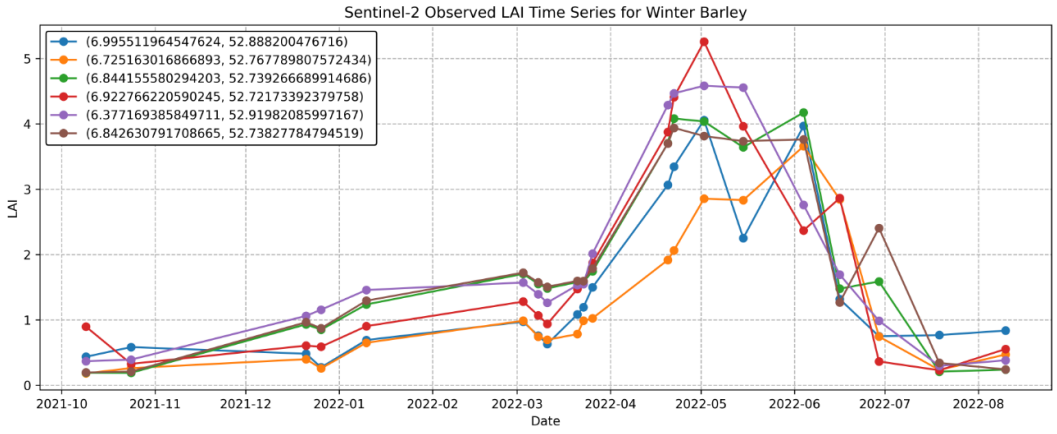

Figure 4.19: Satellite-retrieved LAI time series for six winter barley parcels in the study area, from September 2021 to August 2022.

This discrepancy is most likely caused by inaccurate crop parameterization. A major challenge in simulating winter barley is the lack of a dedicated crop parameterization within the PCSE/WOFOST framework. In the FPCUP project, winter barley was modeled by reusing the spring barley parameter set

with only the sowing date adjusted, which is clearly insufficient and leads to unrealistic crop dynamics. As a result, our initial open-loop simulations failed to reproduce a complete phenological development cycle for winter barley. To address this issue, we contacted experts at Wageningen University Research for support. Fortunately, their team had recently completed a comprehensive calibration of phenological parameters for major European crops, and we were able to incorporate the newly calibrated values for TSUM1, TSUM2, DLO, VERNSAT, DLC, and VERBASE. However, for several other key parameters controlling canopy development and senescence, such as the specific leaf area table (SLATB), leaf lifespan (SPAN), and assimilate partitioning coefficients, we adapted values from winter wheat due to the lack of winter barley–specific data. This mixed parameterization approach is likely the main reason for the discrepancies observed in the open-loop simulations, especially the overestimated LAI. We tested multiple parameter modifications to improve the simulation accuracy, but none of these adjustments yielded satisfactory results. Therefore, we skipped this step and explored whether data assimilation of satellite-derived variables could compensate for structural parameter uncertainties and correct the trajectory of crop state estimates during the growing season.

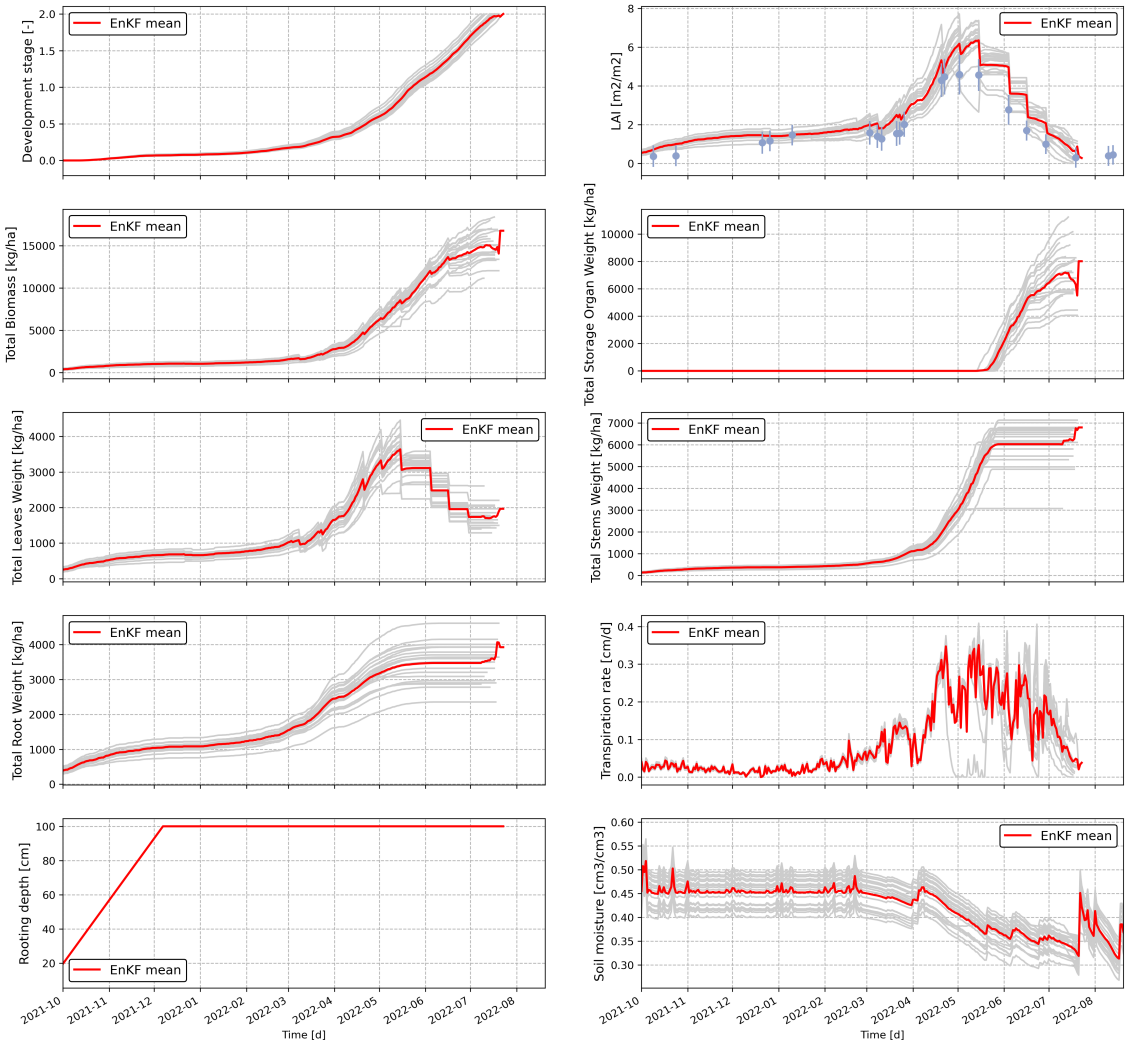

Figure 4.20: EnKF-assimilated WOFOST time series for one winter barley parcel in the study area (52.9198°N, 6.3772°E). The red line is the EnKF ensemble mean; grey shading denotes the ensemble spread. Panels (left to right, top to bottom): development stage (–), LAI ($m^2\ m^{-2}$; blue dots are assimilated Sentinel-2 observations), total above-ground biomass TAGP ($kg\ ha^{-1}$), total storage organ biomass TWSO ($kg\ ha^{-1}$; i.e., grain yield), leaf biomass WL ($kg\ ha^{-1}$), stem biomass WS ($kg\ ha^{-1}$), root biomass WR ($kg\ ha^{-1}$), transpiration rate TRA ($cm\ d^{-1}$), rooting depth RD (cm), and root-zone soil moisture θ ($cm^3\ cm^{-3}$).

Figure 4.20 presents the evolution of key WOFOST state variables for winter barley under the EnKF assimilation framework during the 2022 growing season for one representative location. Compared with the open-loop simulations, the data assimilation significantly improves the model's agreement with remote sensing observations and reduces uncertainty in the estimated crop states. First, for LAI (top-right panel), the open-loop simulations largely overestimated peak canopy development, producing unrealistically high LAIMAX values (> 7.5), which deviated strongly from Sentinel-2 observations. After assimilation, the LAI trajectory aligns much more closely with the satellite-derived values throughout the growing season. Moreover, the stepwise adjustments visible at the observation dates, particularly during the vegetative and peak-growth phases, clearly demonstrate the corrective influence of the assimilated measurements on the model trajectory. This indicates that the EnKF successfully constrains canopy dynamics using Sentinel-2 observations, preventing early-season LAI overshoot. Second, the improved LAI estimates propagate to other biomass components. The total above-ground biomass (TAGP) and storage organ biomass (TWSO, i.e., grain yield) show better consistency with expected winter barley growth patterns after assimilation. In this study, the harvest date of winter barley was set to 10 July 2022. This decision was based on agricultural news reports on the local harvest period and the simulated growth curves of TWSO. Around this date, TWSO in most fields reached its peak and then started to decline, indicating that the crop had entered the maturity stage. Therefore, selecting this date as the harvest time is both reasonable and representative. While the open-loop underestimated final TWSO ($< 5,000\ kg/ha$), the assimilation-corrected simulations increase the mean TWSO toward more realistic levels ($7,000$–$7,500\ kg/ha$), indicating a more accurate representation of assimilate allocation to grains. Finally, the EnKF reduces the ensemble spread (gray shading) for most state variables, especially LAI and TAGP, implying increased confidence in model predictions.

Overall, these results provide strong support for the modeling framework: even under imperfect crop parameterization, assimilating Sentinel-2 LAI via EnKF confers a robust corrective effect, improving canopy and yield simulations while reducing predictive uncertainty relative to the open loop.

4.2. Results of Workflow Testing: Sensitivity Analysis

4.2.1. Sensitivity to Observation Uncertainty

Section 3.2.1 introduces 5 scenarios with different uncertainty strategies. For each scenario, we report the mean EnKF LAI trajectory (red), the full ensemble (gray), and the corresponding observations with $\pm 1\sigma$ (blue) in Fig. 4.21. As scalar metrics we extract LAI at harvest and TAGP at harvest.

Figure 4.21 presents the temporal evolution of LAI under different assimilation scenarios (S1 - S5). For this experimental site, the 10×10 window is entirely located within the field. A clear dependence on the window size is observed. When the window size is small (e.g. S5, window = 1), the analysis is strongly influenced by noisy single-pixel observations. This leads to abrupt adjustments during the growing season and an overall underestimation of LAI in the later stages, reflecting the amplified representativeness error. In contrast, a large window (S3, window = 10) over-smooths the observations, thereby attenuating the peak LAI and reducing the impact of assimilation. Intermediate window sizes (S1: 5, S4: 3) provide a balanced performance: the model trajectories closely follow the observations while maintaining realistic ensemble variability. This indicates that moderate spatial averaging can effectively suppress random noise while preserving local signals. Furthermore, applying inflation (S2,

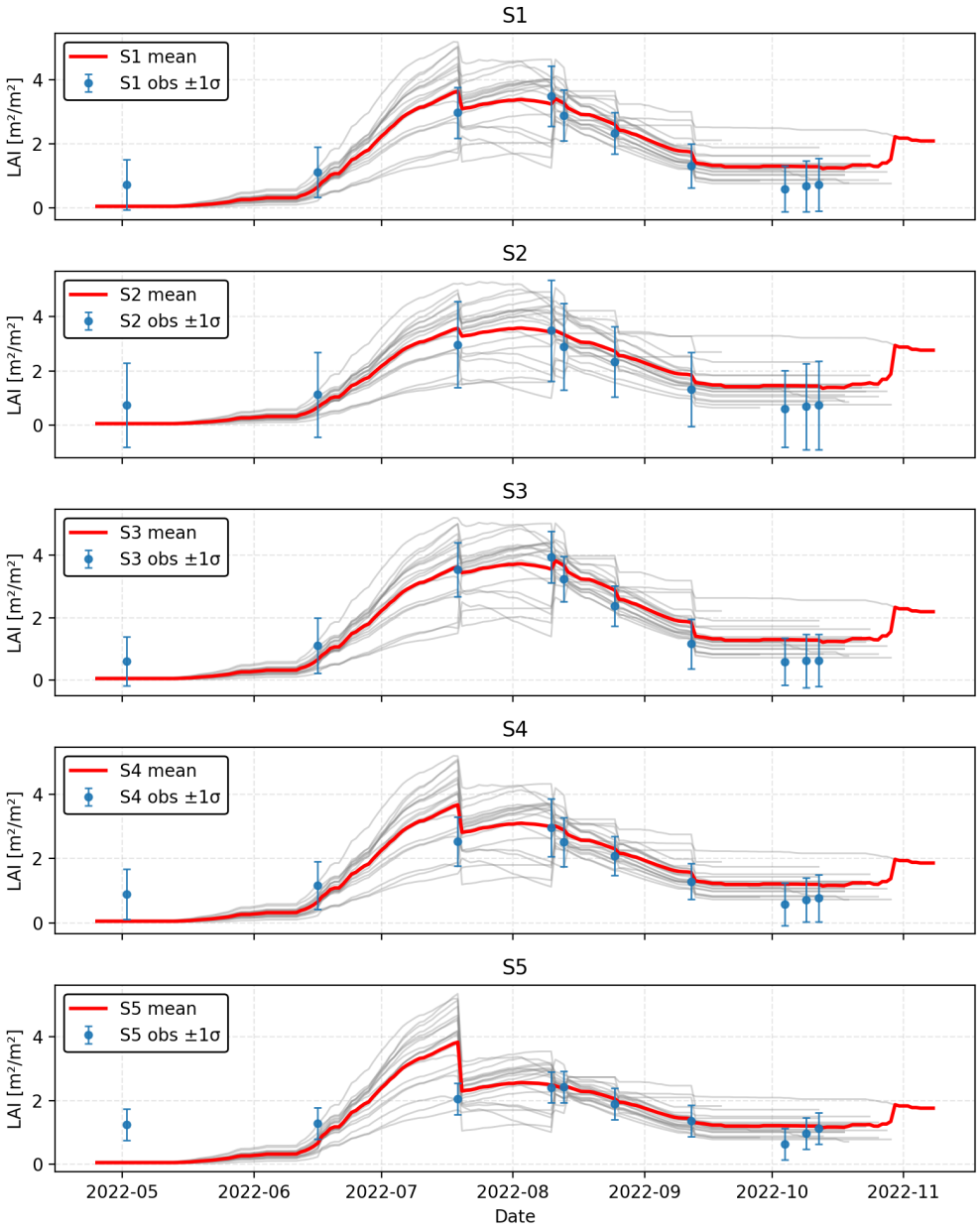

Figure 4.21: LAI trajectory under 5 different observation uncertainty scenarios.

window = 5 with inflation factor = 2) enhances the impact of the observations by increasing ensemble spread, resulting in an improved fit, especially around the LAI peak. However, excessive inflation may risk overfitting to noisy observations.

Table 4.1 further complements the temporal patterns in Figure 4.21, providing a quantitative assessment of how window size and inflation affect the final yield estimates. When the window is too small (e.g., S5, window = 1), TAGP at harvest is markedly underestimated ($11.18\ tons/ha$), consistent with the noisy single-pixel influence and late-season underestimation of LAI observed in Figure 4.21. A large window (S3, window = 10) attenuates the LAI peak and slightly reduces TAGP relative to intermediate windows. By contrast, moderate window sizes (S1: 5; S4: 3) achieve a balanced performance, producing harvest yields in the range of 11.47–$11.98\ tons/ha$, while maintaining realistic ensemble variability. Applying inflation (S2, window = 5 with inflation factor = 2) further enhances the impact of observations, raising TAGP to $12.05\ tons/ha$, indicating that modest inflation can improve yield estimates, particularly around the LAI peak.

Table 4.1: Sensitivity of harvest metrics to LAI observation uncertainty.

Scenario	LAI at harvest	TAGP at harvest (t ha^{-1})
S1: window size = 5	1.31	11.82
S2: window size = 5, inflation = 2	1.45	12.05
S3: window size = 10	1.30	11.98
S4: window size = 3	1.21	11.47
S5: window size =1	1.21	11.18

In summary, small windows amplify noise, large windows dilute the observational signal, while moderate window sizes (3-5) yield the most consistent and physically realistic assimilation outcomes. Inflation can further improve performance, but requires careful tuning to avoid over-adjustment.

4.2.2. Sensitivity to Number of Observations

We conducted the sensitivity experiment at all sites; Fig. 4.22 displays four representative cases. Two consistent patterns emerge. First, LAI and TAGP respond coherently to assimilation: corrections applied to LAI propagate to TAGP, although the response in TAGP is typically attenuated in magnitude. Second, increasing the number of assimilated observations generally reduces the ensemble spread ($\pm 1\sigma$) for both variables, with the largest reduction occurring from the first to about the third–fourth observation. We also observed that, the second observation introduces larger uncertainty. This is possibly because it falls at a phenological breakpoint; the large observed background discrepancy $(y_t - Hx_t^f)$ and the high obeservation quality on that date lead the assimilation to assign greater weight to it, producing a strong correction to LAI that propagates to TAGP; meanwhile, this strong increment pushes the ensemble into a more sensitive (nonlinear) region of state space, so that, when propagated to harvest, the uncertainty (spread) increases for some fields.

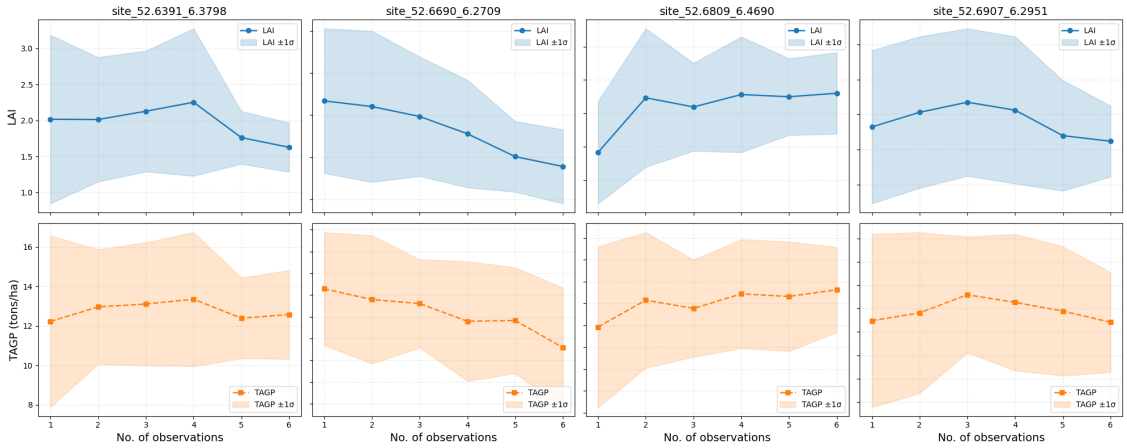

Figure 4.22: Stand derivation of LAI and TAGP at harvest when assimilated with different numbers of observations.

We further examined how the timing of observations shapes the assimilation outcome. Updates applied near phenological breakpoints, most notably Aug 13 produce strong corrections. Short inter-observation gaps (Aug 10 ,Aug 13; ∼3 d) can amplify the effective influence when temporally correlated retrieval errors are treated as independent, thereby over-weighting closely spaced pairs and, for some fields, even increasing the harvest-time spread. Conversely, longer gaps (Aug 13, Aug 25; ∼12 d) allow forecast uncertainty to accumulate, enlarging the background covariance and thus the Kalman gain $K_t = P_t^f H^\top \left(H P_t^f H^\top + R_t\right)^{-1}$, again leading to strong updates. Finally, very late-season observations tend to sample senescent canopies and can bias LAI (and hence TAGP) downward if heavily weighted. These patterns suggest prioritizing 3–4 well-placed dates (early growth, peak LAI, early senescence), down-weighting short-interval pairs (e.g., by thinning or inflating R as a function of Δt), and inflating R or terminating assimilation within ∼40-50 d of harvest.

In conclusion, we assessed how the number, spacing and timing of Sentinel-2 LAI observations shape the EnKF analysis and harvest-time uncertainty for green maize. Across sites, LAI and TAGP respond coherently to assimilation, with TAGP exhibiting a moderate amplitude. Observation dates near phenological breakpoints (e.g., July 24 and Aug 25) produce large observed-background discrepancies and strong analysis increments. Very late-season dates tend to pull the mean downward as they sample senescent canopies. Short-interval pairs (e.g., Aug 10 to 13) carry temporally correlated retrieval errors and can be effectively over-weighted if treated as independent, whereas longer gaps (e.g., Aug 13 to 25) allow forecast variance to grow and thus increase the gain—both mechanisms contributing to stronger updates. Taken together, these results support a compact design with 3 to 4 well-placed dates (rapid growth, peak LAI, early senescence), a preferred spacing of 10 to 21 d, adaptive R based on pixel variance/QA, reduced weight or omission of very late-season dates, and thinning/superobservation or Δt–dependent inflation of R for closely spaced pairs to limit spread growth while retaining high-information observations.

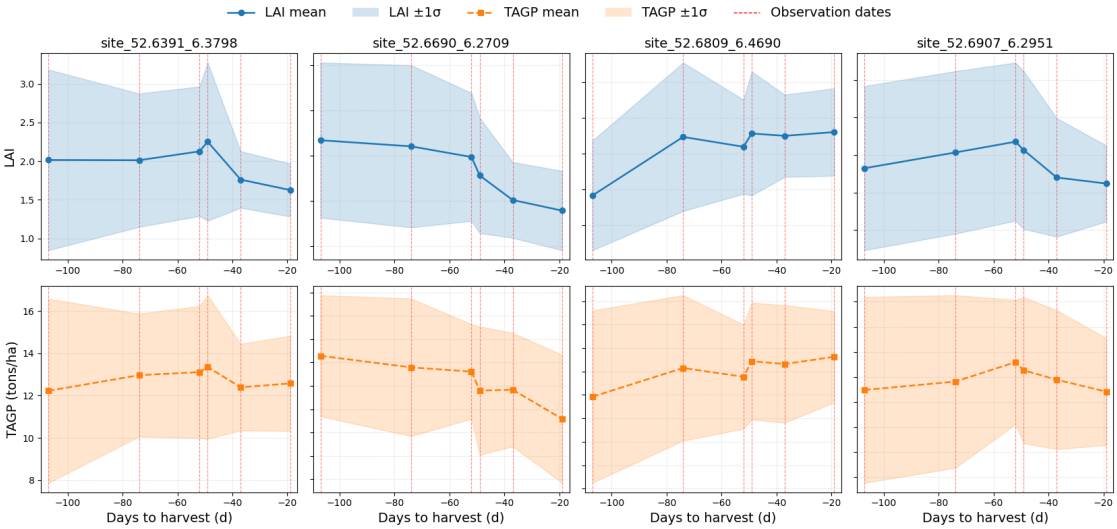

Figure 4.23: Stand derivation of LAI and TAGP at harvest against the observation dates

The sensitivity analysis presented above focused on maize. However, due to cloud contamination, only six valid observations were available during the growing season, which limited the clarity of the results. To address this limitation, the experiment was extended to winter barley. By relaxing the cloud cover filter to 50%, we were able to include a greater number of observations and thereby obtain a more reliable assessment of the sensitivity to observation frequency. As a result, we got 22 observations in total.

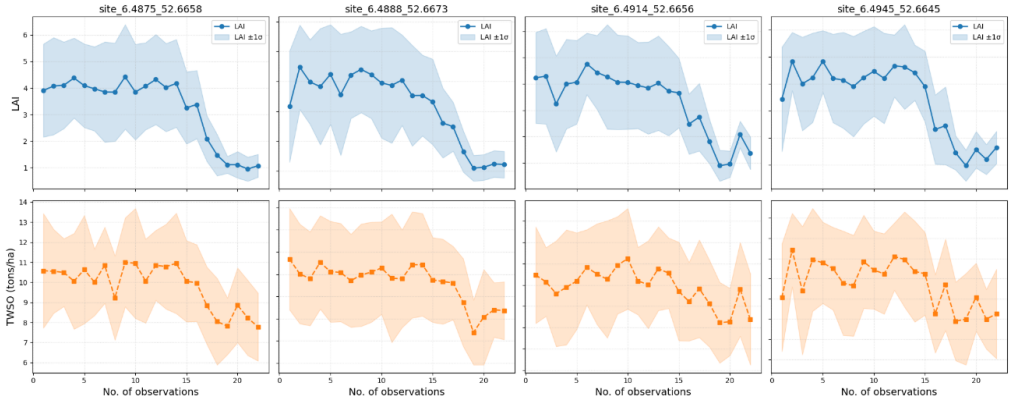

Figure 4.24: Sensitivity of winter barley data assimilation results to the number of assimilated Sentinel-2 observations. Top row: LAI trajectories with ±1σ uncertainty; bottom row: simulated total above-ground dry matter allocated to storage organs (TWSO).

Figure 4.24 presents the sensitivity of winter barley assimilation results to the number of assimilated observations at four locations. Two main patterns can be identified. First, the spread of simulated LAI trajectories decreases markedly as the number of observations increases, particularly beyond 15 observations, indicating that additional data help to better constrain canopy dynamics. Second, in contrast to LAI, the predicted TWSO does not converge but instead exhibits persistent fluctuations across observation scenarios. This can be explained by the fact that yield formation integrates uncertainties over the entire growing season, making it highly sensitive to small deviations in LAI dynamics, especially during the reproductive stages. Consequently, while additional observations reduce canopy uncertainty, they also propagate variability into biomass allocation and final yield estimates.

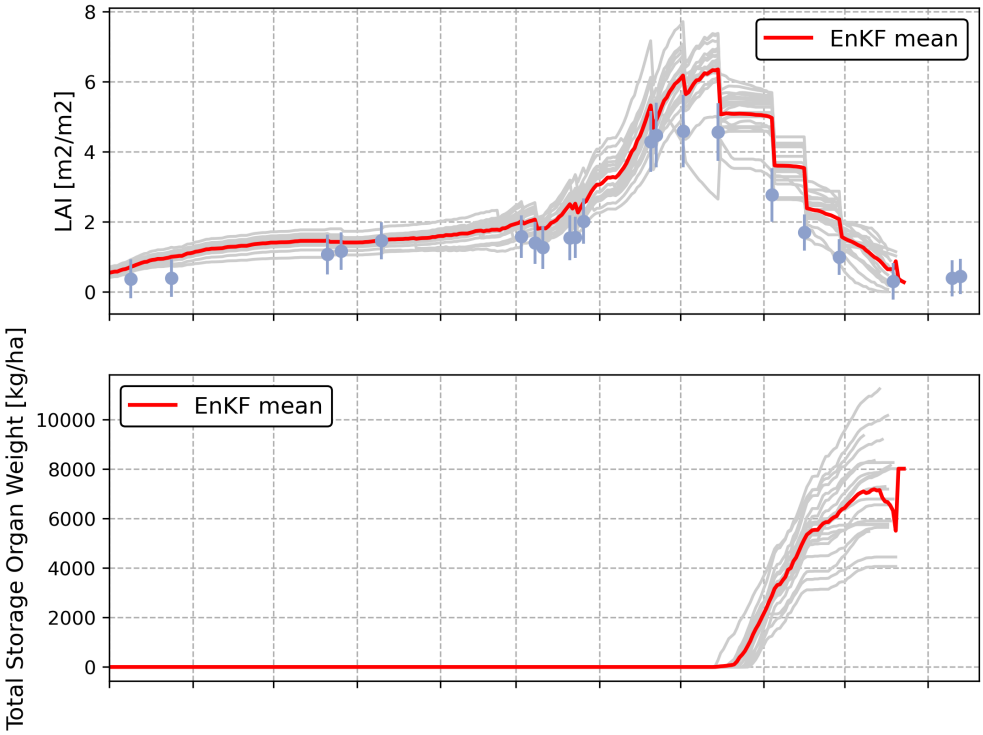

Figure 4.25: Time series of LAI and TWSO for winter barley as simulated by WOFOST with EnKF assimilation.

When examining the time series of TWSO, it becomes evident that the 15th observation coincides with the onset of storage organ formation, at which point TWSO begins to accumulate from zero (see Figure 4.25). This timing is critical, as prior to this stage assimilation adjustments primarily affect vegetative growth, whereas after the reproductive transition even small differences in LAI trajectories are propagated into biomass partitioning and yield formation. Consequently, while the spread in LAI decreases beyond 15 observations, the variability in TWSO estimates increases, reflecting the amplified sensitivity of yield prediction during the grain-filling stage.

The sensitivity experiments demonstrate that the number and timing of assimilated observations exert distinct influences on crop-state estimation. For LAI, increasing the number of observations gradually reduces the spread of simulated trajectories, particularly beyond approximately 15 observations in the case of winter barley. This convergence indicates that additional observations help to constrain canopy dynamics, especially during the peak and senescence stages. However, for TWSO, no comparable convergence is observed. Instead, yield estimates continue to fluctuate as more observations are added. This divergence can be explained by the fact that yield formation integrates assimilation effects over the entire growing season. Once storage organ formation begins, even small deviations in canopy dynamics are amplified and translated into variability in assimilate partitioning and final yield, resulting in persistent fluctuations in TWSO predictions.

Equally important is the timing of observations. During the vegetative phase, when TWSO remains zero, additional observations mainly improve LAI estimates but exert limited influence on yield. In contrast, once the reproductive transition is reached and storage organ accumulation begins, assimilation has a direct impact on yield formation. Observations during this critical window strongly shape the trajectory of TWSO but also increase uncertainty, highlighting the dual role of timing in enhancing

prediction skill and propagating variability.

Overall, these findings suggest that while the number of assimilated observations contributes to reducing canopy uncertainty, the effectiveness of assimilation for yield prediction is governed more by observation timing than by sheer data volume. High-quality observations during canopy expansion, peak growth, and the onset of grain filling are therefore far more valuable than a greater quantity of observations indiscriminately distributed across the season. This underscores the importance of strategically designing assimilation schemes that balance observation number with phenological relevance to achieve robust improvements in both canopy and yield prediction.

4.2.3. Sensitivity to Assimilated Variables

Theoretically, LAI, CCC, and CWC all provide physiological insights into crop development, but they affect the TAGP differently within the WOFOST model framework. LAI directly determines the light interception capacity, serving as the primary driver of gross assimilation. CCC is associated with photosynthetic efficiency, yet it does not directly govern biomass accumulation without changes in canopy structure. CWC peaks generally coincide with LAI, with both showing a marked decline from mid-August to October, reflecting canopy senescence and the progressive loss of water content during maturation and harvest. Therfore, they have different effects on crop yield. Figure 4.26illustrate the distribution of harvest TAGP across all parcels under different assimilation scenarios.

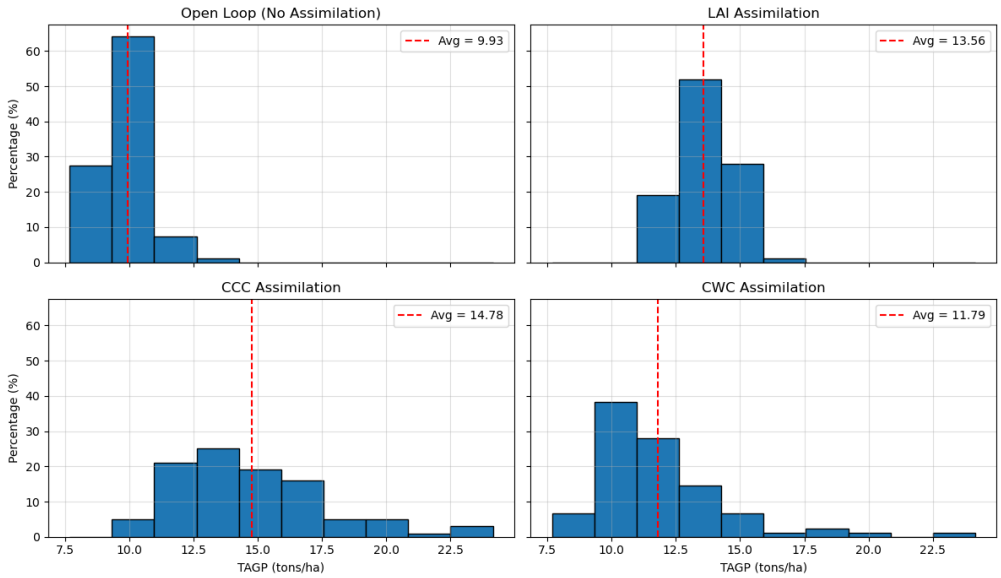

Figure 4.26: Distribution histogram of overall TAGP at harvest under different assimilation scenarios.

Without assimilation (Open Loop), TAGP is substantially underestimated, with a mean of $9.93 tons/ha$, and the distribution is narrow and left-skewed. We also reported a similar pattern in Section 4.1.3, where the open loop underestimated LAI compared to satellite-retrieved observations. This suggests that the model is not optimal. But data assimilation effectively corrected this underestimation no matter which one has been assimilated. In particular, LAI assimilation produced the most “normal” distribution shape, centered within a reasonable range, with the mean increased to $13.56\ tons/ha$, indicating a robust balance between model and observations. While CCC assimilation achieved the highest mean

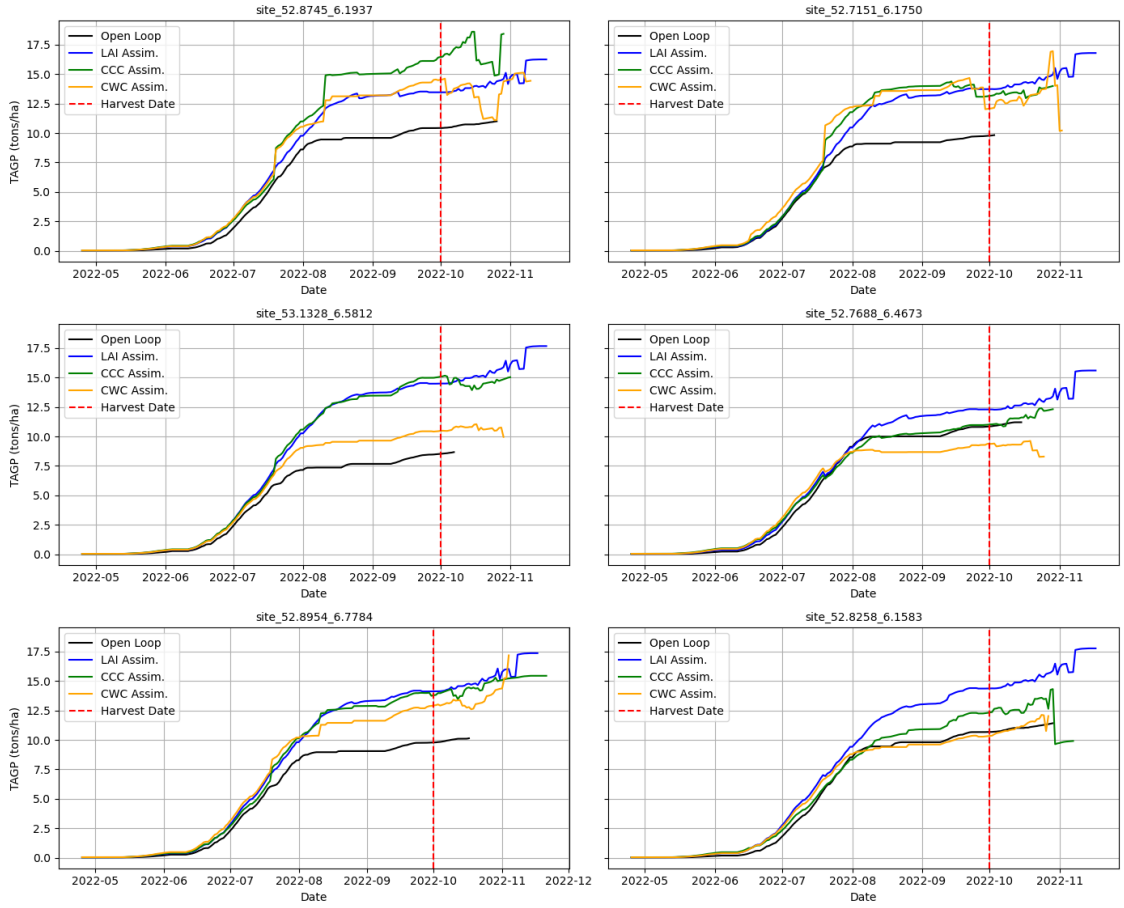

Figure 4.27: TAGP trajectory for six sites under different assimilation scenarios.

yield ($14.78\ tons/ha$), its distribution was more dispersed, suggesting increased uncertainty. CWC assimilation showed only limited improvements, raising the mean to $11.79\ tons/ha$. This discrepancy can be attributed to the varying degrees of coupling between the assimilated variables and crop growth. LAI, as a direct measure of photosynthetically active area, is strongly related to TAGP accumulation; assimilating LAI therefore effectively corrects growth trajectories and results in a realistic yield distribution. In contrast, CCC and CWC primarily capture canopy pigment content and water status, respectively, which are more sensitive to nutrient availability and short-term environmental fluctuations. Their weaker coupling to biomass accumulation explains the more dispersed distributions or limited improvements in TAGP estimates.

Figure 4.27 illustrates the impact of different assimilation schemes on TAGP dynamics. Across all sites, the open-loop simulations consistently underestimated TAGP in the late growing season. In contrast, LAI assimilation effectively corrected this bias, producing smooth TAGP trajectories that aligned well with expected harvest levels, demonstrating the most stable and reliable performance. CCC assimilation, however, occasionally resulted in excessive growth or oscillations at certain sites, likely due to its sensitivity to nitrogen dynamics and leaf senescence. CWC assimilation provided only limited constraints, often underestimating TAGP toward the end of the season. Overall, LAI emerges as the most robust variable for constraining biomass accumulation.

In conclusion, DA not only corrected the systematic underestimation of crop growth but also revealed that LAI assimilation provides the most standard and stable outcomes among the tested observation types.

4.3. Results of Workflow Validation

For validation, we used official agricultural statistics provided by Statistics Netherlands (CBS) through the StatLine open data portal (dataset code: 85636ENG, Arable crops; production, region). This dataset contains long-term records (1994–2024, with preliminary estimates for 2025) of harvested area, crop yields, and total production for major arable crops, including cereals, potatoes, and sugar beet, at both national and provincial levels. The statistics are compiled based on farm surveys and expert assessments, and are annually updated and validated by CBS. Given its broad coverage and high reliability, this dataset provides an authoritative benchmark for evaluating our model-based estimates of crop productivity. The recorded statistics are reported as fresh weight, whereas WOFOST provides crop yields in dry weight. Therefore, we converted the reported data accordingly, as shown in Table 4.2

Table 4.2: Conversion of CBS reported fresh weight to dry weight for green maize and winter barley in Drenthe, 2022.

	Green Maize	Winter Barley
Yield variable	TAGP	TWSO
Fresh weight (ton/ha)	45.7	8.4
Dry matter ratio	0.3	0.84
Dry weight (ton/ha)	13.71	7.06

The yield estimates of green maize derived from the data assimilation framework showed a substantial improvement compared to the open-loop simulation when validated against independent statistical yield data (13.71 t ha^{-1}). As shown in Table 4.3, the open-loop model significantly underestimated crop yield, with a mean bias of -3.78 t ha^{-1} (-27.6%), an RMSE of 3.89 t ha^{-1}, and a Z-score of -4.18, indicating a strong systematic underestimation and a statistically significant deviation from the observed mean. After assimilating satellite-derived canopy variables, the model bias was almost eliminated, decreasing to -0.11 t ha^{-1} (-0.81%), while the RMSE dropped to 0.99 t ha^{-1}, corresponding to a ∼74.5% reduction in overall error. The Z-score was also markedly reduced to -0.11, demonstrating that the assimilated yield estimates were statistically consistent with the independent reference data.

Table 4.3: Validation of simulated green maize yields against independent statistical data (13.71 t ha^{-1}).

	Bias (t ha^{-1})	Relative Bias (%)	Z-score	RMSE (t ha^{-1})
Open-loop	-3.78	-27.6	-4.18	3.89
Assimilated	-0.11	-0.81	-0.11	0.99

These results highlight the effectiveness of the data assimilation approach in correcting systematic errors and improving model accuracy. The reduction in relative bias from -27.6% to -0.8% and the 74.5% decrease in RMSE clearly indicate that the assimilation significantly enhanced the predictive performance of the WOFOST model. The large reduction in $|Z|$-score (from 4.18 to 0.11) further confirms that the assimilated yield estimates fall within one standard deviation of the observed value, underscoring the improved reliability and realism of the yield simulation. Overall, the preceding results demonstrated that TAGP in the open-loop simulation was substantially underestimated, indicating that the model failed to capture the actual growth dynamics. With data assimilation, and particularly LAI

assimilation, the predictions were markedly improved, yielding harvest estimates close to statistical references. This confirms that integrating satellite-derived LAI into WOFOST effectively corrects systematic biases and enhances the reliability of yield predictions.

5

Discussion

5.1. Key Findings

This thesis explored the integration of remotely sensed vegetation parameters into the WOFOST crop growth model through data assimilation, with a particular focus on Sentinel-2 observations and the EnKF. The results showed that the open-loop simulation systematically underestimated crop yield, indicating that the process-based model alone struggled to capture actual crop dynamics under field conditions. Assimilating satellite-derived LAI effectively corrected this bias, resulting in trajectories that were agronomically consistent and harvest estimates that aligned well with statistical references. At the same time, the spatial and temporal patterns revealed by assimilation confirmed that remote sensing can provide meaningful corrections to model states when observations are available at critical growth stages.

A comparison of different biophysical variables further demonstrated that LAI is the most effective variable for assimilation, whereas CCC and CWC, under the current implementation, provided limited additional information since they were indirectly constrained by LAI. The analysis also highlighted the key role of observation quality and frequency, showing that assimilation benefits were most pronounced when LAI observations were concentrated around the canopy expansion and peak phases. Despite improvements, uncertainties remain, stemming from incomplete remote sensing observations, model parameterization, and reliance on prior crop-type information.

Our results demonstrate that assimilating Sentinel-2 LAI observations into the WOFOST model using the Ensemble Kalman Filter (EnKF) substantially improves the simulation of maize canopy development and yield estimation. This finding is consistent with previous studies, for example, Guo et al., 2024, who integrated UAV-derived LAI into WOFOST for summer maize and reported a significant reduction in yield prediction errors, with RMSE decreasing from 413 to 132 kg/ha in 2020 and from 392 to 215 kg·ha□¹ in 2021. Similar to our study, they found that the EnKF effectively corrected LAI trajectories and improved yield forecasts, even when crop parameterization was suboptimal. For winter barley, fewer studies are available that explore LAI assimilation into process-based models. Consequently, our

results provide new insights into the potential of integrating Sentinel-2 LAI within WOFOST for less-studied crops. Overall, these comparisons confirm that EnKF-based assimilation provides a robust corrective mechanism across different environments and crop types, while also highlighting the need for improved crop parameterization and additional observational constraints for optimal performance.

Our assimilation experiments also highlight the intrinsic limitations of the WOFOST model in its open-loop configuration. Without observational constraints, WOFOST tends to underestimate final yield for both maize and winter barley, indicating structural limitations in the current crop parameterization and assimilate allocation schemes. The successful integration of Sentinel-2 LAI through the EnKF demonstrates that data assimilation can effectively compensate for these deficiencies by dynamically correcting canopy trajectories and improving yield forecasts, even under imperfect model parameterization. Moreover, our experiments incorporating additional biophysical variables, CCC and CWC, suggest a promising direction for further model development. While LAI primarily constrains canopy structure, CCC and CWC provide complementary information on photosynthetic capacity and water status, which are not fully represented in WOFOST's current formulation. The observed benefits from multi-variable assimilation indicate that extending WOFOST to better capture these physiological processes, or coupling it with models that explicitly simulate chlorophyll dynamics and canopy water balance, could further enhance predictive skill and model robustness.

5.2. Limitations

Although the results of this study demonstrate that LAI-based data assimilation substantially improves the accuracy of WOFOST simulations of crop growth and yield, several limitations remain. These limitations primarily concern the reliance on prior information, methodological assumptions in assimilation, and constraints of observational and validation data.

Firstly, this study relies on the BRP dataset, which provides detailed parcel boundaries and crop types as critical prior knowledge for assimilation experiments. In the absence of such high-quality datasets, the applicability of the framework becomes more challenging. One alternative is to use remote sensing–based crop classification to pre-identify crop types. Such classification exploits spectral and structural differences across crop growth stages and can partially substitute for prior databases. However, this approach requires reliable training datasets and multi-temporal observations, making it data- and resource-intensive. Another option is to directly fit remotely sensed LAI time series against crop-specific growth trajectories, thereby inferring crop type from the shape of the LAI curve. While this avoids the complexity of full-scale classification, it raises an important question: how many temporal observations are sufficient to reliably distinguish crops, especially during the early growth stages? Sparse or poorly timed observations may lead to ambiguity in crop identification. Thus, whether based on classification or LAI trajectory fitting, crop identification methods require careful trade-offs among accuracy, data availability, and computational cost.

Secondly, in this study, the assimilation of CCC and CWC was implemented by fixing Cw/Cab parameters, meaning that their estimates were largely driven by LAI dynamics. Essentially, CCC and CWC assimilation did not provide fully independent observational constraints but rather acted as derivatives of LAI. This dependence may limit the independent contribution of CCC and CWC in constraining crop growth, thereby reducing the potential benefit of multi-variable assimilation. Future work should investigate approaches that directly assimilate remotely sensed CCC and CWC products instead of inferring

them indirectly from LAI trajectories.

Thirdly, the performance of assimilation is also constrained by the availability and quality of observational and validation data. On the one hand, Sentinel-2 LAI time series are affected by cloud cover and revisit cycles, leading to missing observations during critical growth stages. If more complete and continuous remote sensing observations were available, it would be possible to systematically investigate how observation frequency and quantity influence assimilation performance, thereby informing future data acquisition strategies. Moreover, LAI retrieval itself carries algorithmic uncertainties and saturation effects, which inevitably propagate into the assimilation results. On the other hand, the CBS yield statistics used for validation are only available at provincial averages, lacking the field-level resolution needed to capture local heterogeneity.

5.3. Recommendations to Future Work and Applications

The findings of this study provide several recommendations for future research and practical applications. First, with respect to spatial aggregation, our experiments showed that moderate window sizes (3-5 pixels) offer the best trade-off between suppressing random noise and retaining local signals. For field-scale applications, we therefore recommend this range as a default choice, while future work may explore adaptive approaches that dynamically adjust window size based on within-window variance or by filtering out non-agricultural pixels using parcel boundaries. Second, the timing of observations proved to be more important than their sheer number. Concentrating a limited number of acquisitions (e.g., 4–6) during the critical growth stages, i.e., from stem elongation through tasseling and grain filling, yielded the largest improvements in harvest prediction. This suggests that future designs should prioritize observation timing relative to the harvest date when determining minimal observation schemes. Third, the open-loop simulations revealed that default parameter configurations substantially underestimated biomass, highlighting the need for localized parameterization. We therefore recommend incorporating joint calibration, where remote sensing observations not only constrain state variables such as LAI but also inform crop model parameters (e.g., photosynthetic efficiency, temperature thresholds). Such an approach would yield parameter sets better tailored to local conditions. Fourth, the results underscored the importance of remote sensing data quality: cloud contamination and noisy pixels can destabilize assimilation, particularly with small windows. It is thus advisable to implement rigorous preprocessing, including temporal filtering, gap-filling, and potentially multi-sensor fusion (e.g., Sentinel-2 and Landsat), before assimilation. Ensuring high-quality inputs should be considered a standard step in any operational framework. Finally, when input meteorological data are incomplete, a combination of multi-source gap-filling, bias correction, and uncertainty inflation provides a robust strategy. Short gaps can be bridged with interpolation or nearby stations, medium gaps with bias-corrected reanalysis data, and long gaps with full replacement accompanied by downgraded confidence. Within the assimilation framework, inflating process noise during these periods reduces the risk of biased forcing. Developing automated workflows that adjust gap-filling and uncertainty treatment according to gap length represents a promising direction for future research.

6

Conclusion

This thesis has investigated the integration of satellite-derived biophysical parameters into a process-based crop growth model to enhance field-scale yield prediction under real-world conditions. By assimilating Sentinel-2–retrieved Leaf Area Index (LAI), Canopy Chlorophyll Content (CCC), and Canopy Water Content (CWC) into the WOFOST model using the Ensemble Kalman Filter (EnKF), this work addressed key limitations of conventional crop modeling, including uncertainties in parameterization, incomplete representation of canopy dynamics, and reduced predictive robustness under heterogeneous field conditions.

The results demonstrate that assimilating LAI substantially improves the simulation of canopy development and yield formation, reducing biomass biases and aligning predictions more closely with independent statistical references. Specifically, for green maize, the assimilation framework reduced the mean yield bias from -3.78 t ha^{-1} (-27.6%) in the open-loop simulation to -0.11 t ha^{-1} (-0.81%), and lowered the RMSE from 3.89 t ha^{-1} to 0.99 t ha^{-1}, representing a $\sim$74.5% reduction in overall error. The Z-score improved from -4.18 to -0.11, indicating that the assimilated yield estimates were statistically consistent with the independent reference value. These findings confirm the pivotal role of canopy structural information in constraining process-based models and demonstrate the significant potential of data assimilation to enhance yield prediction reliability. Although CCC and CWC assimilation contributed less under the current implementation due to their dependence on fixed biochemical coefficients, their inclusion provided valuable insights into the challenges of incorporating additional physiological information and revealed the potential of multi-variable assimilation to enrich model constraints. Sensitivity analyses further underscored the importance of observation density, timing, and uncertainty characterization. In particular, observation frequency and timing during the critical canopy expansion and reproductive growth stages (DVS $\approx$ 0.4–1.0) were shown to exert the greatest influence on assimilation performance, emphasizing the need for strategically designed observation campaigns to maximize the impact of satellite-based model updates.

Beyond methodological advancement, this study contributes to the broader field of agro-hydrological modeling by demonstrating the scalability and transferability of a satellite-assisted EnKF framework.

The successful application to winter barley — a crop that has received relatively limited attention in data assimilation research — extends the utility of WOFOST beyond its conventional focus on major cereals and showcases the framework's adaptability to diverse cropping systems. The findings also emphasize the importance of linking remote sensing observations with mechanistic modeling to bridge the gap between empirical yield estimation and physiologically consistent simulation, thus providing a more reliable foundation for precision agriculture, policy support, and food security planning under changing climatic conditions.

Looking forward, several avenues merit further exploration. First, improving the retrieval algorithms and physical parameterization of CCC and CWC could enhance their independent informational value, allowing for more effective multi-variable assimilation. Second, extending the framework to assimilate multi-sensor datasets, including SAR- and thermal-derived variables, could provide complementary information on canopy structure and water status, reducing temporal gaps and observation uncertainty. Finally, coupling assimilation-based crop models with decision-support systems could transform them from diagnostic tools into operational platforms, enabling near-real-time forecasting, adaptive management, and strategic planning across spatial and temporal scales. Collectively, these future efforts will advance the integration of remote sensing and crop modeling, paving the way for more comprehensive, resilient, and scalable agricultural monitoring systems.

7

Implication

7.1. Scientific and Methodological Implications

This study demonstrates the methodological feasibility of dynamically integrating remote sensing observations into a process-based crop growth model using data assimilation techniques. By assimilating biophysical parameters such as LAI, CCC, and CWC into WOFOST through the Ensemble Kalman Filter, the analysis shows that systematic model underestimation in open-loop runs can be corrected, and harvest predictions can be brought closer to reference statistics. This not only validates the practical use of remote sensing–model fusion at the field scale but also highlights the methodological value of state-variable assimilation in crop modeling.

The sensitivity experiments conducted in this study provide further insights into how observation design shapes assimilation performance. Results showed that moderate spatial aggregation (3–5 pixels) achieved the best balance between reducing noise and preserving local signals. Likewise, the timing of observations, particularly during the peak growth stages, was identified as a decisive factor in improving yield prediction. These findings offer a set of empirically grounded guidelines that future researchers can adopt when designing assimilation strategies. They also underscore the potential of extending the framework beyond LAI to include other variables, provided that their retrieval accuracy and temporal coverage are sufficient.

Finally, the study provides a basis for joint calibration approaches, where remote sensing observations are not only used to update dynamic states but also to constrain crop model parameters such as photosynthetic efficiency or phenological thresholds. This points to a promising direction for advancing crop modeling methodology, as parameter optimization through assimilation could significantly reduce local bias and improve the transferability of models across regions and seasons.

7.2. Practical Implications

For agricultural management, the improved accuracy of yield predictions has direct operational value. Farmers and advisors can use mid-season estimates of biomass and harvest potential to adjust irrigation scheduling, fertilizer application, and harvest planning. This is particularly important in precision agriculture contexts, where decisions need to be tailored to individual fields rather than based on regional averages. The study shows that with only a limited number of well-timed satellite acquisitions, substantial improvements in predictive accuracy can be achieved, making this approach practical and scalable in real-world farming systems.

For policymakers, the methodology provides a complementary tool to official statistics, which are typically available only after harvest and at aggregated spatial scales. By delivering near-real-time estimates of crop growth and yield at field to regional scales, the framework supports more agile decision-making for food security assessments, subsidy distribution, and agricultural monitoring programs. Moreover, the integration of free and open satellite data such as Sentinel-2 ensures that the approach remains cost-effective, which is crucial for public-sector adoption.

In addition, the framework has implications for the insurance and finance sectors. Yield-based insurance schemes often suffer from delays and inaccuracies in damage assessment. By assimilating remote sensing data into crop models, insurers can obtain more accurate and timely estimates of expected yield losses, enabling faster and fairer compensation processes. This creates opportunities for integrating Earth observation–based assimilation frameworks into financial risk management tools.

7.3. Societal and Operational Implications

At a broader societal level, the study highlights the potential of assimilation-based crop monitoring systems to strengthen food security monitoring. In regions with limited ground survey capacity, the reliance on freely available satellite data makes the approach attractive for scaling up to national or even global monitoring programs. Such systems can provide governments and international organizations with near-real-time, spatially explicit yield estimates, thereby improving early warning systems for food shortages.

The findings are particularly relevant in the context of climate change, where weather variability and extreme events increasingly threaten crop productivity. By dynamically integrating observations with process-based models, the framework enhances the ability to monitor how crops respond to droughts, heatwaves, or excessive rainfall. This can inform adaptation strategies, such as selecting more resilient varieties or adjusting planting schedules, and ultimately help build climate-resilient agricultural systems.

Finally, the methodological insights from this study can inform the design of future operational platforms. For instance, automated workflows that combine multi-source satellite data, adaptive observation strategies, and uncertainty quantification could be developed into decision-support systems for agriculture. Such platforms would not only benefit farmers and policymakers but also contribute to international efforts aimed at ensuring global food security. By bridging methodological advances with operational needs, the study thus lays the groundwork for both academic innovation and practical deployment.

Appendix A

Table 7.1: Detailed descriptions and values of key crop parameters for green maize in the WOFOST model.

No.	Parameter	Description	Unit	Value
Photosynthesis and Growth				
1	AMAXTB	Maximum assimilation rate vs. development stage	μmol m^{-2} s^{-1}	[0.0,70.0,...]
2	SLATB	Specific leaf area vs. development stage	ha kg^{-1}	[0.0,0.0026,...]
3	SPAN	Leaf life span	days	33.0
4	RGRLAI	Maximum relative growth rate of LAI	day^{-1}	0.0294
5	TMPFTB	Temperature response of photosynthesis	-	[0.0,0.01,...,42.0,0.56]
Phenology				
6	TSUMEM	Temperature sum from sowing to emergence	°C d	110
7	TSUM1	Temperature sum from emergence to anthesis	°C d	695
8	TSUM2	Temperature sum from anthesis to maturity	°C d	800
9	DVSEND	Development stage at maturity	-	2.0
10	TBASE	Base temperature for development	°C	10.0
Partitioning of Assimilates				
11	FLTB	Fraction to leaves vs. development stage	-	[0.0,0.62,...]
12	FSTB	Fraction to stems vs. development stage	-	[0.0,0.38,...]
13	FRTB	Fraction to roots vs. development stage	-	[0.0,0.40,...]
14	FOTB	Fraction to storage organs vs. development stage	-	[0.95,0.0,...]
15	CVL	Conversion efficiency of assimilates to leaves	-	0.68
16	CVS	Conversion efficiency of assimilates to stems	-	0.658
17	CVR	Conversion efficiency of assimilates to roots	-	0.69
18	CVO	Conversion efficiency of assimilates to storage organs	-	0.671
Initial Conditions				
19	TDWI	Initial total dry matter weight	g m^{-2}	50.0
20	RDI	Initial rooting depth	cm	10.0

sentinel-2 image of the whole AOI

Table 7.2: List of Sentinel-2 images used in this study.

Acquisition Date	Satellite	Tile ID	Crop Type
2021-09-04	S2B	T32ULD	Barley
2021-10-04	S2B	T32ULD	Barley
2021-10-09	S2A	T32ULD	Barley
2021-10-24	S2B	T32ULD	Barley
2021-12-21	S2A	T32ULD	Barley
2021-12-26	S2B	T32ULD	Barley
2022-01-10	S2A	T31UGU	Barley
2022-02-26	S2A	T31UFU	Barley
2022-03-03	S2A	T32ULD	Barley
2022-03-08	S2A	T32ULD	Barley
2022-03-11	S2A	T32ULD	Barley
2022-03-21	S2A	T32ULD	Barley
2022-03-23	S2A	T32ULD	Barley
2022-03-26	S2B	T32ULD	Barley
2022-04-20	S2A	T32ULD	Barley
2022-04-22	S2B	T32ULD	Barley
2022-05-02	S2B	T31UGU	Barley, Maize
2022-05-15	S2B	T31UGU	Barley, Maize
2022-06-16	S2A	T32ULD	Maize, Barley
2022-07-19	S2A	T32ULD	Maize, Barley
2022-07-27	S2A	T32ULD	Maize, Barley
2022-08-10	S2B	T32ULD	Maize
2022-08-13	S2B	T32ULD	Maize
2022-08-25	S2A	T32ULD	Maize
2022-09-12	S2B	T32ULD	Maize
2022-10-04	S2B	T31ULD	Maize
2022-10-09	S2B	T32ULD	Maize
2022-10-12	S2B	T32ULD	Maize

Bibliography

Ai, S., Zheng, H., & Yu, J. (2020). Preparation and reflectance spectrum modulation of cr2o3 green pigment by solution combustion synthesis. *Materials*, *13*(7), 1540.

Akumaga, U., Gao, F., Anderson, M., Dulaney, W. P., Houborg, R., Russ, A., & Hively, W. D. (2023). Integration of remote sensing and field observations in evaluating dssat model for estimating maize and soybean growth and yield in maryland, usa. *Agronomy*, *13*(6), 1540.

Alebele, Y., Wang, W., Yu, W., Zhang, X., Yao, X., Tian, Y., Zhu, Y., Cao, W., & Cheng, T. (2021). Estimation of crop yield from combined optical and sar imagery using gaussian kernel regression. *IEEE Journal of Selected Topics in Applied Earth Observations and Remote Sensing*, *14*, 10520–10534.

Anderegg, J., Kirchgessner, N., Aasen, H., Zumsteg, O., Keller, B., Zenkl, R., Walter, A., & Hund, A. (2024). Thermal imaging can reveal variation in stay-green functionality of wheat canopies under temperate conditions. *Frontiers in Plant Science*, *15*, 1335037.

Bai, T., Wang, S., Meng, W., Zhang, N., Wang, T., Chen, Y., & Mercatoris, B. (2019). Assimilation of remotely-sensed lai into wofost model with the subplex algorithm for improving the field-scale jujube yield forecasts. *Remote sensing*, *11*(16), 1945.

Boogaard, H., Wolf, J., Supit, I., Niemeyer, S., & van Ittersum, M. (2013). A regional implementation of wofost for calculating yield gaps of autumn-sown wheat across the european union. *Field Crops Research*, *143*, 130–142.

Boogaard, H., van Diepen, C., Rötter, R., Cabrera, J., & van Laar, H. (1998). *Wofost 7.1: User's guide for the wofost 7.1 crop growth simulation model and wofost control centre 1.5*. DLO Winand Staring Centre. Wageningen, The Netherlands.

Bouras, E. h., Olsson, P.-O., Thapa, S., Díaz, J. M., Albertsson, J., & Eklundh, L. (2023). Wheat yield estimation at high spatial resolution through the assimilation of sentinel-2 data into a crop growth model. *Remote Sensing*, *15*(18), 4425.

Camargo, G., & Kemanian, A. R. (2016). Six crop models differ in their simulation of water uptake. *Agricultural and forest meteorology*, *220*, 116–129.

Castro, R. C. (2024). Prediction of yield and diseases in crops using vegetation indices through satellite image processing. *2024 IEEE Technology and Engineering Management Society (TEMSCON LATAM)*, 1–6.

Chisanga, C. B., Phiri, E., & Chinene, V. R. (2021). Evaluating apsim-and-dssat-ceres-maize models under rainfed conditions using zambian rainfed maize cultivars. *Nitrogen*, *2*(4), 392–414.

Copernicus browser [Accessed: 2025-08-10]. (n.d.).

Croci, M., Impollonia, G., Marcone, A., Antonucci, G., Letterio, T., Colauzzi, M., Vignudelli, M., Ventura, F., Anconelli, S., & Amaducci, S. (2022). Rtm inversion through predictive equations for multi-crop lai retrieval using sentinel-2 images. *Agronomy*, *12*(11), 2835.

De Wit, A., Boogaard, H., Supit, I., & Van Den Berg, M. (2020). *System description of the wofost 7.2, cropping systems model* (tech. rep.). Wageningen Environmental Research.

De Wit, A. d., & Van Diepen, C. (2007). Crop model data assimilation with the ensemble kalman filter for improving regional crop yield forecasts. *Agricultural and forest meteorology*, *146*(1-2), 38–56.

De Wit, A., Boogaard, H., Fumagalli, D., Janssen, S., Knapen, R., van Kraalingen, D., Supit, I., van der Wijngaart, R., & van Diepen, K. (2019). 25 years of the wofost cropping systems model. *Agricultural systems*, *168*, 154–167.

Delloye, C., Weiss, M., & Defourny, P. (2018). Retrieval of the canopy chlorophyll content from sentinel-2 spectral bands to estimate nitrogen uptake in intensive winter wheat cropping systems. *Remote Sensing of Environment*, *216*, 245–261.

Di Paola, A., Valentini, R., & Santini, M. (2016). An overview of available crop growth and yield models for studies and assessments in agriculture. *Journal of the Science of Food and Agriculture*, *96*(3), 709–714.

FAO, IFAD, UNICEF, WFP and WHO. (2024). *The state of food security and nutrition in the world 2024: Financing to end hunger, food insecurity and malnutrition in all its forms* (Accessed: 2025-08-04). Food and Agriculture Organization of the United Nations. Rome. https://doi.org/10.4060/cd1254en

Franch, B., Bautista, A. S., Fita, D., Rubio, C., Tarrazó-Serrano, D., Sánchez, A., Skakun, S., Vermote, E., Becker-Reshef, I., & Uris, A. (2021). Within-field rice yield estimation based on sentinel-2 satellite data. *Remote Sensing*, *13*(20), 4095.

Gebbers, R., & Adamchuk, V. I. (2010). Precision agriculture and food security. *Science*, *327*(5967), 828–831.

Guo, Y., Hao, F., Zhang, X., He, Y., & Fu, Y. H. (2024). Improving maize yield estimation by assimilating uav-based lai into wofost model. *Field Crops Research*, *315*, 109477.

Ji, F., Meng, J., Cheng, Z., Fang, H., & Wang, Y. (2021). Crop yield estimation at field scales by assimilating time series of sentinel-2 data into a modified casa-wofost coupled model. *IEEE Transactions on Geoscience and Remote Sensing*, *60*, 1–14.

Jin, X., Kumar, L., Li, Z., Feng, H., Xu, X., Yang, G., & Wang, J. (2018). A review of data assimilation of remote sensing and crop models. *European journal of agronomy*, *92*, 141–152.

Jones, J. W., Hoogenboom, G., Porter, C. H., Boote, K. J., Batchelor, W. D., Hunt, L. A., Wilkens, P. W., Singh, U., Gijsman, A. J., & Ritchie, J. T. (2003). The dssat cropping system model. *European journal of agronomy*, *18*(3-4), 235–265.

Keating, B. A., Carberry, P. S., Hammer, G. L., Probert, M. E., Robertson, M. J., Holzworth, D., Huth, N. I., Hargreaves, J. N., Meinke, H., Hochman, Z., et al. (2003). An overview of apsim, a model designed for farming systems simulation. *European journal of agronomy*, *18*(3-4), 267–288.

(KNMI), R. N. M. I. (2024a). Harmonie-arome cy43 p1 reforecast [Accessed: 2025-08-06]. https://dataplatform.knmi.nl/dataset/harmonie-arome-cy43-p1-reforecast-1-0

(KNMI), R. N. M. I. (2024b). Open data: Weather model harmonie [Accessed: 2025-08-06]. https://www.knmidata.nl/open-data/harmonie

Konings, A. G., Saatchi, S. S., Frankenberg, C., Keller, M., Leshyk, V., Anderegg, W. R., Humphrey, V., Matheny, A. M., Trugman, A., Sack, L., et al. (2021). Detecting forest response to droughts with global observations of vegetation water content. *Global change biology*, *27*(23), 6005–6024.

Lakhiar, I. A., Yan, H., Zhang, C., Wang, G., He, B., Hao, B., Han, Y., Wang, B., Bao, R., Syed, T. N., et al. (2024). A review of precision irrigation water-saving technology under changing climate for enhancing water use efficiency, crop yield, and environmental footprints. *Agriculture*, *14*(7), 1141.

Li, X., Tan, J., Wang, X., Han, G., Qian, Z., Li, H., Wang, L., & Niu, G. (2024). Responses of spring wheat yield and growth period to different future climate change models in the yellow river irrigation area based on cmip6 and wofost models. *Agricultural and Forest Meteorology*, *353*, 110071.

Liang, S., & Qin, J. (2008). Data assimilation methods for land surface variable estimation. In S. Liang (Ed.), *Advances in land remote sensing* (pp. 297–322). Springer, Dordrecht. https://doi.org/10.1007/978-1-4020-6450-0_12

Marin, F., Jones, J. W., & Boote, K. J. (2017). A stochastic method for crop models: Including uncertainty in a sugarcane model. *Agronomy Journal*, *109*(2), 483–495.

Masson-Delmotte, V., Zhai, P., Pörtner, H.-O., Roberts, D., Skea, J., Shukla, P. R., Pirani, A., Moufouma-Okia, W., Péan, C., Pidcock, R., et al. (2018). Global warming of 1.5 c. *An IPCC Special Report on the impacts of global warming of*, *1*(5), 43–50.

Omia, E., Bae, H., Park, E., Kim, M. S., Baek, I., Kabenge, I., & Cho, B.-K. (2023). Remote sensing in field crop monitoring: A comprehensive review of sensor systems, data analyses and recent advances. *Remote Sensing*, *15*(2), 354.

Panda, S. S., Ames, D. P., & Panigrahi, S. (2010). Application of vegetation indices for agricultural crop yield prediction using neural network techniques. *Remote sensing*, *2*(3), 673–696.

Pathak, T. B., Jones, J. W., Fraisse, C. W., Wright, D., & Hoogenboom, G. (2012). Uncertainty analysis and parameter estimation for the csm-cropgro-cotton model. *Agronomy Journal*, *104*(5), 1363–1373.

Pcse documentation [Accessed: 2025-08-13]. (n.d.).

Sagan, V., Maimaitijiang, M., Bhadra, S., Maimaitiyiming, M., Brown, D. R., Sidike, P., & Fritschi, F. B. (2021). Field-scale crop yield prediction using multi-temporal worldview-3 and planetscope satellite data and deep learning. *ISPRS journal of photogrammetry and remote sensing*, *174*, 265–281.

Shi, Y., Wang, Z., Hou, C., & Zhang, P. (2022). Yield estimation of lycium barbarum l. based on the wofost model. *Ecological Modelling*, *473*, 110146.

Singh, J., Biswas, B., Dhaliwal, L. K., Poddar, R., Gharib, A. F., Raafat, B. M., Gaber, A., & Hossain, A. (2025). Performance evaluation of the dssat-ceres-wheat and wofost-wheat models under various agroclimatic conditions in northwest india. *Theoretical and Applied Climatology*, *156*(5), 1–18.

Supit, I., & van Diepen, C. (1994). *System description of the wofost 6.0 crop simulation model implemented in cgms*. Joint Research Centre (JRC), Commission of the European Communities.

Tagliabue, G., Boschetti, M., Bramati, G., Candiani, G., Colombo, R., Nutini, F., Pompilio, L., Rivera-Caicedo, J. P., Rossi, M., Rossini, M., et al. (2022). Hybrid retrieval of crop traits from multi-temporal prisma hyperspectral imagery. *ISPRS Journal of Photogrammetry and Remote Sensing*, *187*, 362–377.

Tao, W., ZHANG, N.-n., MERCATORIS, B., et al. (2020). Growth simulation and yield prediction for perennial jujube fruit tree by integrating age into the wofost model. *Journal of Integrative Agriculture*, *19*(3), 721–734.

Tilman, D., Balzer, C., Hill, J., & Befort, B. L. (2011). Global food demand and the sustainable intensification of agriculture. *Proceedings of the national academy of sciences*, *108*(50), 20260–20264.

Time and Date. (2022). *Weather history for drenthe, april 2022* [Accessed July 16, 2025]. Retrieved July 16, 2025, from https://www.timeanddate.com/weather/@2756631/historic?month=4&year=2022

UNICEF et al. (2023). The state of food security and nutrition in the world 2023.

Van Diepen, C. v., Wolf, J. v., Van Keulen, H., & Rappoldt, C. (1989). Wofost: A simulation model of crop production. *Soil use and management*, *5*(1), 16–24.

Wageningen Environmental Research. (2024a). *A gentle introduction to wofost 7.2* [Version 20240701]. https://wofost.readthedocs.io/en/7.2/

Wageningen Environmental Research. (2024b). *Pcse / wofost documentation* [Python Crop Simulation Environment (PCSE), Version WOFOST 7.2 / 7.3]. Wageningen University & Research. https://pcse.readthedocs.io/en/stable/

Wang, H., Magagi, R., Goïta, K., Duguay, Y., Trudel, M., & Muhuri, A. (2023). Retrieval performances of different crop growth descriptors from full-and compact-polarimetric sar decompositions. *Remote Sensing of Environment*, *285*, 113381.

Whitcraft, A. K., Vermote, E. F., Becker-Reshef, I., & Justice, C. O. (2015). Cloud cover throughout the agricultural growing season: Impacts on passive optical earth observations. *Remote sensing of Environment*, *156*, 438–447.

Wirsenius, S., Azar, C., & Berndes, G. (2010). How much land is needed for global food production under scenarios of dietary changes and livestock productivity increases in 2030? *Agricultural systems*, *103*(9), 621–638.

World Economic Forum. (2025). *The global risks report 2025, 20th edition* (Accessed: 2025-08-04). World Economic Forum. https://reports.weforum.org/docs/WEF_Global_Risks_Report_2025.pdf

Wu, S., Yang, P., Ren, J., Chen, Z., & Li, H. (2021). Regional winter wheat yield estimation based on the wofost model and a novel vw-4densrf assimilation algorithm. *Remote Sensing of Environment*, *255*, 112276.

Xiao, G., Zhang, X., Niu, Q., Li, X., Li, X., Zhong, L., & Huang, J. (2024). Winter wheat yield estimation at the field scale using sentinel-2 data and deep learning. *Computers and Electronics in Agriculture*, *216*, 108555.

Xu, L., Liu, H., Jiang, L., Zhang, F., Li, X., Feng, X., Huang, J., & Bai, T. (2024). Wofost-n: An improved wofost model with nitrogen module for simulation of korla fragrant pear tree growth and nitrogen dynamics. *Computers and Electronics in Agriculture*, *220*, 108860.

Zhou, Z., Majeed, Y., Naranjo, G. D., & Gambacorta, E. M. (2021). Assessment for crop water stress with infrared thermal imagery in precision agriculture: A review and future prospects for deep learning applications. *Computers and Electronics in Agriculture*, *182*, 106019.